Towards Hybrid Optomechanics in a Fiber-Based Fabry-Perot Cavity

Inauguraldissertation
zur
Erlangung der Würde eines Doktors der Philosophie
vorgelegt der
Philosophisch-Naturwissenschaftlichen Fakultät
der Universität Basel

von

Thibaud Etienne Olivier RUELLE

aus Frankreich

2023

Genehmigt von der Philosophisch-Naturwissenschaftlichen Fakultät

auf Antrag von

Prof. Dr. Martino Poggio
Faculty representative

Prof. Dr. Albert Schliesser
Co-referee

Basel, den 16.11.2021

Prof. Dr. Marcel Mayor
Dean of Faculty

UNIVERSITY OF BASEL

Abstract

Faculty of Science
Department of Physics

Doctor of Philosophy

Towards Hybrid Optomechanics in a Fiber-Based Fabry-Perot Cavity

by Thibaud Etienne Olivier RUELLE

Hybrid optomechanical systems which associate a cavity optomechanical system and a two-level system have recently emerged as a route towards strong optomechanical coupling, which is challenging to achieve in a pure optomechanical system.

Motivated by this context, we decided to develop an experimental platform based on a fiber Fabry-Perot cavity (FFPC) and a mechanical resonator operated in a membrane-in-the-middle (MIM) configuration, aimed at studying the interaction between an optomechanical system and a two-level system embedded within the mechanical resonator. In this thesis I describe the conception, assembly and characterization of this experimental platform.

We used CO_2 laser ablation to fabricate fiber mirrors with a geometry optimized for realizing hybrid optomechanical systems in the MIM configuration. We formed a FFPC between two fiber mirrors, held in a titanium cage that we specially designed for operating a MIM system within a ^{4}He bath cryostat and in high vacuum, while maintaining both a high level of tunability and a high level of mechanical stability. The resulting cavity compares well with other state-of-the-art FFPCs, and most importantly it is mechanically stable enough for us to stabilize its length to within 5 pm using the Pound-Drever-Hall locking technique. The lock remains stable for many hours, both at room temperature and at 4 K, which to the best of our knowledge has not been previously achieved with a high finesse tunable FFPC.

Hexagonal boron nitride (hBN) is a 2D material which has been identified as a promising candidate for realizing hybrid mechanical resonators due to its superior mechanical properties and because it was found to host bright strain-coupled quantum emitters. We fabricated suspended hBN drum micromechanical resonators by transferring exfoliated flakes of hBN on top of a hole in a thin silicon nitride membrane, and inserted one of these hBN drums in the middle of the FFPC, forming a MIM system. We then measured the dispersive and dissipative effect of the position of the hBN drum on the resonance of the cavity, which is a signature of the optomechanical interaction in a MIM system. From this measurement we estimate a linear dispersive optomechanical coupling on the order of $6\,\mathrm{GHz}\cdot\mathrm{nm}^{-1}$.

We expect our forthcoming study of dynamical optomechanical effects in this MIM system to provide valuable data on the mechanical properties of hBN and to help answer some of the open questions about the dynamics of 2D material membranes. We then aim to observe the impact of a quantum emitter positioned within the hBN drum on its optomechanical interaction with the cavity field.

Acknowledgements

During the writing of this thesis, I was lucky to receive help from colleagues, friends, and family, who advised, assisted, supported, and encouraged me on the way. I am grateful for that, as well as to anyone who will read this manuscript.

I will start with the Qubit Optomechanics project team, which I joined at its very beginning, with the initial impulse and funding provided by Floris. David joined shortly after, bringing in his dry humor and his expertise in optics, fab, and whiskey. Thank you David for being a great lab and office companion, and for the "Fuck off" whiskey glass graduation gift. Francesco was a later addition to the team, breathing new life into it with his optimism and uncanny noise hunting abilities. Thank you Francesco for being so generous with your knowledge, time, and friendship.

Our small team is part of the Poggio lab, led by Martino. Thank you Martino for maintaining such an enjoyable working atmosphere, which made my 6 years in the group a great time. Favorite memories include : rooftop ping-pong, Martino's lunchtime stories, office nerf-gun battles, and summer BBQ at the Birsköpfli. Special thanks to Giulio, Hinrich, and Nicola for getting me into cycling, taking way too much pleasure in watching me suffer on Blauen.

On a larger scale, I feel lucky to have been a part of the world-class group of research labs and supporting facilities that forms the Physics Institute of the University of Basel. In particular, the mechanical workshop is the best I have ever had the opportunity to work with, and was instrumental in the success of the Qubit Optomechanics experiment. Thank you Sascha for the many discussions, always resulting in a satisfying middle ground between an over-engineered design and reasonable one. I am also grateful for collaborations and friendships within the Warburton group.

Most importantly, none of this would have been possible without the support of my family. Mom and Dad provide a nurturing and loving home, and have encouraged me to be curious since childhood. My grandparents always believed in me, and inspire me to reach my goals. I enjoy discussing science with my sister Mélanie, and is a great pleasure watching her grow as a young physicist. I cannot thank Zézé et Yves enough for welcoming me every summer, and for being so continuously supportive. Finally, my partner Elodie made every effort so I could focus on my thesis when needed. Our relationship is my proudest achievement, and I will now gladly support her through her own thesis writing. Je t'aime Elodie.

Contents

Introduction

Cavity optomechanical systems [1], in which the inherently weak radiation-pressure force exerted by light on a mechanical element is enhanced by integrating the mechanical element into an optical cavity, make it possible to detect and control the displacement of mechanical resonators with unprecedented precision. Enabled by the advent of increasingly small and high quality mechanical resonators [2], the field of cavity optomechanics has seen tremendous experimental progress, and has additionally emerged as a promising platform for quantum information processing applications [3]. The many milestone proof-of-concept experiments include: ground-state cooling of a nanomechanical oscillator [4, 5], and quantum-limited position sensing [6–8].

As reviewed in [9], optomechanical systems can be implemented using various kinds of optical cavities and mechanical resonators. Here we focus on the membrane-in-the-middle system (MIM) pioneered in the Harris group [10], where the mechanical resonator is placed inside a Fabry-Perot cavity (FPC) formed between two low loss mirrors. The MIM system allows the mechanical resonator and optical cavity to be optimized independently, lifting the requirements on reflectivity and lateral dimensions of the mechanical element that are characteristic of the suspended mirror optomechanical system. This property arguably makes the MIM system the most versatile optomechanical system, in which mechanical resonators with the widest range of mechanical resonance frequency and mass can be used. Notably, most optomechanical effects have been demonstrated in MIM systems using thin silicon nitride (SiN) membranes [11–16], enabled by the high mechanical quality factor of stoichiometric SiN, and recently by the advent of soft-clamped resonators [17, 18]. Other promising materials to use as mechanical resonators in object-in-the-middle systems are photonic crystal reflectors [19], carbon nanotubes [20], silicon carbide nanowires [21], and two-dimensional materials [22].

Cavity optomechanical experiments have up to now relied on strongly driving the optical cavity to enhance the weak dispersive single-photon optomechanical coupling rate so that optomechanical effects overcome dissipation phenomena [23, 24]. In this case, the resulting optomechanical interaction is effectively linear, which prevents the observation of nonlinear single photon effects inherent to optomechanics [25, 26].

On the other hand, hybrid mechanical systems in which a nanomechanical resonator is coupled to a two-level system (TLS) have emerged as an alternative route to ground state cooling and quantum control of a mechanical resonator [3, 27, 28], but are typically limited by the short energy lifetime of the TLS. Since optical control of the TLS is also greatly improved by embedding it in a high finesse cavity, a natural step up is to insert both a mechanical resonator and a TLS in an optical cavity, effectively bridging the gap between cavity optomechanics (cOM) and cavity quantum electrodynamics (CQED) [29–31]. One thus realizes a tripartite hybrid quantum system in which true three-body interaction effects are expected to occur [32–36]; in particular an increase in the effective optomechanical coupling rate by several orders of magnitude was demonstrated in an early circuit cavity electromechanical

experimental implementation [34]. Such a hybrid optomechanical system takes full advantage of the intrinsic capacity of a mechanical oscillator to simultaneously couple to a broad range of physically disparate quantum systems, and thus constitutes a promising platform for both hybrid quantum information processing [37, 38] and quantum sensing [39, 40].

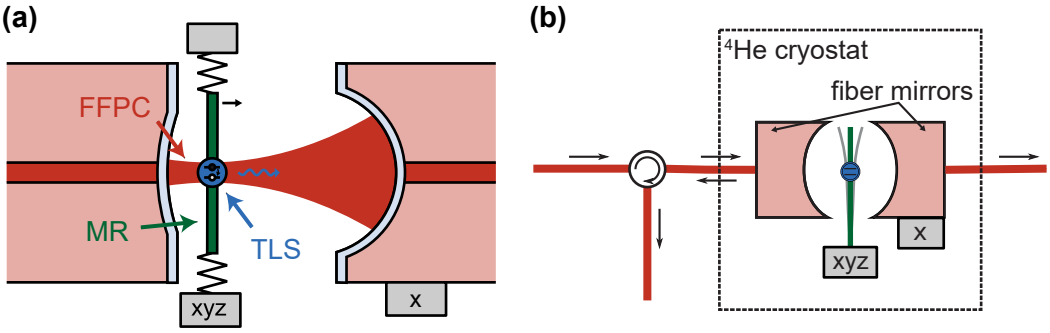

FIGURE 1: **(a):** drawing of the proposed hybrid optomechanics experimental system. FFPC : fiber Fabry-Perot cavity, MR : mechanical resonator, TLS : two-level system. **(b):** drawing of the experimental platform designed to operate the experimental system.

In 2016, motivated by this context, we started developing an experimental platform within which hybrid optomechanical systems can be studied. We decided to build the platform around a widely tunable fiber-based open-access Fabry-Perot optical cavity (FFPC), within which different interchangeable samples can be precisely positioned, forming a membrane/nanowire-in-the-middle optomechanical system (Fig. 1(a)). The experimental system would be operated within a ^{4}He bath cryostat and in high vacuum, by measuring its response in reflection and transmission to a laser input (Fig. 1(b)).

The fiber Fabry-Perot cavity (FFPC) type of optical cavity, formed between the end-facets of two optical fibers [41, 42], was deemed to be the most suitable type of optical cavity for our application for several reasons. First and foremost, the small mode volume typical of FFPCs allows stronger coupling to both nanomechanical resonators and quantum emitters. Secondly, the small lateral dimensions of the fiber mirrors facilitate the realization and alignment of short tunable optical cavities within which mechanical resonators can be positioned, and are also well-suited to the limited space available in our bath cryostat. Finally, FFPCs are addressed directly through the optical fibers, avoiding the complications of using free-space optics to couple light into the cryostat and into the cavity mode [43, 44], albeit at the cost of a capped coupling efficiency determined by the optical fiber and the cavity geometry [41]. These unique features have led to the widespread adoption of FFPCs in cavity quantum electrodynamics [45–55], and in optomechanics [20, 21, 56–60].

Following the discovery of bright strain-coupled quantum emitters in hBN [61], and due to favorable mechanical properties typical of 2D materials [62–64], hexagonal boron nitride has been identified as a promising material for realizing hybrid mechanical resonators [22, 65]. The low optical absorption of hBN makes it a suitable material for optomechanics, as demonstrated in [22]. These elements motivate our choice of hBN to realize the first mechanical resonators to be used in our MIM system. In addition, because several research questions remain open regarding the mechanical behavior of 2D materials in general [66], and hBN in particular, we expect intermediate results obtained during the development of our hybrid optomechanical system to be of scientific interest.

So far, we fabricated fiber mirrors using CO_2 ablation [67, 68]. We used these fiber mirrors to form FFPCs, held in a titanium cage that we specially designed and built for operating a MIM system within a 4He bath cryostat and in high vacuum, while maintaining both a high level of tunability and a high level of mechanical stability [69]. We built a measurement and control setup to operate the experimental system, that we used to characterize extensively the optical properties and the mechanical stability of the FFPC, and to implement a Pound-Drever-Hall locking scheme to stabilize the cavity length. We additionally developed an improved white-light spectroscopy technique to characterize the cavity length. We fabricated suspended hBN drum mechanical resonators, which we inserted within the FFPC to realize a MIM system. We then measured the dispersive and dissipative effect of the position of the hBN drum on the cavity resonance, and used this measurement to estimate the linear dispersive optomechanical coupling. We are now ready to study dynamical optomechanical effects in the MIM system.

Due to its high level of tunability and to its versatility, the experimental platform presented here is suitable for studying a broad array of mechanical elements, and in particular low-dimensional mechanical resonators such as carbon nanotubes or 2D materials. The platform allows such samples to be inserted within the low mode volume and high finesse FFPC, where they can be scanned while controlling and detecting their mechanical vibrations and/or their photoluminescence signal.

Thesis outline

The present thesis reports on the progress of the implementation of our experimental platform for the study of hybrid optomechanical systems, and is structured as follows:

In **Chapter 1** we introduce the theoretical concepts which underlay the behavior of fiber-based MIM optomechanical systems.

In **Chapter 2** we describe the fabrication and measurement setups that were developed as part of the present thesis work : the CO_2 ablation setup used to fabricate fiber mirrors, the measurement and control setup used to operate the MIM system, and the white-light spectroscopy setup used to measure the distance between the fiber mirrors and the sample in the MIM system.

In **Chapter 3** we present the results of our study of single-shot CO_2 ablation of optical fibers, [68], which were then applied to the fabrication of fiber mirrors with optimized geometry for use in our MIM system.

In **Chapter 4** we discuss the design and assembly of the experimental platform, and the procedure through which we characterize the behavior of the fiber-based optical cavity.

In **Chapter 5** we present early experimental results demonstrating the dispersive effect of a hBN drum micromechanical resonator on the resonance frequency of the MIM system, paving the way towards the characterization of the associated optomechanical interaction.

Chapter 1

Theoretical Background

This chapter introduces the theoretical concepts which are required for the understanding, modeling and analysis of the data acquired using our optomechanical experimental system. It is divided into two main sections, which address the two main components of the optomechanical system, namely the Fabry-Perot optical cavity and the mechanical resonator.

1.1 Fabry-Perot Cavities

A Fabry-Perot (FP) cavity is a type of optical cavity which consists of two mirrors facing each other, forming an optical resonator. In this section we summarize the theoretical background necessary to describe and model the behavior of this system. The conventions in [70, 71] are followed whenever possible, and the refractive index of the intracavity medium is assumed to be $n = 1$.

1.1.1 Plane-wave description

The most fundamental properties of the cavities studied here are well captured by a simple 1D model based on plane waves. The mirrors are assumed to be two infinite planes parallel to each other and separated by a distance L_c, as represented in Fig. 1.1. Each of the two mirrors ($i = 1, 2$) is characterized by its residual transmission t_i and losses l_i, and we define the corresponding power transmittance $T_i = t_i^2$, power losses $L_i = l_i^2$, and power reflectance $R_i = 1 - T_i - L_i$.

As a starting point we take the standard vectorial plane-wave expression for the electric field, using a sign convention matching the theory of quantum mechanics:

$$\mathcal{E}(\mathbf{r}, t) = \mathcal{E}_0 \, \mathbf{e}_p \cos(\mathbf{k} \cdot \mathbf{r} - \omega t + \phi) \tag{1.1}$$

where $\mathbf{e}_p$ is the direction of polarization, $\mathbf{k} = k \, \mathbf{e}_k = \omega / c \, \mathbf{e}_k$ is the wave vector pointing in the direction of propagation $\mathbf{e}_k$, $\mathcal{E}_0$ is the field amplitude, $\omega = 2\pi \nu = 2\pi \, c / \lambda$ is the angular frequency, and ϕ is a phase offset.

Assuming the light field is propagating along the z axis ($\mathbf{k} \cdot \mathbf{r} = kz$) and ignoring polarization for the moment, we consider the scalar plane-wave expression:

$$\mathcal{E}(z, t) = \mathcal{E}_0 \cos(kz - \omega t + \phi) \tag{1.2}$$

Finally, using the complex notation by defining E such that $\mathcal{E} = \mathrm{Re}\{E\}$ and $E_0 = \mathcal{E}_0 \, e^{i\phi}$, we obtain:

$$E(z, t) = E_0 \, e^{i(kz - \omega t)} \tag{1.3}$$

This expression for the light field is used to derive the theory presented in the rest of this section. The power in the light field can be expressed as $P = |E|^2 = E \, E^\star$.

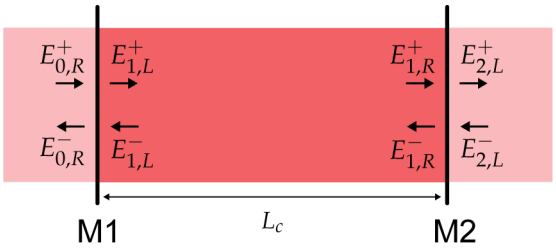

FIGURE 1.1: Sketch of a planar-planar Fabry-Perot cavity. The fields propagating forward (+) and backward (-) and taken near the left (L) and/or right (R) boundaries of each part of the system are defined.

The fields of interest in Fig. 1.1 can be related to each other using the coupling matrix formalism:

$$\begin{pmatrix} E^+_{2,L} \\ E^-_{2,L} \end{pmatrix} = \mathbf{C}_{\text{cav}} \begin{pmatrix} E^+_{0,R} \\ E^-_{0,R} \end{pmatrix} \tag{1.4}$$

$$\begin{pmatrix} E^+_{1,L} \\ E^-_{1,L} \end{pmatrix} = \mathbf{C}_{\text{mirror},1} \begin{pmatrix} E^+_{0,R} \\ E^-_{0,R} \end{pmatrix} \tag{1.5}$$

where $\mathbf{C}_{\text{cav}}$ is the coupling matrix for the entire cavity, and $\mathbf{C}_{\text{mirror},1}$ is the coupling matrix for mirror 1. The cavity coupling matrix is expressed as the product of the coupling matrices of the individual elements of the cavity:

$$\mathbf{C}_{\text{cav}} = \mathbf{C}_{\text{mirror},2}\, \mathbf{C}_{\text{space}}(L_c, 1)\, \mathbf{C}_{\text{mirror},1} \tag{1.6}$$

with the mirror and free-space coupling matrices defined as:

$$\mathbf{C}_{\text{mirror},i} = \frac{i}{t_i} \begin{pmatrix} -1 & r_i \\ -r_i & r_i^2 + t_i^2 \end{pmatrix} \tag{1.7}$$

$$\mathbf{C}_{\text{space}}(L, n) = \begin{pmatrix} e^{-i\,kn\,L} & 0 \\ 0 & e^{i\,kn\,L} \end{pmatrix} \tag{1.8}$$

with $r_i = \sqrt{R_i}$.

Equations (1.4) and (1.5) can be solved to obtain expressions for the fields transmitted through the cavity $E_t = E^+_{2,L}$, reflected by the cavity $E_r = E^-_{0,R}$, and circulating inside the cavity $E_{\text{circ}} = E^+_{1,L}$, with the input fields taken as $E^+_{0,R} = E_i$ and $E^-_{2,L} = 0$, and defining $\phi \equiv k\,L_c = (2\pi/\lambda)\,L_c = (\omega/c)\,L_c$. The circulating, reflection and transmission coefficients are then expressed as:

$$C_{\text{circ}} = \frac{E_{\text{circ}}}{E_i} = \frac{i t_1}{1 - r_1 r_2\, e^{i\,2\phi}} \tag{1.9}$$

$$C_r = \frac{E_r}{E_i} = \frac{r_1 - r_2\left(r_1^2 + t_1^2\right) e^{i\,2\phi}}{1 - r_1 r_2\, e^{i\,2\phi}} \tag{1.10}$$

$$C_t = \frac{E_t}{E_i} = \frac{-t_1 t_2\, e^{i\,\phi}}{1 - r_1 r_2\, e^{i\,2\phi}} \tag{1.11}$$

The corresponding intensity coefficients are:

$$C_{\text{Circ}} = \frac{P_{\text{circ}}}{P_i} = \frac{t_1^2}{(1-r_1r_2)^2 + 4\,r_1r_2\sin^2(\phi)} \tag{1.12}$$

$$C_R = \frac{P_r}{P_i} = \frac{\left(r_1 - r_2\left(r_1^2+t_1^2\right)\right)^2 + 4\,r_1r_2\left(r_1^2+t_1^2\right)^2\sin^2(\phi)}{(1-r_1r_2)^2 + 4\,r_1r_2\sin^2(\phi)} \tag{1.13}$$

$$C_T = \frac{P_t}{P_i} = \frac{t_1^2\,t_2^2}{(1-r_1r_2)^2 + 4\,r_1r_2\sin^2(\phi)} \tag{1.14}$$

From these formula we can define some important concepts and quantities. Cavity resonance is defined as the point where the field circulating inside the cavity is maximum. It is achieved when $\phi = \phi_q = q\pi$ with $q \in \mathbb{N}$, which can be realized by tuning either the length of the cavity to $L_{c,q} = q\frac{\lambda}{2}$, or the angular frequency of the input field to $\omega_{c,q} = q\frac{\pi c}{L_c}$. The free spectral range is defined as the difference between two consecutive resonances : in terms of angular frequency $\Delta\omega_{\text{FSR}} = \frac{\pi c}{L_c}$, and in terms of cavity length $\Delta L_{c,\text{FSR}} = \lambda/2$. The full-width-at-half-maximum (FWHM) is defined in terms of angular frequency as $\kappa = 2\omega_p$, with ω_p the angular frequency at which the circulating power decreases to half of its maximum:

$$\kappa = \frac{2c}{L_c}\arcsin\left(\frac{1-r_1r_2}{2\sqrt{r_1r_2}}\right) \tag{1.15}$$

Finally, the finesse, which represents the enhancement of the circulating power over the power that is coupled into the cavity, is defined as:

$$\mathcal{F} = \frac{\Delta\omega_{\text{FSR}}}{\kappa} \tag{1.16}$$

Equations (1.12) to (1.14) are plotted in red in Fig. 1.2 for varying ω, with annotations to illustrate the definitions of $\Delta\omega_{\text{FSR}}$ and κ.

Let us now consider the case of a cavity which is defined between high reflectivity mirrors such that $t_1, t_2, l_1, l_2 \ll 1$. Under this approximation, we have:

$$\arcsin\left(\frac{1-r_1r_2}{2\sqrt{r_1r_2}}\right) \sim \frac{1}{2}\frac{1-r_1r_2}{\sqrt{r_1r_2}} \sim \frac{1-r_1r_2}{2} \sim \frac{T_1+L_1+T_2+L_2}{4}$$

which can be inserted in Eqs. (1.15) and (1.16) to yield:

$$\kappa \sim \frac{c}{L_c}(1-r_1r_2) \sim \frac{c}{2L_c}(T_1+L_1+T_2+L_2) \tag{1.17}$$

$$\mathcal{F} \sim \frac{\pi}{1-r_1r_2} \sim \frac{2\pi}{T_1+L_1+T_2+L_2} \tag{1.18}$$

Making the additional assumption that the cavity is close to resonance, and defining $\Delta = \omega - \omega_{c,q}$ with $\Delta \ll \Delta\omega_{\text{FSR}}$, we can write :

$$1 - r_1r_2\,e^{i\,2\phi} \sim 1 - r_1r_2 - 2ir_1r_2\phi = 2\frac{L_c}{c}\left(\frac{\kappa}{2} - i\Delta\right)$$

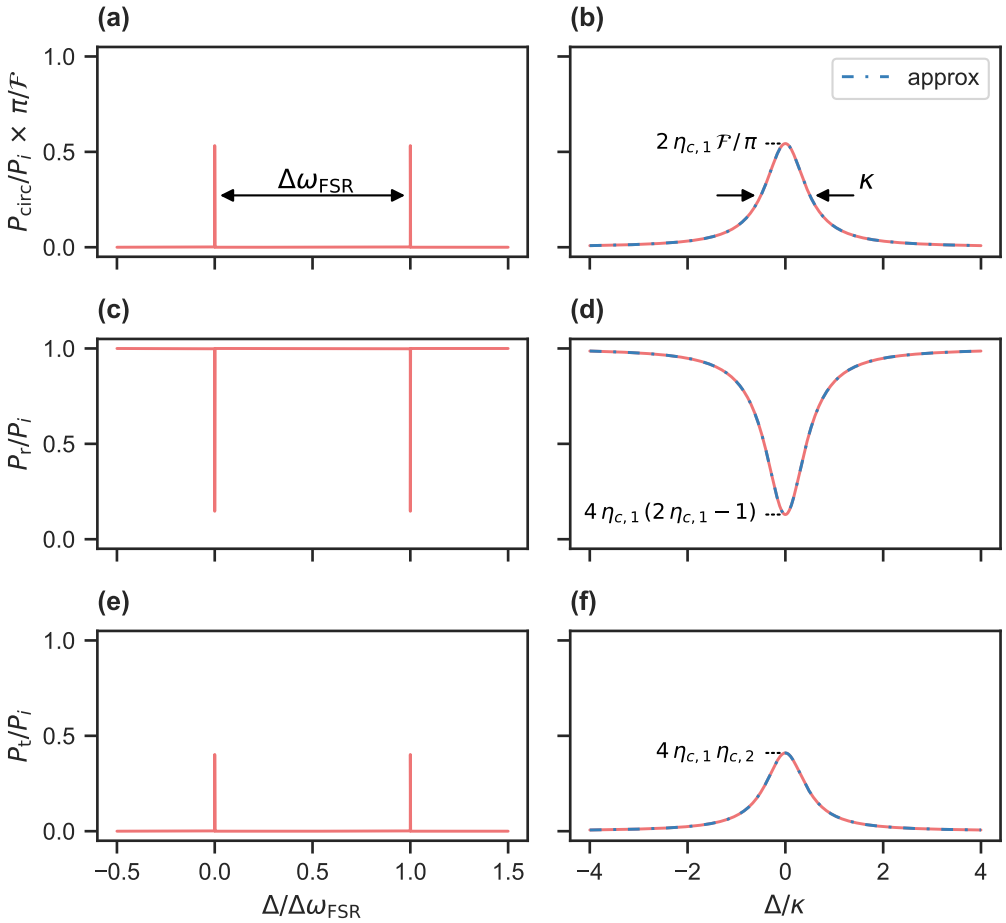

FIGURE 1.2: Plots of the circulating **(a,b)**, reflected **(c,d)** and transmitted **(e,f)** power as a function of detuning in a planar Fabry-Pérot cavity according to Eqs. (1.12) to (1.14). The right column is a zoom around a single cavity resonance, with the simplified expressions of Eqs. (1.22) to (1.24) overlayed as dashed blue curves.

Equations (1.9) to (1.11) can then be simplified to:

$$C_{\text{circ}} \sim \frac{c}{2L_c}\frac{it_1}{\kappa/2 - i\Delta} \tag{1.19}$$

$$C_r \sim 1 - \frac{c}{2L_c}\frac{t_1^2}{\kappa/2 - i\Delta} \tag{1.20}$$

$$C_t \sim \frac{c}{2L_c}\frac{-t_1 t_2}{\kappa/2 - i\Delta} \tag{1.21}$$

and Eqs. (1.12) to (1.14) to:

$$C_{\text{Circ}} \sim \frac{\mathcal{F}}{\pi}\frac{\kappa_{\text{ex},1}}{\kappa/2}\frac{(\kappa/2)^2}{(\kappa/2)^2 + \Delta^2} \tag{1.22}$$

$$C_R \sim 1 - \frac{\kappa_{\text{ex},1}}{\kappa/2}\left(2 - \frac{\kappa_{\text{ex},1}}{\kappa/2}\right)\frac{(\kappa/2)^2}{(\kappa/2)^2 + \Delta^2} \tag{1.23}$$

$$C_T \sim \frac{\kappa_{\text{ex},1}}{\kappa/2}\frac{\kappa_{\text{ex},2}}{\kappa/2}\frac{(\kappa/2)^2}{(\kappa/2)^2 + \Delta^2}, \tag{1.24}$$

where we defined the loss rates through each mirror as $\kappa_{\mathrm{ex},i} = t_i^2 c/(2L_c)$. Equations (1.22) to (1.24) are plotted as blue dashed curves in Fig. 1.2(b,d,f), displaying the characteristic Lorentzian lineshape of the resonance of a high-finesse FP cavity.

An important characteristic of a FP cavity is the degree of overcoupling defined as $\eta_{c,i} = \kappa_{\mathrm{ex},i}/\kappa$. A FP cavity is said to be impedance-matched when $\eta_{c,1} = \eta_{c,2} = 0.5$, with deviations from this value leading to the power reflectance and transmittance of the cavity at resonance respectively deviating from 0 and 1, as illustrated in Fig. 1.2.

We additionally define the cavity susceptibility as:

$$\chi_c(\Delta) = \frac{1}{\kappa/2 - i\Delta} \tag{1.25}$$

1.1.2 Phase-modulated input and Pound-Drever-Hall error signal

Up to now we have assumed the input field to be monochromatic at angular frequency ω. Here we consider the case when the input field is instead phase-modulated, creating additional frequency components called sidebands. In this work we use phase-modulated input fields to lock the length of a Fabry-Perot cavity to the laser frequency via the Pound-Drever-Hall (PDH) stabilization scheme [72, 73] (Section 4.3.4). We also plan to use phase-modulated input fields as a diagnostic tool for characterizing optomechanical systems by implementing an optomechanically-induced transparency (OMIT) measurement, described theoretically in Section 1.2.3.

The generation of frequency sidebands by modulating the phase of the electric field is described by the following equations:

$$E_i(t) = E_0 e^{-i(\omega t + \beta \sin(\Omega t))} \tag{1.26}$$

$$= E_0 e^{-i\omega t}\left(J_0(\beta) + \sum_{k=1}^{\infty}(-1)^k J_k(\beta) e^{ik\Omega t} + \sum_{k=1}^{\infty} J_k(\beta) e^{-ik\Omega t}\right) \tag{1.27}$$

$$\underset{\beta\to 0}{\approx} E_i e^{-i\omega t}\left(J_0(\beta) + J_1(\beta)\left(e^{-i\Omega t} - e^{i\Omega t}\right)\right) \tag{1.28}$$

where $J_k(x)$ are the Bessel functions.

The field reflected from the cavity is the sum of each frequency component:

$$E_r(t) = E_0 e^{-i\omega t}\left(J_0(\beta)F(\Delta) + J_1(\beta)F(\Delta+\Omega)e^{-i\Omega t} - J_1(\beta)F(\Delta-\Omega)e^{i\Omega t}\right) \tag{1.29}$$

where we write the cavity reflection coefficient as $F(\Delta) = C_r = 1 - \kappa_{\mathrm{ex},1}\,\chi_c(\Delta)$, following [73]. The field power can be expressed as:

$$\begin{aligned}\frac{P_r(t)}{P_0} &= J_0(\beta)^2|F(\Delta)|^2 + J_1(\beta)^2|F(\Delta-\Omega)|^2 + J_1(\beta)^2|F(\Delta+\Omega)|^2 \\ &\quad + 2J_0(\beta)J_1(\beta)\,\mathrm{Re}\left\{(F^\star(\Delta)F(\Delta+\Omega) - F(\Delta)F^\star(\Delta-\Omega))e^{-i\Omega t}\right\} \\ &\quad - 2J_1(\beta)^2\,\mathrm{Re}\left\{F(\Delta+\Omega)F^\star(\Delta-\Omega)e^{-2i\Omega t}\right\}\end{aligned} \tag{1.30}$$

highlighting the beatnotes at Ω and 2Ω. The corresponding photodetector voltage is given by $V_{\mathrm{PD}} = \eta_{\mathrm{PD}} P_r(t)$, with η_{PD} the detection efficiency. The photodetector

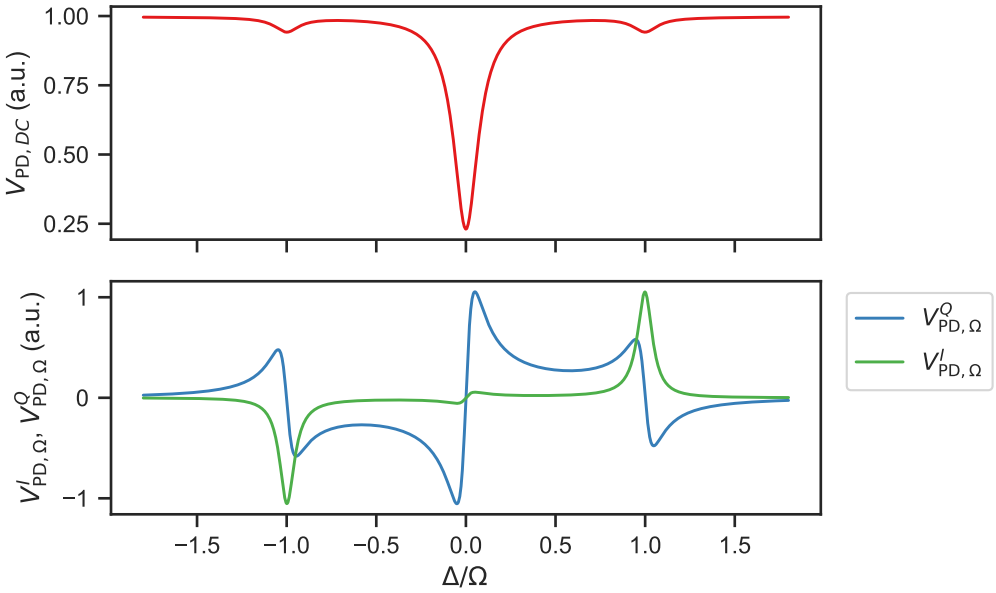

FIGURE 1.3: **(top)**: DC component of the reflected power from a FP cavity when the input field is phase-modulated. **(bottom)**: quadratures of the beatnote at Ω in the photodetected reflection signal.

voltage is demodulated at Ω to obtain $V_{\mathrm{PD},\Omega}(t) \equiv V^I_{\mathrm{PD},\Omega}\cos\Omega t + V^Q_{\mathrm{PD},\Omega}\sin\Omega t$:

$$\begin{aligned}\frac{V_{\mathrm{PD},\Omega}(t)}{2P_0J_0(\beta)J_1(\beta)\eta_{\mathrm{PD}}} &= \mathrm{Re}\{(F^\star(\Delta)F(\Delta+\Omega) - F(\Delta)F^\star(\Delta-\Omega))\}\cos\Omega t \\ &\quad + \mathrm{Im}\{(F^\star(\Delta)F(\Delta+\Omega) - F(\Delta)F^\star(\Delta-\Omega))\}\sin\Omega t\end{aligned} \tag{1.31}$$

When the modulation and demodulation are performed using a lock-in amplifier, the complex response measured is:

$$V^I_{\mathrm{PD},\Omega} + i\,V^Q_{\mathrm{PD},\Omega} = 2P_0J_0(\beta)J_1(\beta)\eta_{\mathrm{PD}}(F^\star(\Delta)F(\Delta+\Omega) - F(\Delta)F^\star(\Delta-\Omega)) \tag{1.32}$$

The two quadratures of $V_{\mathrm{PD},\Omega}(t)$ are plotted in Fig. 1.3 in the fast-modulation case ($\Omega > \kappa$). In this case $V^Q_{\mathrm{PD},\Omega}$ is linearly proportional to the detuning around $\Delta = 0$ and $\Delta = \pm\Omega$. The PDH stabilization scheme consists in using $V^Q_{\mathrm{PD},\Omega}$ as the error signal in a feedback loop acting on either the laser frequency or the cavity length to stabilize the detuning at $\Delta = 0$, or at $\Delta = \pm\Omega$ [74].

1.1.3 Transverse modes

General properties of Hermite-Gauss transverse modes

Some more advanced properties of Fabry-Perot cavities cannot be accurately described by the simple plane-wave model of Section 1.1.1, and require taking the transverse components of the light field into account. Here we consider the following expression for an optical beam propagating in the z direction, with transverse component $u(x,y,z)$:

$$E(x,y,z,t) = u(x,y,z)\,e^{i(kz-\omega t)} \tag{1.33}$$

The power in such a beam is given by :

$$P(z) = \iint E(x,y,z)E^{\star}(x,y,z)\,\mathrm{d}x\,\mathrm{d}y \tag{1.34}$$

We place ourselves in the paraxial approximation, under which the envelope of the light field $u(x,y,z)$ is assumed to vary slowly with z compared to $e^{i(kz)}$ and to the transverse variations, such that:

$$\left|\partial_z^2 u(x,y,z)\right| \ll |2k\partial_z u(x,y,z)|, \left|\partial_x^2 u(x,y,z)\right|, \left|\partial_y^2 u(x,y,z)\right| \tag{1.35}$$

Inserting Eq. (1.35) into the standard Helmoltz equation leads to the paraxial wave equation, which governs the propagation of the paraxial beams considered in this section:

$$\left(\partial_x^2 + \partial_y^2\right)u(x,y,z) + 2ik\partial_z u(x,y,z) = 0 \tag{1.36}$$

Hermite-Gauss modes $u_{n,m}(x,y,z)$ are solutions of Eq. (1.36) which are well suited to the optical cavities considered here. They can be separated into independent tangential and sagittal components $u_n^t(x,z)$ and $u_m^s(y,z)$ such that:

$$u_{n,m}(x,y,z) = u_n^t(x,z)u_m^s(y,z) \tag{1.37}$$

$$u_n^t(x,z) = \left(\frac{2}{\pi}\right)^{\frac{1}{4}}\left(\frac{1}{2^n\,n!\,w_t(z)}\right)^{\frac{1}{2}} H_n\left(\frac{\sqrt{2}x}{w_t(z)}\right) e^{i\frac{kx^2}{2R_t(z)} - \frac{x^2}{w_t^2(z)} - i\left(\frac{1}{2}+n\right)\Psi_t(z)} \tag{1.38}$$

The corresponding expression for $u_m^s(y,z)$ is obtained by replacing $\{n,t,x\}$ by $\{m,s,y\}$ in Eq. (1.38). $H_n(x)$ are the Hermite polynomials, $w_{t/s}(z)$ is the spot size, $R_{t/s}(z)$ is the radius of curvature, and $\Psi_{t/s}(z)$ is the Gouy phase shift incurred by a Gaussian beam while propagating through its waist. These quantities are defined as:

$$w_t(z) = w_{0,t}\sqrt{1 + \left(\frac{z - z_{0,t}}{z_{R,t}}\right)^2} \tag{1.39}$$

$$R_t(z) = (z - z_{0,t})\left(1 + \left(\frac{z_{R,t}}{z - z_{0,t}}\right)^2\right) \tag{1.40}$$

$$\Psi_t(z) = \arctan\left(\frac{z - z_{0,t}}{z_{R,t}}\right) \tag{1.41}$$

where we have defined the Rayleigh range:

$$z_{R,t} = \frac{\pi w_{0,t}^2}{\lambda} \tag{1.42}$$

Hermite-Gauss modes are uniquely determined by their waists $w_{0,t/s}$ and their positions $z_{0,t/s}$ along the z-axis, which can be combined into the so-called beam parameter $q_{t/s}$:

$$q_{t/s}(z) = (z - z_{0,t/s}) - iz_{R,t}, \quad \frac{1}{q(z)} = \frac{1}{R_{t/s}(z)} + i\frac{\lambda}{\pi w_{t/s}^2(z)} \tag{1.43}$$

We will now list some of the key properties of Hermite-Gauss modes. For convenience, the following developments will assume $w_{0,t} = w_{0,s}$ and $z_{0,t} = z_{0,s}$ whenever beam astigmatism is not relevant to the point.

Hermite-Gaussian functions form a complete basis set of orthogonal functions:

$$\iint u_{n,m}(x,y)u^{\star}_{n',m'}(x,y)\,\mathrm{d}x\,\mathrm{d}y = \delta_{n,n'}\delta_{m,m'} \tag{1.44}$$

As such, they can be used to expand any paraxial optical beam obeying Eq. (1.36):

$$E(x,y,z,t) = \sum_{n,m} a_{n,m}u_{n,m}(x,y,z)\,e^{i\,(kz-\omega t)} \tag{1.45}$$

The intensity profile of a fundamental Gaussian beam $u_{0,0}(x,y,z)$ carrying a total power P is given by:

$$I(x,y,z) = \frac{2P}{\pi w(z)^2}e^{\frac{-2(x^2+y^2)}{w^2}} \tag{1.46}$$

Consequently, clipping losses when going though an aperture of diameter D amount to:

$$\mathcal{L}_{\mathrm{cl}} = e^{\frac{-2(D/2)^2}{w^2}} \tag{1.47}$$

Higher-order modes are larger than the fundamental mode, and therefore suffer higher clipping losses. Their waist can be approximated as $w_{n,m} \approx w_0\sqrt{n+m+1}$ [75].

The coupling coefficient from an incoming beam u_{in} to an outgoing beam u_{out} is defined as the overlap integral [76–78] :

$$\langle u_{\mathrm{in}}|u_{\mathrm{out}}\rangle = \iint u^{\star}_{\mathrm{in}}(x,y,z)u_{\mathrm{out}}(x,y,z)\,\mathrm{d}x\,\mathrm{d}y \tag{1.48}$$

such that the power coupling efficiency from the incoming to the outgoing beam is given by:

$$\eta = \left|\frac{\langle u_{\mathrm{in}}|u_{\mathrm{out}}\rangle}{\langle u_{\mathrm{in}}|u_{\mathrm{in}}\rangle}\right|^2 \tag{1.49}$$

When both the incoming and outgoing beams are Gaussian, Eq. (1.49) simplifies to:

$$\eta = \frac{4}{\left(\frac{w'}{w}+\frac{w}{w'}\right)^2 + \left(\frac{\pi w' w}{\lambda}\right)^2\left(\frac{1}{R'}-\frac{1}{R}\right)^2} \tag{1.50}$$

where w, w', R, R' are the waist and radius of curvature of the incoming and outgoing beams at a reference position along the z axis.

Hermite-Gauss transverse modes in Fabry Perot cavities

Here we summarize the main features that arise when considering transverse effects in Fabry-Perot cavities. We consider a cavity formed between two parabolic mirrors with radii of curvature $R_{c,1}$ and $R_{c,2}$ at positions z_1 and z_2 such that the length of the cavity is $L_c = z_2 - z_1$, illustrated in Fig. 1.4. Convenient parameters are the g factors, defined as :

$$g_i = 1 - \frac{L_c}{Rc,i} \tag{1.51}$$

The resonant mode or eigenmode of a Fabry-Perot cavity is defined as the beam whose transverse profile is conserved upon experiencing a round-trip through the cavity, described by its beam parameter q_c. This condition can be expressed by using

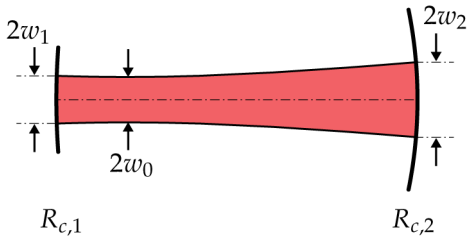

FIGURE 1.4: Sketch of a concave-concave Fabry-Perot cavity. The red beam represents the Gaussian-shaped fundamental eigenmode of the cavity.

the ABCD law [79]:

$$q_c = \frac{Aq_c + B}{Cq_c + D} \tag{1.52}$$

A, B, C, and D are the coefficients of the round trip ray transfer matrix $\mathbf{P}_{\text{cav}}$ for a cavity made of two mirrors with radii of curvature $R_{c,1}$ and $R_{c,2}$ separated by L_c :

$$\mathbf{P}_{\text{cav}} = \begin{pmatrix} A & B \\ C & D \end{pmatrix} = \mathbf{P}_{\text{mirror}}(R_{c,1})\mathbf{P}_{\text{space}}(L_c)\mathbf{P}_{\text{mirror}}(R_{c,2})\mathbf{P}_{\text{space}}(L_c) \tag{1.53}$$

The ray transfer matrices for reflection on a curved mirror and propagation through space are given by:

$$\mathbf{P}_{\text{mirror}}(R_c) = \begin{pmatrix} 1 & 0 \\ -\frac{2}{R_c} & 1 \end{pmatrix} \tag{1.54}$$

$$\mathbf{P}_{\text{space}}(L) = \begin{pmatrix} 1 & L \\ 0 & 1 \end{pmatrix} \tag{1.55}$$

Inserting Eqs. (1.54) and (1.55) into Eq. (1.53) and making use of Eq. (1.51) yields:

$$\mathbf{P}_{\text{cav}} = \begin{pmatrix} 2g_2 - 1 & 2L_c g_2 \\ -2\frac{g_2 - g_1(2g_2-1)}{L_c} & 2g_2(2g_1 - 1) - 1 \end{pmatrix} \tag{1.56}$$

The solution to Eq. (1.52) is then expressed as:

$$q_c = L_c \frac{-g_2(1-g_1) - i\sqrt{g_1 g_2(1 - g_1 g_2)}}{g_1 + g_2 - 2g_1 g_2} \tag{1.57}$$

Equation (1.57) fully defines the cavity eigenmodes. Notably their waist size w_0 can be written as:

$$w_0^2 = \frac{\lambda L_c}{\pi} \frac{\sqrt{g_1 g_2(1 - g_1 g_2)}}{g_1 + g_2 - 2g_1 g_2} \tag{1.58}$$

For the optical cavity to be stable, it is additionally required that the eigenmode has a real waist size, which is equivalent to $\text{Im}\{q_c\} = \pi w_0^2/\lambda > 0$. Using Eq. (1.57), the stability condition is expressed in terms of the g factors as:

$$0 \leq g_1 g_2 \leq 1 \tag{1.59}$$

The stability regime is represented graphically in g-space in Fig. 1.5, as well as the different values of g_1 and g_2 that can be achieved by varying the length of a FP cavity.

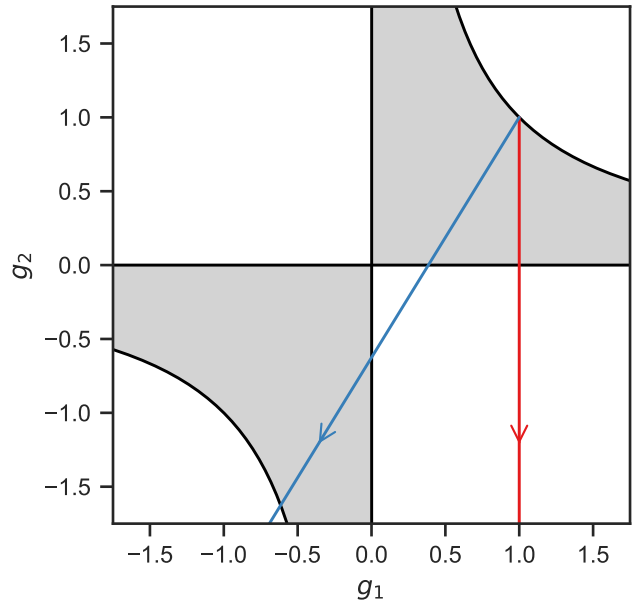

FIGURE 1.5: Stability diagram of a Fabry-Perot cavity. Red line: planar-concave cavity with $\mathrm{ROC}_1 = \infty$, $\mathrm{ROC}_2 = 28.5\,\mu\mathrm{m}$. Blue line: concave-concave cavity with $\mathrm{ROC}_1 = 92.2\,\mu\mathrm{m}$, $\mathrm{ROC}_2 = 56.7\,\mu\mathrm{m}$. The arrows show the direction of increasing L_{cav}.

Hermite-Gauss modes experience a Gouy phase shift, resulting in a modified round-trip phase shift ϕ compared to the plane-wave model:

$$\begin{aligned}\phi &= kL_c - \left(\frac{1}{2}+n\right)(\Psi_t(z_2)-\Psi_t(z_1)) - \left(\frac{1}{2}+m\right)(\Psi_s(z_2)-\Psi_s(z_1)) \\ &= kL_c - \left(\frac{1}{2}+n\right)\arccos(\sqrt{g_{1,t}\,g_{2,t}}) - \left(\frac{1}{2}+m\right)\arccos(\sqrt{g_{1,s}\,g_{2,s}})\end{aligned} \tag{1.60}$$

Some features of the cavity resonances $\phi = q\pi$ are noteworthy. The phase difference between resonant modes of successive transverse order, or higher order mode separation frequency [71], is:

$$\delta_{\mathrm{ho}} = 2\arccos(\sqrt{g_1\,g_2}) \tag{1.61}$$

In the case when the cavity eigenmodes are astigmatic, there also exist a fine splitting between higher-order modes of the same order. Finally, higher-order modes of longitudinal order $q-1$ can become resonant with the fundamental mode of order q, with the resonance condition given by [75] :

$$(n+m)\arccos(\sqrt{g_1\,g_2}) = \pi \tag{1.62}$$

1.1.4 Describing real-life fiber cavities

In order to understand the behavior or real-life FP cavities, misalignments and deviations of the mirrors from perfect parabolas, resulting in imperfect mode-matching and diffraction losses, must be taken into account. When the FP cavity is defined between two fiber mirrors, forming a fiber Fabry-Perot cavity (FFPC) [41], some additional complexity is introduced.

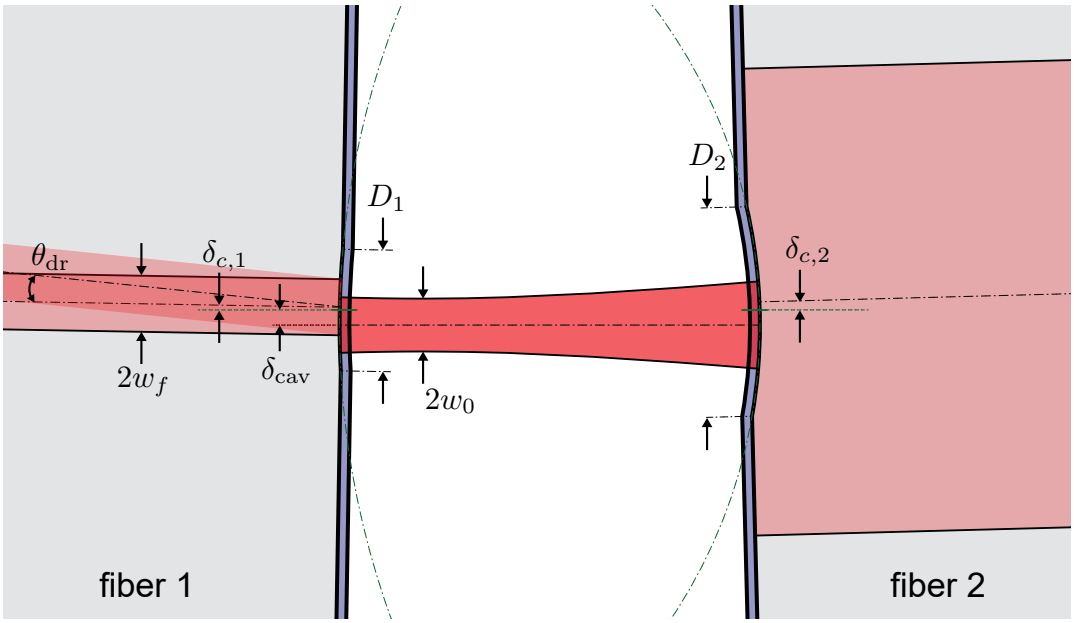

FIGURE 1.6: Sketch of a real life fiber-based Fabry-Perot cavity, to scale, with exaggerated misalignments.

Misalignments and mode-matching

Here we summarize the effects of misalignments and mode-matching imperfections on the behavior of a FFPC, based on the detailed description given in [78]. We consider the FFPC sketched in Fig. 1.6, formed between a single-mode fiber mirror (SMF, fiber 1) and a multimode fiber mirror (MMF, fiber2), which corresponds to the experimental setup introduced in the next chapters. The SMF is used to both couple light into the FP cavity and collect the reflected beam via the fiber mode with waist size w_f. The MMF is used to collect the transmitted beam, ensuring near perfect coupling efficiency regardless of misalignments. The mirror shapes are parabolic with a finite outer diameter D_i, and with an offset $\delta_{c,i}$ between the center of the parabola and the center of the fiber mode. Fiber 2 is additionally laterally offset by δ_f.

These geometrical misalignments lead to misalignments between the different optical beams, namely the SMF fiber mode, the beam directly reflected by the backside of the mirror, and the beam reflected from the FP cavity. The fiber mode and the directly reflected beam are misaligned by a tilt angle $\theta_{\mathrm{dr}} = 2\arcsin(\delta_c/R_{c,1})$. The directly reflected beam additionally experiences an increase in propagation length given by $\Delta l_{\mathrm{dr}} = 2R_{c,1}(1-\cos(\theta_{\mathrm{dr}}/2))$. The input beam and the cavity mode are misaligned by a lateral offset $\delta_{\mathrm{cr}} = \delta_{c,1} - \delta_{\mathrm{cav}}$ and a tilt angle θ_{cav}, with:

$$\theta_{\mathrm{cav}} = \arctan\left(\frac{2\,\delta_f}{2L_c - R_{c,1} - R_{c,2}}\right) \approx \frac{2\,\delta_f}{2L_c - R_{c,1} - R_{c,2}} \tag{1.63}$$

$$\delta_{\mathrm{cav}} = -\frac{R_{c,1}}{2}\sin(\theta_{\mathrm{cav}}) \approx \frac{2\,\delta_f\,R_{c,1}}{2L_c - R_{c,1} - R_{c,2}} \tag{1.64}$$

The beam reflected from the cavity additionally experiences an increase in propagation length given by:

$$\Delta l_{\mathrm{cr}} = -\frac{R_{c,1}}{2}(1-\cos(\theta_{\mathrm{cav}})) \approx \frac{2\,\delta_f^2\,R_{c,1}}{(2L_c - R_{c,1} - R_{c,2})^2} \tag{1.65}$$

Adopting the naming convention from [78], we define $\beta = |\beta| \exp(i\xi_\beta)$ as the mode-matching coefficient between the fiber mode and the directly reflected beam, and $\alpha = |\alpha| \exp(i\xi_\alpha)$ as the the mode-matching coefficient between the fiber mode and the beam reflected from the cavity. The phase of α and β is related to the additional propagation lengths Δl_{cr} and Δl_{dr} by:

$$\xi_\alpha = n_f \, k \, \Delta l_{\mathrm{cr}} \tag{1.66}$$

$$\xi_\beta = n_f \, k \, \Delta l_{\mathrm{dr}} \tag{1.67}$$

where n_f is the refractive index of the optical fibers. The amplitude of α and β is expressed as:

$$|\alpha|^2 = \tau_{a,\mathrm{cr}}^2 \exp\left(-\frac{\theta_{\mathrm{cav}}}{\theta_{e,\mathrm{cr}}}\right) \exp\left(-\frac{\delta_{\mathrm{cr}}}{d_{e,\mathrm{cr}}}\right) \tag{1.68}$$

$$|\beta|^2 = \tau_{a,\mathrm{dr}}^2 \exp\left(-\frac{\theta_{\mathrm{dr}}}{\theta_{e,\mathrm{dr}}}\right) \tag{1.69}$$

The coupling efficiencies $\tau_{a,\mathrm{dr/cr}}$, the angular tolerances $\theta_{e,\mathrm{dr/cr}}$ and the axial tolerance $d_{e,\mathrm{cr}}$ are defined following [76] :

$$\tau_{a,\mathrm{cr}}^{-1} = \frac{1}{2} \sqrt{\left(\frac{w_2}{w_f} + \frac{w_f}{w_2}\right)^2 + \left(\frac{k \, w_2 w_f}{2R_{\mathrm{cr}}}\right)^2} \tag{1.70}$$

$$\theta_{e,\mathrm{cr}}^{-1} = \frac{1}{2^{3/2}} \, k \, \tau_{a,\mathrm{cr}} \sqrt{w_2^2 + w_f^2} \tag{1.71}$$

$$d_{e,\mathrm{cr}}^{-1} = \frac{1}{\sqrt{2}} \, \tau_{a,\mathrm{cr}} \sqrt{\frac{1}{w_2^2} + \frac{1}{w_f^2} + \left(\frac{k \, w_2}{2R_{\mathrm{cr}}}\right)^2} \tag{1.72}$$

$$\tau_{a,\mathrm{dr}}^{-1} = \frac{1}{2} \sqrt{4 + \left(\frac{k \, w_f^2}{2R_{\mathrm{dr}}}\right)^2} \tag{1.73}$$

$$\theta_{e,\mathrm{dr}}^{-1} = \frac{1}{2} \, k \, \tau_{a,\mathrm{dr}} \, w_f \tag{1.74}$$

where we defined $R_{\mathrm{dr}} = R_{c,1}/(2n_f)$ and $R_{\mathrm{cr}} = R_{c,1}/(n_f - 1)$ as the radius of curvature of the directly reflected and cavity reflected beams, taking into account the lensing effect at the curved mirror interface.

In contrast with free-space FP cavities, where mode-matching optics are used, the mode-matching between the input beam and the cavity mode in a FFPC is fully determined by the waist size of the fiber mode, the waist size of the cavity mode, and misalignments [41]. In addition, due to directly reflected and cavity reflected beams being collected through the fiber mode to yield the full reflection signal, the expressions for cavity response in reflection must be modified. Equation (1.10) becomes:

$$E_r = E_i \, \frac{\beta r_1 - r_2 \left(\beta r_1^2 + \alpha^2 t_1^2\right) e^{i\,2\phi}}{1 - r_1 r_2 \, e^{i\,2\phi}} \tag{1.75}$$

and Eq. (1.13) becomes:

$$\frac{P_r}{P_i} \sim A - B \frac{(\kappa/2)^2}{(\kappa/2)^2 + \Delta^2} - C \frac{\Delta \; \kappa/2}{(\kappa/2)^2 + \Delta^2} \tag{1.76}$$

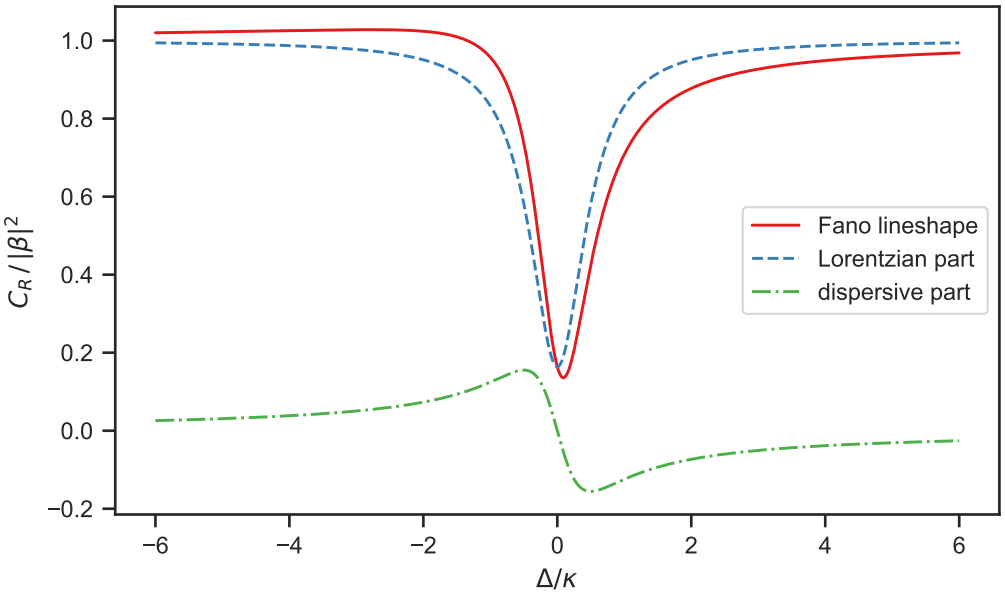

FIGURE 1.7: Reflection lineshape of a fiber-based Fabry Perot cavity. The red curve is the full Eq. (1.76) while the blue and green curves show the Lorentzian and dispersive parts.

with

$$\begin{aligned} A &= |\beta|^2 \\ B &= |\alpha|^2 |\beta| \frac{\kappa_{ex,1}}{\kappa/2} \left(2\cos(\xi) - \frac{|\alpha|^2}{|\beta|} \frac{\kappa_{ex,1}}{\kappa/2} \right) \\ C &= 2\,|\alpha|^2 |\beta| \frac{\kappa_{ex,1}}{\kappa/2} \sin(\xi) \\ \xi &= \xi_\beta - 2\,\xi_\alpha \end{aligned} \tag{1.77}$$

The modified cavity lineshape in reflection (plotted in Fig. 1.7) includes a dispersive part, which stems from a the phase-mismatch between the directly reflected and cavity reflected beams, and is a unique feature of FFPCs as highlighted in [78]. The lineshape of the circulating and transmitted field is not modified, with the mode-matching coefficients only coming in as prefactors.

The mixing matrix formalism

In realistic cavities, the mirrors are not perfect infinite parabolas. Their finite diameter, their shape deviating from parabolic, and the roughness of their surface all lead to the cavity eigenmodes deviating from pure Hermite-Gauss modes. Here we introduce the mode-mixing formalism [75, 80], which allows to numerically calculate the modified eigenmodes of cavities formed between imperfect mirrors.

The action of each cavity mirror on the cavity field can be expressed in the basis of Hermite Gauss modes as a mixing matrix $\mathbf{M}$, which coefficients are the overlap between an outgoing mode $u_{n,m}(x, y; q_{\text{out}})$ with beam parameter q_{out}, and an incoming mode $u_{n',m'}(x, y, q_{\text{in}}) \exp(-2ik\Delta(x, y))$, where $\Delta(x, y)$ is the height profile of the mirror:

$$\mathbf{M}_{i,j} = k_{(n,m),(n',m')} = \iint u_{n,m}(x, y; q_{\text{out}}) u^{\star}_{n',m'}(x, y; q_{\text{in}}) \exp(2i\,k\,\Delta(x, y))\,\mathrm{d}x \tag{1.78}$$

Using the unfolded cavity representation [79] is convenient since it allows one to use only forward-propagating Hermite-Gauss modes, simplifying the calculations. The incoming and outgoing beam parameters for a mirror located at distance Δz from the waist of the Hermite-Gauss mode are then given by:

$$q_{\text{in}} = \frac{1}{R(\Delta z)} + i\frac{\lambda}{\pi w^2(\Delta z)}, \quad q_{\text{out}} = \frac{-1}{R(\Delta z)} + i\frac{\lambda}{\pi w^2(\Delta z)} \tag{1.79}$$

The mixing matrix corresponding to a round-trip through the cavity is:

$$\mathbf{M}_{\text{cav}} = \exp(2\,i\,k\,L_{\text{cav}})\,\mathbf{M}_{\text{m1}}\mathbf{M}_{\text{m2}} \tag{1.80}$$

where $\mathbf{M}_{\text{m1}}$ and $\mathbf{M}_{\text{m2}}$ are the mixing matrices for mirrors 1 and 2 respectively. The properties of the transverse resonances of the cavity are obtained by solving the eigensystem $\gamma_i\,|\Phi_i\rangle = \mathbf{M}_{\text{cav}}\,|\Phi_i\rangle$.

The cavity transverse eigenmodes are given by the eigenvectors $\Phi_i = \sum_n c_{i,n}u_n(x)$. Since $\mathbf{M}_{\text{cav}}$ is normal and unitary, the eigenvectors form a new complete orthonormal basis. An input mode Φ_{in} can therefore be expanded in this basis, and the coefficients of this expansion are the coupling efficiencies from the input mode into the cavity eigenmodes. The associated eigenvalues contain the losses $1 - |\gamma_i|^2$ and phase shift $\arg(\gamma_i)$ experienced by the corresponding eigenmode during a cavity round-trip.

In the case of perfect parabolic mirrors, $\Delta(x,y) = (x^2+y^2)/(2R_{c,i})$ with $R_{c,i} = R(\Delta z_i)$, and the mixing matrices can be calculated analytically. They take a diagonal shape, leading to $\mathbf{M}_{\text{cav},n,n'} = \delta_{n,n'}\exp\big(2\,i\big(kL_{\text{cav}} + \big(\frac{1}{2}+n\big)(\Psi(\Delta z_1)+\Psi(\Delta z_2))\big)\big)$. The solutions to this eigensystem are the pure Hermite-Gauss modes, consistent with the standard theory for FP cavities.

Fiber mirrors often have a gaussian shape [41], leading to strong mode-mixing effects described in [75]. The nature and the impact of these effects in our FFPCs are discussed in detail in 4.3.2.

1.2 Mechanical Resonators in Fabry-Perot Cavities

In this section we summarize the fundamental properties of mechanical resonators, and present the key characteristics of the interaction between the eigenmodes of a FP cavity and a mechanical resonator inserted in-between its two mirrors.

1.2.1 Fundamental properties of mechanical resonators

Here we list the basic properties of the vibrational modes of a mechanical elements, focusing on the example of a circular drum resonator of micrometric dimensions.

The main characteristics of the vibrational modes (or eigenmodes) of a mechanical resonator are their resonance frequency, quality factor and effective mass, which are determined by its geometry and by the material it is made of. A given vibrational mode of a mechanical resonator can be modeled as an harmonic resonator with a mechanical susceptibility of:

$$\chi_m(\Omega) = \frac{1}{m_{\text{eff}}(\Omega_m^2 - \Omega^2 - i\Omega\Gamma_m)} \tag{1.81}$$

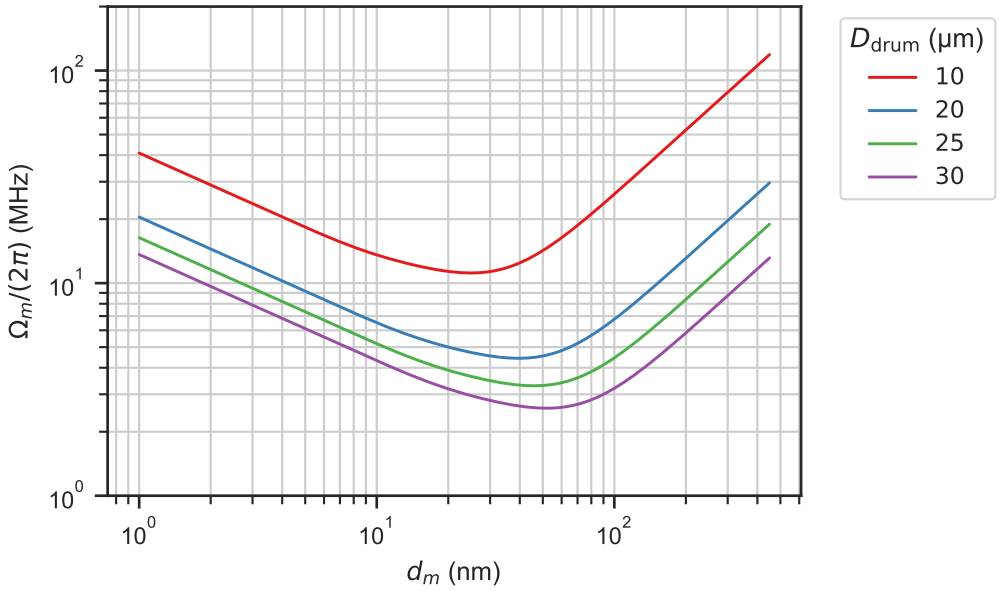

FIGURE 1.8: Fundamental mechanical resonance frequency of a stretched circular plate as a function of thickness, for various values of the drum diameter.

where m_{eff} is the effective mass associated with the mode, Ω_m the resonance frequency of the mode, and Γ_m the rate at which the mechanical mode loses energy, related to the quality factor Q_m by $Q_m = \Omega_m/\Gamma_m$.

The resonance frequency of a mode of order (n,m) of a stretched circular plate of radius r and thickness t are given by [64, 81] :

$$\Omega_{m,(n,m)} = 2\pi\left(k_{(n,m)}r\right)\sqrt{\frac{D_p}{\rho_{2D}\,r^4}\left(\left(k_{(n,m)}r\right)^2 + \frac{\gamma\,r^2}{D_p}\right)} \tag{1.82}$$

where ρ_{2D} is the areal density, γ is the tension per unit length, $D_p = \frac{E\,t^3}{12(1-\nu^2)}$ the flexural rigidity, E the Young's modulus, ν the Poisson ratio, and $k_{(n,m)}$ a calculated parameter which depends on $x = (\gamma\,r^2)/D_p$ as follows :

$$\left(k_{(n,m)}r\right)(x) = \alpha + (\beta-\alpha)\exp(-\eta\exp(\delta\ln(x))) \tag{1.83}$$

The model parameters α, β, δ, η are numerically calculated in [81].

Depending on the value of γ and D_p, which vary in particular with the thickness t, the behavior of a stretched plate changes from membrane-like to plate-like. This is relevant for the drums made of few-layer hBN used in this work because their typical thickness places them at the transition between the membrane-like and plate-like regimes. The fundamental mechanical frequency $\Omega_{m,(0,0)}$ is plotted as a function of drum thickness and for various values of drum radius in Fig. 1.8, using material properties for hBN taken from [64].

Energy losses in mechanical resonators can occur through a number of processes,

some of them internal to the resonator, while others are of external origin [82]. Contributions to the mechanical quality factor can be decomposed as follows:

$$\frac{1}{Q_m} = \frac{1}{Q_{\text{int}}} + \frac{1}{Q_{\text{medium}}} + \frac{1}{Q_{\text{clamp}}} + \frac{1}{Q_{\text{other}}} \tag{1.84}$$

Q_{int} is the intrinsic quality factor, determined by material properties. Q_{medium} contains losses due to the interaction with the medium in which the mechanical resonator oscillates, for instance gas damping. Q_{clamp} contains losses due to energy leaking into the support to which the mechanical resonator is attached. Q_{other} represents all other loss mechanisms, for instance Eddy current damping.

1.2.2 The membrane-in-the-middle system

When a mechanical resonator is placed within an optical cavity, it forms a variation of the generic optomechanical system called a membrane-in-the-middle (MIM) [1, 83]. The mechanical resonator can interact with the optical cavity either dispersively if the resonance frequency of the cavity depends on its position and/or dissipatively if the cavity losses depend on its position.

We consider a membrane of refractive index n_m and thickness d_m, whose center is positioned at a distance z_m from the left cavity mirror. The fundamental properties of the MIM system are well captured by a 1D plane-wave model [84], sketched in Fig. 1.9, and its transmission and reflection coefficients can be calculated using the coupling matrix formalism introduced in Section 1.1.1.

The air-membrane interfaces are well-described by the Fresnel equations, leading to the following coupling matrices for the air to membrane and membrane to air interfaces:

$$\mathbf{C}_{m,\text{f}} = \frac{1}{t_{m,\text{f}}}\begin{pmatrix} 1 & -r_{m,\text{b}} \\ r_{m,\text{f}} & 1 \end{pmatrix}, \quad \mathbf{C}_{m,\text{b}} = \frac{1}{t_{m,\text{b}}}\begin{pmatrix} 1 & -r_{m,\text{f}} \\ r_{m,\text{b}} & 1 \end{pmatrix} \tag{1.85}$$

The Fresnel coefficients are given by:

$$r_{m,\text{b}} = -r_{m,\text{f}} = \frac{1-n_m}{1+n_m}, \quad t_{m,\text{b}} = n_m\, t_{m,\text{f}} = \frac{2n_m}{1+n_m} \tag{1.86}$$

The coupling matrix for the membrane can then be calculated as:

$$\mathbf{C}_{\text{m}} = \mathbf{C}_{m,\text{b}}\, \mathbf{C}_{\text{space}}(d_m, n_m)\, \mathbf{C}_{m,\text{f}} = \frac{i}{t_m}\begin{pmatrix} -1 & r_m \\ -r_m & r_m^2 + t_m^2 \end{pmatrix} \tag{1.87}$$

with $\mathbf{C}_{\text{space}}$ given by Eq. (1.8). The complex reflection and transmission coefficients of the membrane are given by:

$$r_m = \frac{(n_m^2 - 1)\, \sin(k\, n_m d_m)}{2i\, n_m \cos(k\, n_m\, d_m) + (1 + n_m^2)\, \sin(k\, n_m d_m)} \tag{1.88}$$

$$t_m = \frac{2n_m}{2i\, n_m \cos(k\, n_m d_m) + (1 + n_m^2)\, \sin(k\, n_m d_m)} \tag{1.89}$$

Finally, the coupling matrix for the full MIM system is:

$$\mathbf{C}_{\text{MIM}} = \mathbf{C}_{\text{mirror},2}\, \mathbf{C}_{\text{space}}(L_2, 1)\, \mathbf{C}_{\text{m}}\, \mathbf{C}_{\text{space}}(L_1, 1)\, \mathbf{C}_{\text{mirror},1} \tag{1.90}$$

with $L_1 = z_m - d_m/2$ and $L_2 = L_c - d_m/2 - z_m$.

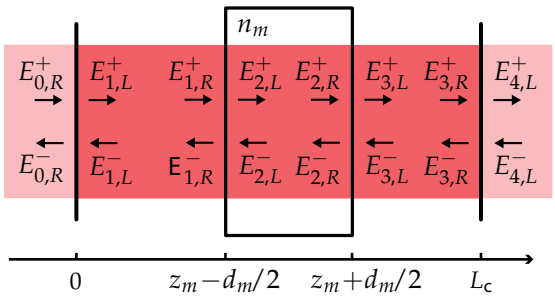

FIGURE 1.9: Sketch of a planar-planar MIM system. The fields are defined in similar fashion than in 1.1. The membrane is defined as a dielectric slab of refractive index n_m and thickness d_m, whose center is positioned at a distance z_m from the left cavity mirror.

The intensity reflection coefficient of a MIM system obtained by solving Eq. (1.90) is plotted as a function of membrane position and cavity detuning in Fig. 1.10, displaying the dispersive effect of the membrane position on the cavity resonances. The left, middle, and right columns respectively correspond to the membrane being positioned close to the left mirror, in the center of the cavity, and close to the right mirror. The top and bottom rows respectively correspond to the detuning being achieved by varying the angular frequency or the cavity length.

Importantly, Fig. 1.10 demonstrates graphically that the angular frequency and cavity length degrees of freedom are not equivalent in a MIM system. The slanting observed in the dispersive behavior in the top row is due to the position of the membrane. Conversely, the slanting observed in the bottom row is due to the definition of L_1 and L_2, which correspond here to the right mirror being moved in order to vary the cavity detuning, matching the experimental system considered. Defining $L_1 = L_c/2 - t/2 + z_m$ and $L_2 = L_c/2 - t/2 - z_m$ (corresponding to the left and right mirror being moved symmetrically around the membrane to vary the cavity detuning) makes the slanting in the bottom row disappear, while the direction of this slanting is reversed in the case where the left mirror is moved. This consideration becomes important when trying to estimate the dispersive optomechanical coupling from experimental data, as discussed in Section 5.2.2.

Even though a general analytical expression for the resonance condition of the MIM system has yet to be found, reasonably good approximations have been developed, assuming a lossless membrane such that $\mathrm{Im}\{n_m\} \approx 0$ [84, 85]. The approximate expression for the resonance condition in terms of cavity length when only the right mirror is moved is:

$$L_{q,\mathrm{MIM}} = q\frac{\lambda}{2} + \frac{\lambda}{2\pi}\arctan\left(\frac{\cos(\phi_r) + |r_m|\,\cos(2\,k\,z_m)}{\sin(\phi_r) - |r_m|\,\sin(2\,k\,z_m)}\right) \tag{1.91}$$

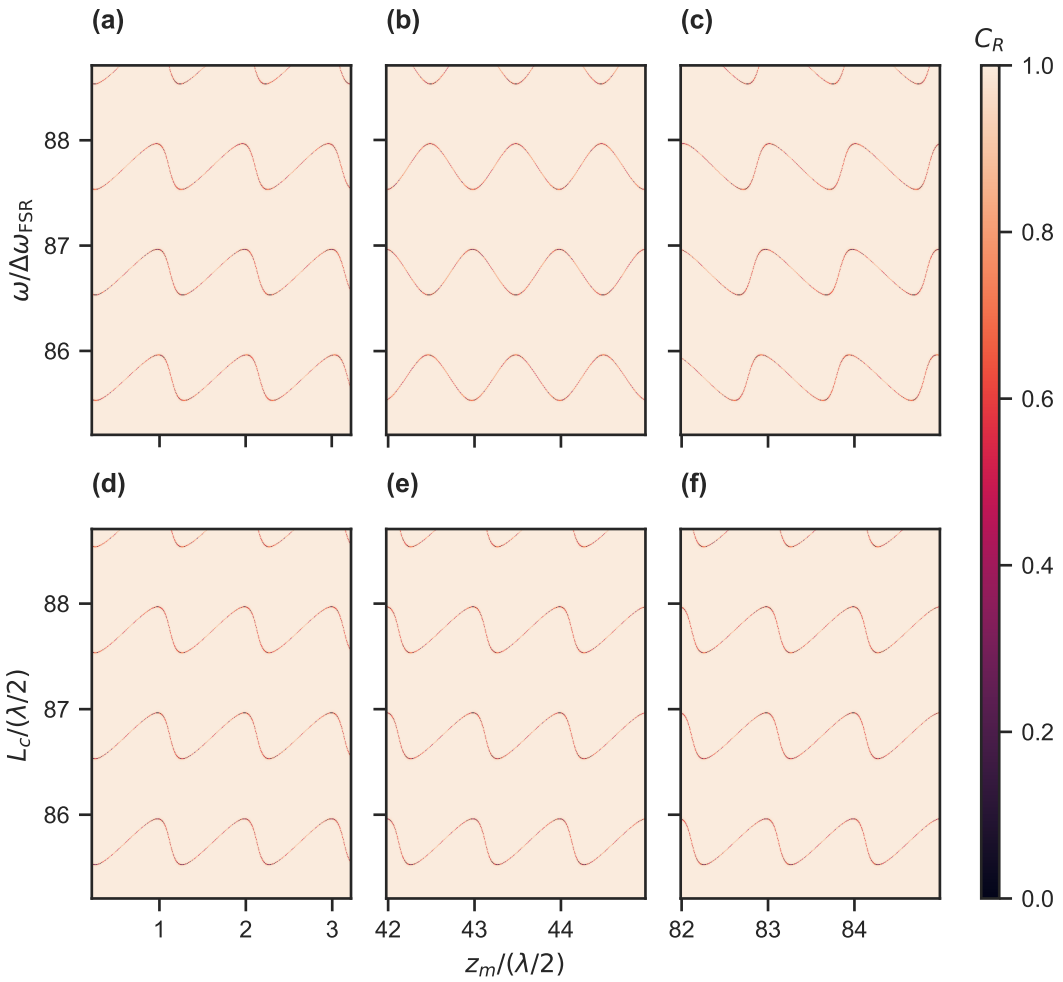

FIGURE 1.10: Plot of the simulated reflection signal of a MIM system when the cavity detuning and membrane position are varied, calculated by solving Eq. (1.90). **(a,d)**, **(b,e)**, **(c,f)**: membrane next to the left mirror, in the middle of the cavity, and next to the right mirror, respectively. **(a,b,c)**, **(d,e,f)**: cavity detuning varied by changing the angular frequency, and the cavity length, respectively

The approximate expressions for the resonance condition in terms of angular frequency, depending on the position of the membrane and under the additional assumption that $L_{\mathrm{MIM}} \gg \lambda/2$, are:

$$\omega_{q,\mathrm{MIM}} = q\Delta\omega_{\mathrm{FSR}} + \frac{\Delta\omega_{\mathrm{FSR}}}{\pi}\arctan\left(\frac{\cos(\phi_r) + |r_m|\,\cos(2\,k\,\delta z_m)}{\sin(\phi_r) - |r_m|\,\sin(2\,k\,\delta z_m)}\right), \quad z_{m,0} \to 0 \tag{1.92}$$

$$\omega_{q,\mathrm{MIM}} = q\Delta\omega_{\mathrm{FSR}} + \frac{\Delta\omega_{\mathrm{FSR}}}{\pi}(\arccos(-|r_m|\cos(2\,k\,\delta z_m)) - \phi_r), \quad z_{m,0} \to L_c/2 \tag{1.93}$$

$$\omega_{q,\mathrm{MIM}} = q\Delta\omega_{\mathrm{FSR}} + \frac{\Delta\omega_{\mathrm{FSR}}}{\pi}\arctan\left(\frac{\cos(\phi_r) + |r_m|\,\cos(2\,k\,\delta z_m)}{\sin(\phi_r) + |r_m|\,\sin(2\,k\,\delta z_m)}\right), \quad z_{m,0} \to L_c \tag{1.94}$$

where we have defined δz_m and $z_{m,0}$ such that $z_m = z_{m,0} + \delta z_m$.

The linear dispersive effect is characterized by the frequency pull parameter, defined as :

$$G = \frac{\partial\omega_c}{\partial z_m} \tag{1.95}$$

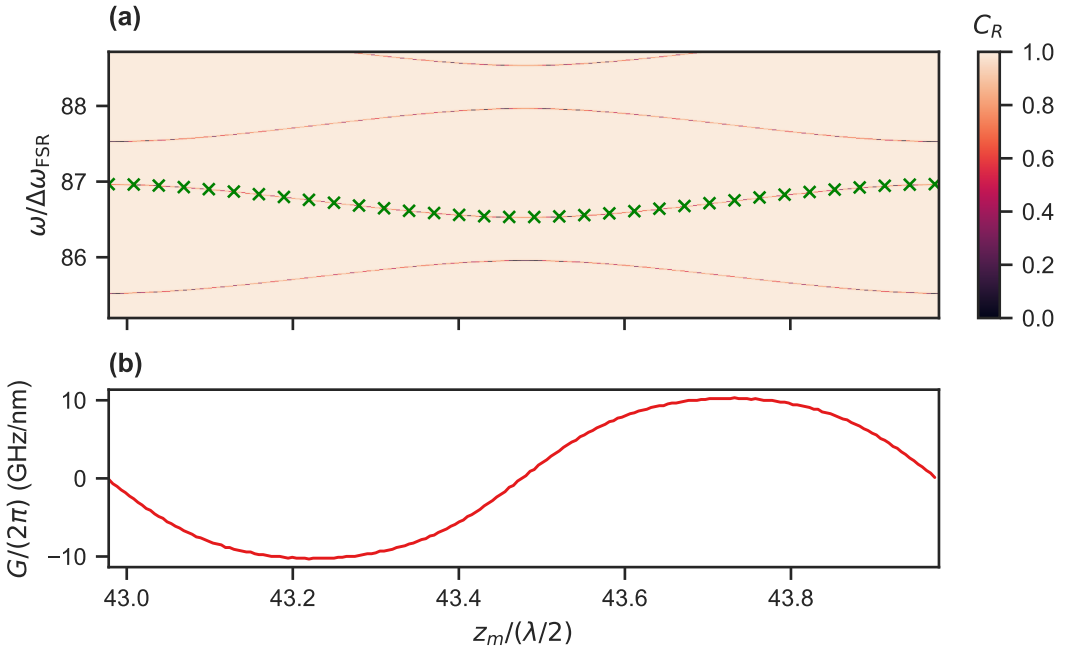

FIGURE 1.11: **(a)**: MIM system transmission coefficient, calculated by solving Eq. (1.90). Green markers track the frequency of a specific resonance as a function of membrane position. **(b)**: frequency pull parameter as a function of membrane position, calculated by differentiating the resonant frequencies extracted from (a).

G is plotted in Fig. 1.11 in the case when the membrane is in the middle of the cavity. The maximum value of the linear dispersive effect is achieved when the membrane is positioned between a node and an antinode of the intracavity field. In contrast, the quadratic dispersive coupling $G^{(2)} = \partial^2\omega_c/\partial z_m^2$ is maximum when the membrane is positioned at a node or at an antinode.

When optical absorption in the membrane is non-zero, when the membrane causes scatter losses, or when the losses in the cavity mirrors are asymmetric, the position of the membrane additionally modifies losses in the MIM system, leading to a dissipative coupling $G_\kappa = \partial\kappa/\partial z_m$ [86].

More advanced effects such as membrane tilt and higher-order modes can be included by expanding on the scattering model [86], or by using a perturbation approach [83, 87, 88].

1.2.3 Dynamical optomechanical effects

The dispersive and dissipative effects of the position of the membrane on the cavity resonance are signatures of the radiation-pressure induced optomechanical coupling between the mechanical vibration modes of the membrane and the optical cavity mode. Here we present some key features of the dynamical optomechanical interaction, otherwise comprehensively reviewed in [1].

We consider small variations of the position of the mechanical resonator around its center position, and linear variations of the linewidth and frequency of the cavity resonance due the motion of the mechanical resonator. We will note the displacement of the mechanical resonator as x here for consistency with the existing literature. The dynamical behavior of the optomechanical system is conveniently

described within the quantum formalism, using the general optomechanical Hamiltonian :

$$\mathcal{H} = -\hbar\omega_c \hat{a}^\dagger \hat{a} + \hbar\Omega_m \hat{b}^\dagger \hat{b} - \hbar g_0 (\hat{b} + \hat{b}^\dagger)\hat{a}^\dagger \hat{a} + i\hbar\sqrt{\eta_{c,1}\kappa}(s_{\text{in}}\hat{a}^\dagger - s_{\text{in}}\hat{a}) \tag{1.96}$$

where $\hat{a}$ in the number of photons in the cavity mode, $\hat{b}$ the number of phonons in the mechanical mode, s_{in} is a driving term and $g_0 = G\, x_{\text{zpf}} = G\sqrt{\hbar/(2\, m_{\text{eff}}\, \Omega_m)}$ is the vacuum optomechanical coupling strength, defined as the shift in cavity resonance frequency due to a single phonon.

The dynamical behavior of the optical cavity field and of the position of the mechanical resonator are described by the Heisenberg equations. We place ourselves in the classical regime, omitting statistical noise terms, and considering a classical driving field $s_{\text{in}}(t) = (\bar{s}_{\text{in}} + \delta s_{\text{in}}(t))\exp(-i\omega_l t)$. We additionally consider the case when $\bar{s}_{\text{in}}$ is large enough that the number of photons and the number of phonons can be linearized around their steady-state values: $a(t) = \bar{a} + \delta a(t)$, and $x(t) = \bar{x} + \delta x(t)$. Under these assumptions, the coupled equations of motion for the system, expressed in the rotating frame at angular frequency ω_l, read:

$$\frac{\mathrm{d}\delta a(t)}{\mathrm{d}t} = \left(i\Delta - \frac{\kappa}{2}\right)\delta a(t) - iG\bar{a}\delta x(t) + \sqrt{\eta_c\kappa}\,\delta s_{\text{in}}(t) \tag{1.97}$$

$$\frac{\mathrm{d}^2\delta x(t)}{\mathrm{d}t^2} + \Gamma_m \frac{\mathrm{d}\delta x(t)}{\mathrm{d}t} + \Omega_m^2 \delta x(t) = -\frac{\hbar G}{m_{\text{eff}}}\bar{a}(\delta a(t) + \delta a^\dagger(t)) \tag{1.98}$$

The steady state values for the cavity field and for the position of the mechanical resonator are given by:

$$\bar{a} = \frac{\sqrt{\eta_c\kappa}}{-i\Delta + \kappa/2}\bar{s}_{\text{in}} \tag{1.99}$$

$$\bar{x} = \frac{\bar{a}^2}{m_{\text{eff}}\Omega_m^2} \tag{1.100}$$

where we redefined the cavity detuning as $\Delta = (\omega_l - \omega_c) - G\bar{x}$ to include the static shift due to the radiation-pressure interaction. The number of photons in the optical cavity is given by $n_{\text{cav}} = P_{\text{circ}}/(\hbar\omega_l)$.

We now consider the case of a phase-modulated input $\delta s_{\text{in}}(t) = s_p^+ \exp(-i\Omega t) + s_p^- \exp(i\Omega t)$. The strong carrier modifies the behavior of the mechanical resonator, which in turn modifies the susceptibility of the cavity to the sidebands. Both the modified mechanical susceptibility and the modified cavity response can be characterized to measure the optomechanical coupling strength. Here we summarize the presentation of these effects made in [89].

We search for solutions to Eqs. (1.97) and (1.98) under the form:

$$\delta a(t) = A^+ \exp(-i\Omega t) + A^- \exp(i\Omega t) \tag{1.101}$$

$$\delta x(t) = X^+ \exp(-i\Omega t) + X^- \exp(i\Omega t) \tag{1.102}$$

Inserting Eqs. (1.101) and (1.102) in Eqs. (1.97) and (1.98) yields after some manipulation:

$$\chi_c^{-1}(\Delta+\Omega)\,A^+ = -iG\bar{a}X + \sqrt{\eta_c\kappa}s_p^+ \tag{1.103}$$

$$\left(\chi_c^{-1}(\Delta-\Omega)\,A^-\right)^\star = iG\bar{a}X + \sqrt{\eta_c\kappa}s_p^- \tag{1.104}$$

$$\chi_m^{-1}(\Omega)\,X = -\hbar\bar{a}\left(A^+ + (A^-)^\star\right) \tag{1.105}$$

Solving for X in Eqs. (1.103) to (1.105) gives:

$$X = -\hbar G\bar{a}\sqrt{\eta_c\kappa}(s_p^+\chi_c(\Delta+\Omega) + s_p^-\chi_c(\Omega-\Delta))\chi_{m,\mathrm{eff}}(\Omega) \tag{1.106}$$

The modified mechanical susceptibility $\chi_{m,\mathrm{eff}}$ is expressed as:

$$\chi_{m,\mathrm{eff}}^{-1}(\Omega) = \chi_m^{-1}(\Omega) + \Sigma(\Omega) \tag{1.107}$$

with:

$$\Sigma(\Omega) = -2i\,m_{\mathrm{eff}}\,\Omega_m\,g^2(\chi_c(\Delta+\Omega) - \chi_c(\Omega-\Delta)) \tag{1.108}$$

where we used $\hbar G^2\bar{a}^2 = 2m_{\mathrm{eff}}\Omega_m g^2$ and $g = g_0\sqrt{n_{\mathrm{cav}}}$. The term $\Sigma(\Omega)$ captures the optical spring and the optomechanical damping effects [90, 91], which are the effective modifications of the mechanical resonance frequency and linewidth due to the radiation-pressure force. When the dissipative optomechanical coupling is taken into account, additional terms appear in the expression for $\Sigma(\Omega)$ [60, 86].

Solving for A^+ and A^- in Eqs. (1.103) to (1.105) gives:

$$A^\pm = \sqrt{\eta_c\kappa}\,\chi_{c,\mathrm{eff}}(\Delta\pm\Omega)s_p^\pm \tag{1.109}$$

The modified cavity susceptibility $\chi_{c,\mathrm{eff}}$ is expressed as:

$$\chi_{c,\mathrm{eff}}(\Omega) = \chi_c(\Omega)\,K(\Omega-\Delta) \tag{1.110}$$

with:

$$K(\Omega) = \frac{\chi_m^{-1}(\Omega)}{\chi_{m,\mathrm{eff}}^{-1}(\Omega)} \tag{1.111}$$

Each sideband is filtered by the cavity with a modified cavity response due to the radiation-pressure interaction. The term $K(\Omega)$ captures the optomechanically induced transparency window effect (OMIT) [91–95].

The fields reflected and transmitted by the MIM system can be expressed using the input-output formalism as $a_{\mathrm{out},R} = s_{\mathrm{in}}(t) - \sqrt{\kappa_{\mathrm{ex},1}}\,a(t)$ and $a_{\mathrm{out},T} = \sqrt{\kappa_{\mathrm{ex},2}}\,a(t)$. In the case when the sidebands are generated through phase-modulation, we have $\bar{s}_{\mathrm{in}} = J_0(\beta)s_l$ and $s_p^+ = -s_p^- = J_1(\beta)s_l$. Defining $F_{\mathrm{eff}}(\Omega) = 1 - \kappa_{\mathrm{ex},1}\chi_{c,\mathrm{eff}}(\Omega)$ and following the same steps as in Section 1.1.2 yields:

$$V_{\mathrm{PD},\Omega}^I + i\,V_{\mathrm{PD},\Omega}^Q = 2P_0J_0(\beta)J_1(\beta)\eta_{\mathrm{PD}}(F^\star(\Delta)F_{\mathrm{eff}}(\Delta+\Omega) - F(\Delta)F_{\mathrm{eff}}^\star(\Delta-\Omega)) \tag{1.112}$$

Equation (1.112) describes the signal measured by a vector network analyzer scanning the frequency of the phase-modulation sideband at Ω while measuring the reflection from a MIM system. Fitting the data obtained in such a measurement with Eq. (1.112) conveniently yields the optomechanical coupling rate g, the cavity linewidth κ and the cavity detuning Δ [18]. Our measurement setup described in Section 2.2 is designed to characterize optomechanical systems by measuring their OMIT response.

Chapter 2

Fabrication and Measurement Setups

This chapter presents the setups that we use for the fabrication of fiber mirrors (Chapter 3) and to operate the FFPC (Chapters 4 and 5).

The fiber mirrors were fabricated using a CO_2 laser setup to machine mirror templates on the tip of optical fibers.

The MIM system is operated using a measurement and control setup that we designed and built, which prepares the cavity input field and measures the reflection and transmission signals.

The distances between the two fiber mirrors and the membrane in the MIM system are characterized using a white-light spectroscopy setup which measures the reflection and transmission of the system in a broad wavelength range.

2.1 CO_2 Ablation Setup

CO_2 laser ablation is a well-established technique for the processing of optical glasses, uniquely suited to fabricating micrometer-scale structures with sub-nanometer surface roughness [96, 97]. A wide range of shapes can be produced using this technique, including microspheres [98], microlenses [99, 100], microtoroids [101], gratings [96], holographic structures [102] and concave mirror templates [67, 103]. In this work, we use CO_2 laser ablation to realize concave mirror templates on the tip of optical fibers. Our optimization of the single-shot ablation technique has been published in [68]. We then use these fibers to form tunable open-access Fabry-Perot microcavities [41, 42].

2.1.1 Instruments

Our CO_2 laser ablation setup is depicted in Fig. 2.1(a). Similar to the setup introduced in [104], it comprises both a CO_2 ablation arm and an imaging arm.

At the core of the ablation arm is an RF-pumped Synrad Firestar V30 10.6 µm CO_2 laser, driven by a 20 kHz pulse-width-modulated control signal generated by the dedicated UC-2000 controller, which ensures a nearly continuous output and sets the maximum power that can be used for ablation. Here we use a 50 % duty cycle, which corresponds to a maximum power of 2.1 W. The ablation pulses are shaped by imprinting a square temporal profile on the nearly continuous wave CO_2 laser beam using a Brimrose GEM-40 acousto-optic modulator (AOM), to which we send square pulses of amplitude V_{AOM} between 0 and 1 V and of duration τ ranging from 10 to 50 ms. In order to provide optical isolation, the beam passes through a Brewster polarizer and a quarter-wave plate. This also makes the beam circularly

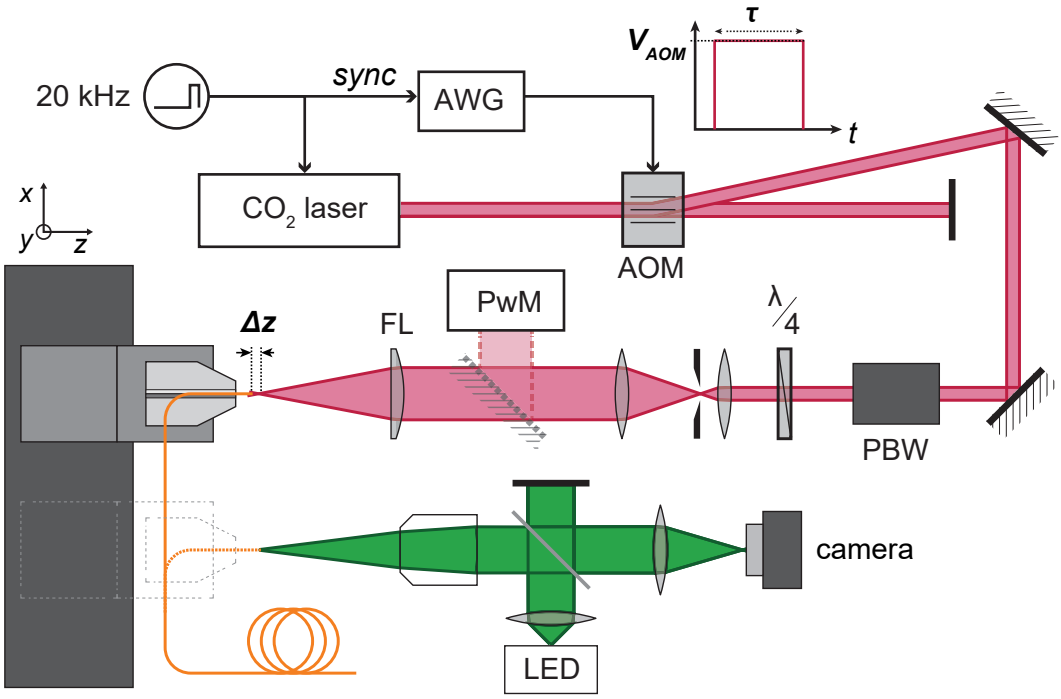

FIGURE 2.1: Drawing of the CO_2 ablation setup. AWG: arbitrary waveform generator, AOM: acousto-optic modulator, PBW: Brewster polarizer, PwM: power meter, FL: aspheric lens, Δz: distance between the focal point of the focusing lens and the ablation target. The inset shows the electronic pulse of amplitude V_{AOM} and duration τ that is sent to the AOM to shape the CO_2 ablation pulse.

polarized, which reduces the ellipticity of ablated structures [105]. The beam is then expanded before being focused by a 50 mm focal length ZnSe aspheric lens. A mirror can be placed before the focusing lens in order to measure the incident power with a power meter, providing a characterization curve between the amplitude V_{AOM} of the pulse sent to the AOM and the power P_{CO2} of the ablation pulse. The radius of the beam at the position of the target is controlled by positioning the target at a distance Δz from the focal point of the lens, ranging from 0 to -1 mm. The mapping between the defocusing distance Δz and the $1/e^2$ beam radius (spot size) w is calibrated by performing a series of knife-edge measurements of the beam profile for different values of Δz.

A combination of a long-range x stage and of a short range xyz stepper motor stage allows the sample to be translated from the ablation arm to the imaging arm, where the tip of the fiber is observed with a microscope. A calibration process allows the exact distance in x, y and z between the focal spot of the microscope and the focal spot of the CO_2 laser to be determined.

2.1.2 Ablation process and parameters

The fabrication of fiber mirrors is done in four major steps. First the fibers are placed in a holder and prepared for ablation. Then the mirror templates are machined in the CO_2 ablation setup. The resulting height profile is measured using a profilometer. Finally, the fibers are sent to an external company that deposits a high reflectivity mirror coating onto the tips of the fibers

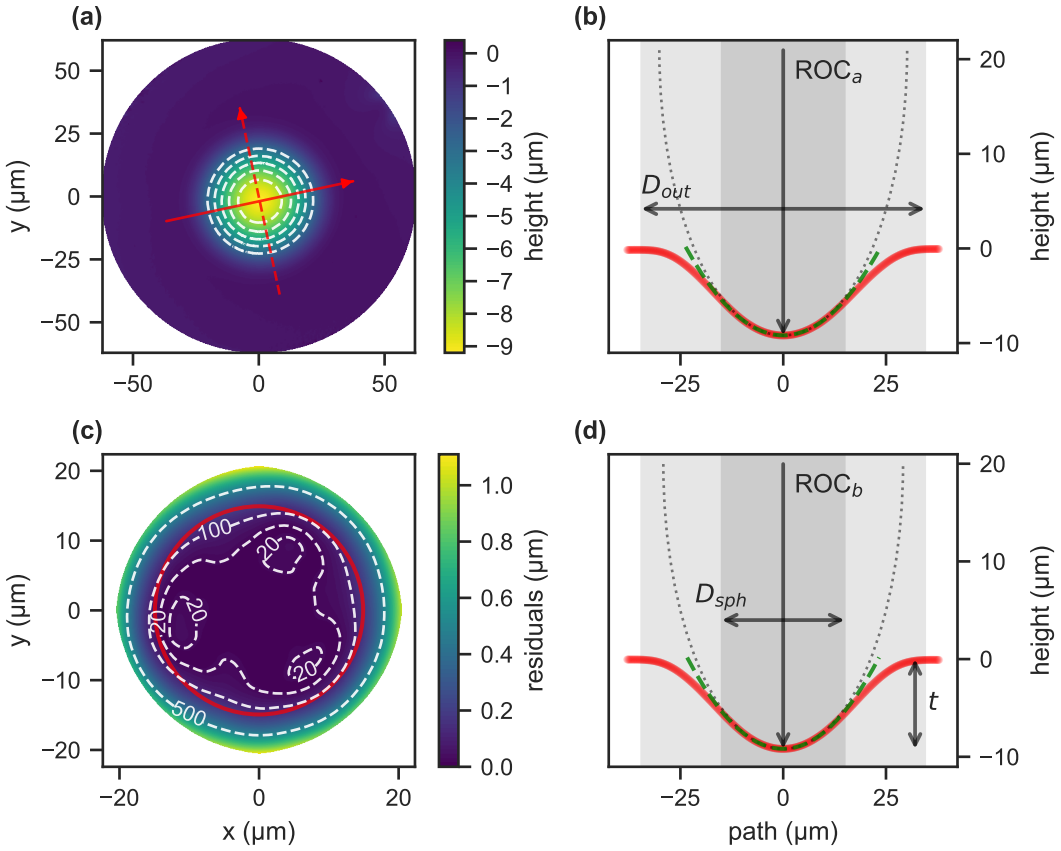

FIGURE 2.2: **(a):** height profile of a fiber as measured by laser scanning confocal microscopy. The white dashed lines are contour lines at -7.6,-6.1,-4.5,-2.9 µm, starting from the center. **(c):** Residuals of the fit of an elliptic paraboloid to the height profile in (a), with white dashed contour lines labeled in nm. The red circle shows the disk of diameter D_{sph} within which we consider the structure to be equivalent to a sphere of radius ROC. **(b,d):** Linecuts through the height profile following the major and minor axes of the fitted elliptic paraboloid (red full and dashed arrows in (a)). The green dashed curves are the corresponding linecut through the best fit elliptic paraboloid. The dotted black curves are the circles of radii ROC$_a$ and ROC$_b$ (note the different lateral and vertical scales).

The first step is to prepare the fibers : each fiber is cut to about 30 cm, its coating is stripped, and it is cleaved using a Photon Kinetics PK11 ultrasonic cleaver. The fiber is then placed into a holder with 2 mm of freestanding length, and the holder is fixed in the CO_2 ablation setup.

The second step is to perform the ablation procedure as follows:

1. center the core of the fiber at the focal point of the imaging arm. The core appears as a bright spot on the microscope image due to the illumination light coupling into it and being reflected from the other end of the fiber.
2. translate the holder by the calibrated distance so that the core of the fiber is located at the focal point of the CO_2 laser beam.
3. tune the spot size at the position of the fiber by performing an additional displacement along the beam axis.
4. trigger the ablation pulse.

5. translate the holder back to the imaging arm to confirm centering and to roughly estimate the geometrical characteristics of the resulting structure.

In the third step, the height profiles of the ablated fibers are measured with a Keyence VK-X200K laser scanning confocal microscope with a vertical resolution of 0.5 nm and a lateral pixel size of 46.5 nm. An example of a typical height profile is shown in Fig. 2.2(a). We performed AFM measurements on a few of the fibers and found that the roughness at the center of the ablated structures is typically smaller than 0.3 nm rms, in good agreement with previously reported values [67].

Finally, for height profiles exhibiting a concave part, we extract its characteristic dimensions as follows. We first correct for plane tilt, find the center of the structure, and calculate its outer diameter D_{out} which we define as the diameter of the contour line at 5 % of the depth of the structure. We then fit an elliptic paraboloid to the height profile cropped to a disk centered on the structure and whose radius is half the waist of a Gaussian fitted to a linecut through the structure. The residuals of such a fit to the data in Fig. 2.2(a) are shown in Fig. 2.2(b). Next, we use the fit results to calculate the depth t of the structure and its radius of curvature $\mathrm{ROC} = (\mathrm{ROC}_a + \mathrm{ROC}_b)/2$, where ROC_a and ROC_b are the radii of curvature along the major and minor axes of the elliptic paraboloid. These dimensions are shown visually in Fig. 2.2(c). Finally, we evaluate the residuals of the fit and calculate the spherical diameter D_{sph} of the structure, which we define as the diameter of the disk centered on the structure for which fit residuals are smaller than 100 nm. D_{sph} is intended to be an estimate of the effective mirror diameter as defined in [41], and is used to estimate clipping losses as per Eq. (1.47).

2.2 Measurement and Control Setup for Operating a MIM System

This section introduces the measurement setup that was designed in order to interface with our object-in-the-middle experimental system.

This setup is responsible for preparing the laser beam before sending it to the MIM system, and for collecting, recording, and processing the beams reflected and transmitted by the optical cavity. It additionally controls the positioners within the experimental system, as well as other experimental parameters. It is intended to perform cavity characterization measurements, PDH cavity stabilization, and optomechanical characterization measurements including OMIT measurements.

The setup is computer-controlled using the QCoDeS module in Python [106].

2.2.1 Instruments

The setup is depicted in Fig. 2.3. The laser beam is prepared in three successive stages during which the signal is generated, phase-modulated, and frequency-shifted before being sent to the cavity via a cross-polarized scheme allowing for the reflected signal to be efficiently collected, and separated from the input field to a high degree.

The signal is generated by a wavelength-tunable external cavity diode laser[1] (915 nm to 985 nm), and coupled into an optical fiber.

The phase modulation is performed using a fiber-coupled electro-optic modulator (EOM)[2], which is placed after a fiber-based polarization controller. The RF signal

[1] Toptica CTL950

[2] iXblue NIR-MPX950-LN-10

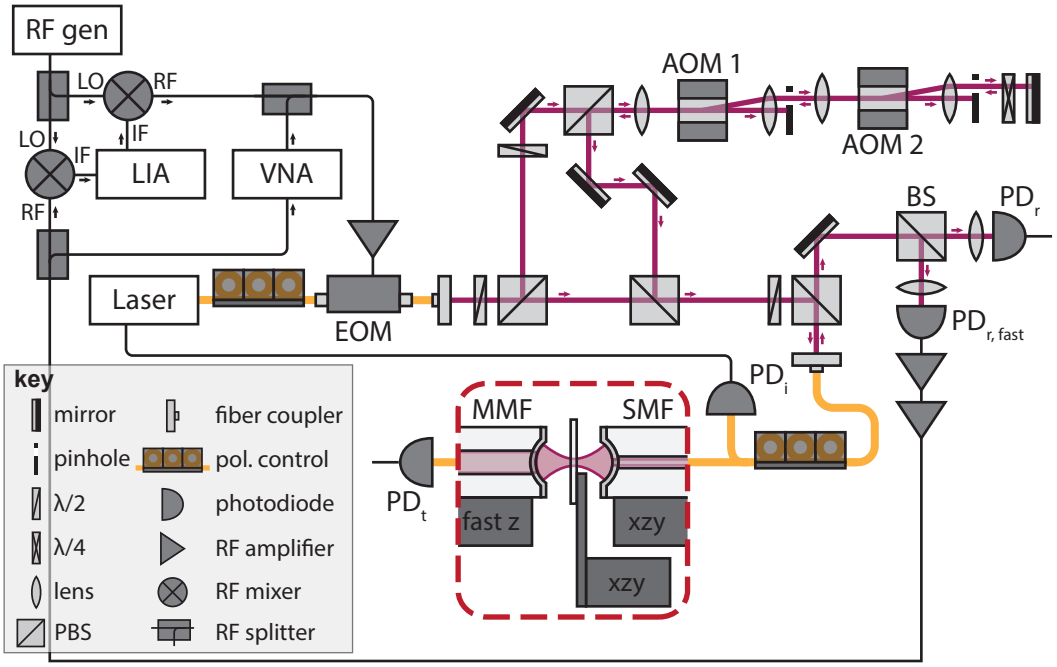

FIGURE 2.3: Drawing of the measurement and control setup. The experimental system shown within the red-dashed area corresponds to the experimental system studied in Chapters 4 and 5. All beamsplitters are polarizing beamsplitters except the one labeled BS which is a 50:50 beamsplitters.

sent to the EOM is the sum of a signal generated by a vector network analyzer[3] (VNA) at angular frequency ω_{VNA} and of a signal generated by a lock-in amplifier[4] (LIA) and up-mixed using an RF source[5], at angular frequency $\omega_{\mathrm{RF}} = \omega_{\mathrm{EOM}} = \omega_{\mathrm{LO}} + \omega_{\mathrm{LIA}}$. It is pre-amplified[6] before entering the EOM.

The next stage is performed in free space. The signal is split with a tunable ratio using a polarized beamsplitter (PBS) in conjunction with an achromatic half-waveplate ($\lambda/2$). One branch goes through two cascaded free-space acousto-optic modulators[7] (AOMs) arranged in a double-pass configuration. The AOMs have a center frequency of 200 MHz and can be tuned within a 45 MHz bandwidth. The two AOMs are oriented so that they shift the frequency of the laser signal in opposite directions. The frequency and the diffraction efficiency of each AOM is controlled via an associated driver module[8]. Overall the signal passing through the AOMs undergoes a tunable frequency shift within ± 90 MHz and a tunable power modulation. The two branches are then recombined. The frequency components of the laser signal after these preparation stages are shown graphically in Fig. 2.4.

The signal is then sent to the experimental system following a polarization-based dark-field technique [107]. The beam is reflected on a polarized beamsplitter before being coupled into an optical fiber, going through a fiber-based polarization controller, and being sent to the experimental system. Once the polarization controller is adjusted, the polarization of the backward-propagating signal reflected from the

[3] Rohde & Schwarz ZNB4
[4] Zurich Instruments HF2LI
[5] Rhode & Schwarz SGS100A
[6] iXblue DR-AN-10-HO
[7] Gooch & Housego 3200-1113
[8] Gooch & Housego 1200AF-AEFO-2.5

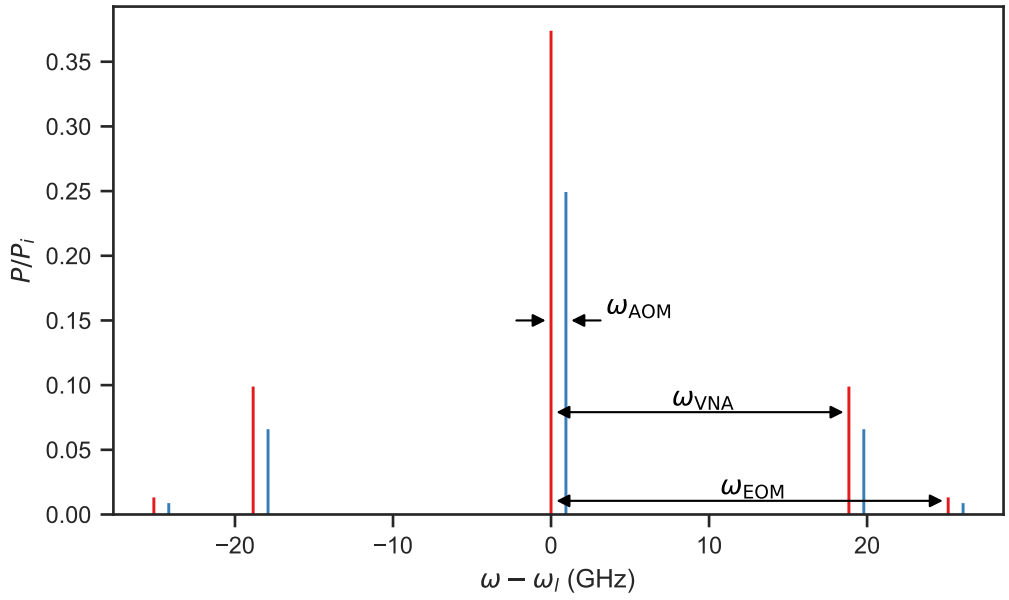

FIGURE 2.4: Frequency components of the laser signal sent to the cavity, referenced to the laser frequency ω_l. Components in blue are generated by splitting the original laser signal and shifting its frequency using the AOMs. Both red and blue components contain a carrier and sidebands generated by an EOM.

cavity and impinging on the polarized beamsplitter is rotated by 90° compared to the forward-propagating input, and is thus transmitted through the beamsplitter. The polarization-based dark-field technique allows for the reflection signal to be efficiently collected, and prevents the reflected signal from being fed back into the laser, which can impact the stability of its output.

The reflection signal is further split in two before being collected on a variable gain photoreceiver[9] and on a fast photodiode[10]. The variable gain photoreceiver detects the slowly-varying part of the signal, while the fast photodiode is AC-coupled and detects the fast-varying part of the signal up to 9 GHz. The output of the fast photodiode is externally amplified in two stages[11], before being split with one part sent to the VNA input and the other part down-mixed and sent to the LIA input. The transmitted signal is detected on a second variable gain photoreceiver[12].

The MIM experimental system studied in Chapters 4 and 5 is depicted within the red-dashed outline in Fig. 2.3. Several positional degrees of freedom of the MIM system are electronically controlled, as described in detail in 4.1.2.

The different instruments in the laser setup are extensively computer-controlled. The laser, RF generator, and VNA are controlled remotely, and the positioners within the experimental system are interfaced via a dedicated control unit[13]. Remotely controlled digital acquisition cards[14] are used to record the signal from the photodiodes and from other devices in the experiment. These cards are also used to send DC inputs to the EOM amplifier, AOM drivers, and positioner control modules. A

[9] FEMTO OE-300
[10] Newport 818-BB-51A
[11] Minicircuits ZX60-123LN-S+ and ZX60-02203+
[12] FEMTO OE-300
[13] Attocube ANC300
[14] NI PXI-6115, PXI-6251 and PXIe-6361

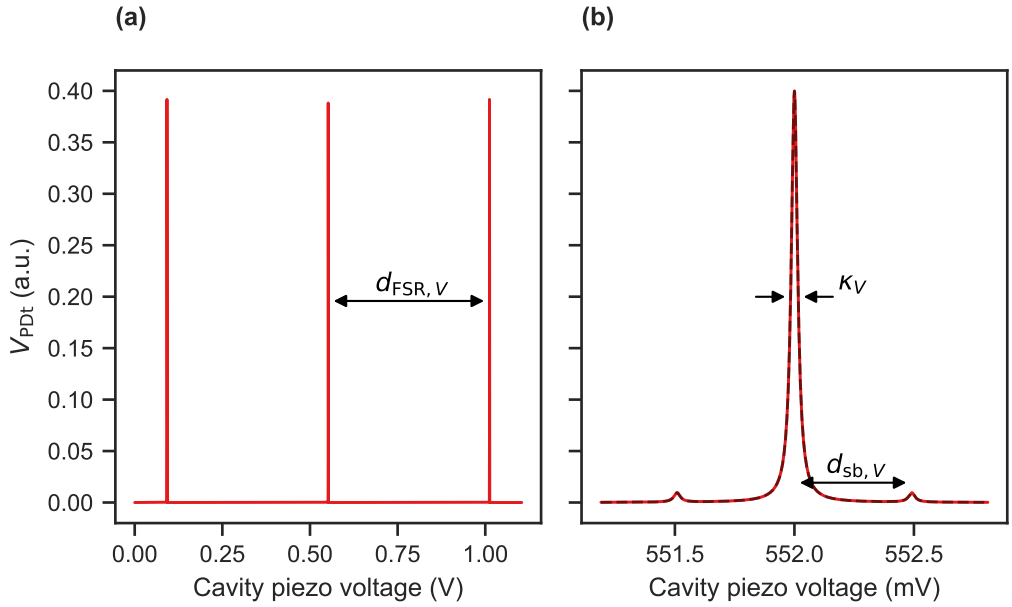

FIGURE 2.5: **(a):** model of the transmitted signal during a cavity scan, in the case of a phase-modulated input field. **(b):** zoom in on a cavity resonance. The annotations illustrate quantities that can be extracted through data analysis.

waveform generator[15] is used to generate voltage ramps for continuously tuning experimental parameters, and can be synchronized with the acquisition cards.

2.2.2 Scanning the cavity

One of the key measurements is to record the reflected and transmitted signals while the detuning between the laser and the cavity is continuously scanned. Due to the short cavity length which is characteristic of FFPCs, the cavity linewidth is very large (GHz), and the free spectral range even more so (10 THz). The best way to scan the detuning between the laser and cavity across a wide range of values (on the order of a few times the cavity linewidth to 3 or 4 times the free spectra range) is to vary the length of the cavity. This range of detuning corresponds to a change in cavity length on the order of 100 pm to 3 µm, which is readily achieved using the DC control of the z cavity positioner. An additional benefit is that such displacements can be performed very rapidly, which reduces the effects of the mechanical instabilities on the measurement.

In order to achieve the desired cavity scan, an S-shaped voltage ramp is generated with the function generator and sent to the DC port of the z cavity positioner. The S-shaped ramp consists in a constant acceleration phase, followed by a constant velocity phase during which the cavity length changes linearly with time, followed by a constant deceleration phase. The reverse ramp is then applied to return the cavity length to its initial value. The constant acceleration and deceleration phases prevent slip-stick motion of a stepper positioner along its guiding rod during the scan, improving the repeatability of the scans.

[15] NI PXI-5421

The theoretically expected transmitted signal during a cavity scan is plotted in Fig. 2.5. The cavity response is modeled using Eq. (1.14), considering a phase-modulated input as defined in Eq. (1.26). The annotations illustrate some of the quantities that can be extracted via the following data analysis procedure. The FSR is first determined in terms of voltage as $d_{\mathrm{FSR},V}$, as well as the higher order mode separation when possible. A subset of the data around a cavity resonance is then fitted with three Lorentzians, yielding the cavity linewidth in terms of voltage κ_V and the separation between the carrier and the phase-modulation sidebands in terms of voltage $d_{\mathrm{sb},V}$.

The known phase-modulation frequency ω_{EOM} is used to obtain the cavity linewidth:

$$\kappa = \kappa_V \frac{\omega_{\mathrm{EOM}}}{d_{\mathrm{sb},V}} \tag{2.1}$$

A separate characterization of the cavity length, discussed in Section 2.3 is then necessary to obtain the cavity finesse as:

$$\mathcal{F} = \frac{\Delta\omega_{\mathrm{FSR}}}{\kappa} = \frac{\pi c}{\kappa L_c} \tag{2.2}$$

This measurement of the cavity finesse is primarily subject to errors in the measurement of the cavity length. The cavity finesse can alternatively be obtained through:

$$\mathcal{F} = \frac{d_{\mathrm{FSR},V}}{\kappa_V} \tag{2.3}$$

This measurement of the cavity finesse is primarily subject to errors due to fluctuations of the cavity length during the cavity scans and due to nonlinearities in the motion of piezoelectric elements. Equations (2.2) and (2.3) are used to determine the finesse of our FFPC in Chapter 4, and the pros and cons of both methods are discussed in Section 4.3.3.

Cavity scans are often repeated while varying other cavity parameters, allowing changes in cavity resonance frequency, linewidth, finesse and higher-order mode separation to be monitored.

2.2.3 PDH error signal generation and locking scheme

The cavity detuning error signal is generated in a modified PDH scheme, inspired by [108, 109]. The PDH phase-modulation sidebands are generated at $\omega_{\mathrm{RF}} = \omega_{\mathrm{LO}} + \omega_{\mathrm{LIA}}$, and the resulting amplitude-modulated cavity reflection signal measured by the fast photodiode is first demodulated to ω_{LIA} before being detected in the lock-in amplifier. This detection scheme improves the signal-to-noise ratio of the cavity detuning error signal, and Eq. (1.32) remains valid.

The detuning error signal generated at the output of the LIA is sent to a RedPitaya FPGA, controlled using the PyRPL Python module [110]. The raw error signal is first digitally filtered before being sent to the PID module which generates the feedback signal. The digital filter is designed in the Infinite Impulse Response (IIR) module in order to prevent the feedback signal from driving system resonances, thus maximizing the bandwidth of the lock.

The feedback signal is finally sent to the fast piezoelectric element controlling the length of the fiber cavity, completing the PDH stabilization scheme. The application and performance of this locking procedure is discussed in Section 4.3.4.

2.2.4 Pump-probe optomechanical measurements

The VNA and the AOMs can be used to generate additional tones in the input to the cavity. These tones can be set-up as pumps and probes to implement various optomechanical experiments, including measuring the optical spring and damping effect, and measuring an OMIT signal as outlined in Section 1.2.3. The AOMs can additionally be used to control the amplitude of the input to the cavity with a bandwidth of a few MHz, opening more experimental possibilities.

2.3 White-light Spectroscopy Setup

This section introduces the setup that we use to characterize the distance between the fiber mirrors and the position of the sample in the MIM system. The broadband spectral response of the cavity is characterized, and the positions of transmission maxima or reflection minima are fit to an analytical model to obtain the cavity length.

2.3.1 Instruments

The white-light setup, depicted schematically in Fig. 2.6, consists in a broadband-white light source[16] that is coupled to the input of the optical cavity through a 2x2 coupler, and a spectrometer[17] which collects either the reflected light through the 50:50 2x2 coupler or the transmitted light. The spectrometer spans the range from 600 nm to 940 nm, with a resolution of 0.36 nm.

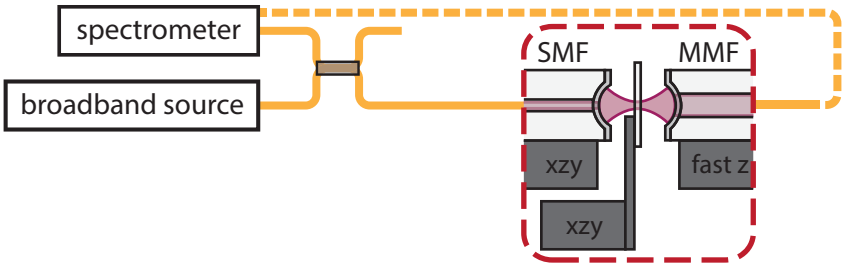

FIGURE 2.6: Drawing of the white-light spectroscopy setup. The broadband light source is coupled into the MIM system via a 50:50 multimode fiber beamsplitter. The reflected signal is collected via the same beamsplitter and sent to the spectrometer. Alternatively, the transmitted signal can be sent directly to the spectrometer.

2.3.2 White-light cavity spectroscopy

In order to improve the robustness of the length measurement, we acquire the transmission or reflection spectrum from the cavity for different cavity lengths and fit the position of the maxima or minima as a function of cavity length. A model dataset, calculated using Eq. (1.14), taking into account the wavelength-dependence of the coating reflectivity and reflection phase, is plotted in Fig. 2.8(b) for cavity lengths between 15 and 20 µm. The power reflectivity and the reflection phase $\phi(\lambda)$ of the distributed-Bragg-reflector (DBR) mirrors used in this work (see Section 3.3.4), modeled using the coupling matrix method introduced in Section 1.1.1, are plotted around the mirror stopband in Fig. 2.7. The white-light setup operates outside of the

[16] Thorlabs SLS201L
[17] Ocean Optics QEPro

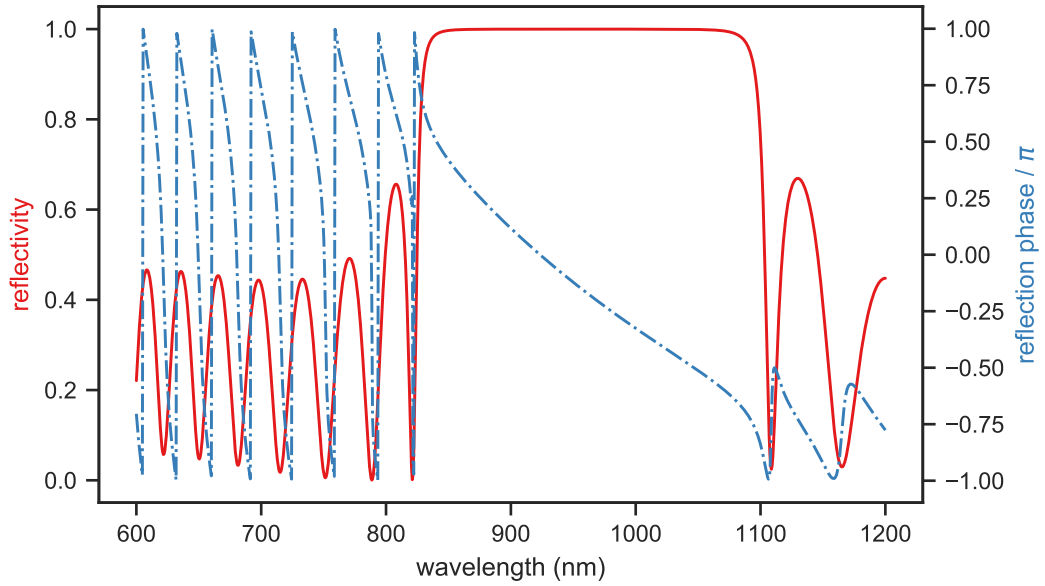

FIGURE 2.7: Power reflectivity and reflection phase of the DBR coating described in Section 3.3.4, modeled using the coupling matrix method introduced in Section 1.1.1.

mirror stopband, where the strong variations in the reflection phase of the DBR lead to strong variations of the penetration depth.

In order to extract the cavity length, the theoretically expected spectrum of the intensity transmission coefficient shown in Fig. 2.8(b) is first normalized by subtracting the average value of the cavity transmission spectrum over all cavity lengths value and normalizing to $[0, 1]$. This preprocessed data, shown in Fig. 2.8(c), facilitates the identification of the transmission maxima, shown as red markers in Fig. 2.8(d).

The positions of the transmission maxima are then fitted in two steps. For each cavity length, an estimate for the cavity length is obtained for all pairs of transmission maxima following :

$$L_c = \frac{\lambda_q \lambda_{q+1}\left(1 + \phi(\lambda_q)/\pi - \phi(\lambda_{q+1})/\pi\right)}{2\left(\lambda_q - \lambda_{q+1}\right)} \tag{2.4}$$

which takes into account the reflection phase [111]. The average of the resulting cavity length estimates for each cavity length are plotted in red in Fig. 2.9, and the standard deviation is shown as green error bars. For each cavity length, using the average of the previously obtained cavity length estimates as an initial value, the following error function is minimized:

$$\sum_q \left| \lambda_q - \frac{2L_c\pi}{q\,\pi - \phi(\lambda_q)} \right| \tag{2.5}$$

using q and L_c as free variables, with q required to be an integer. For each cavity length, the resulting cavity length estimate is plotted in blue in Fig. 2.9, and the statistical error on the fit is shown as orange error bars. Simultaneously fitting the position of several successive maxima significantly decreases the statistical error.

Figure 2.9 confirms that the fitting procedure, applied to modeled data, accurately estimates the cavity length. Applying the fitting procedure to the modeled

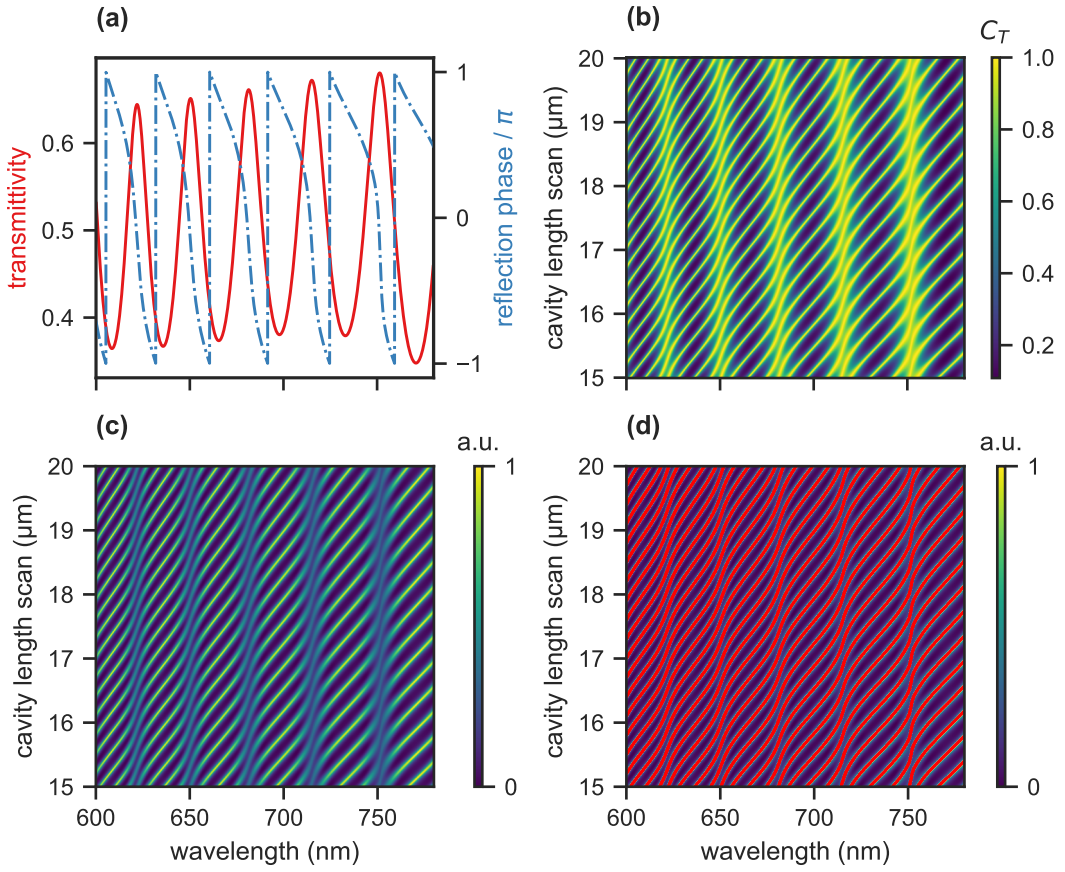

FIGURE 2.8: **(a):** model of the transmittivity and reflection phase of the DBR coating in the wavelength range of interest. **(b):** model of the intensity transmission coefficient for a cavity defined between two mirrors coated with this DBR, calculated using Eq. (1.14) for cavity lengths between 15 and 20 µm. **(c):** normalized data corresponding to the raw data in (b). **(d):** identified transmission maxima are shown as red markers, overlayed on the data from (c).

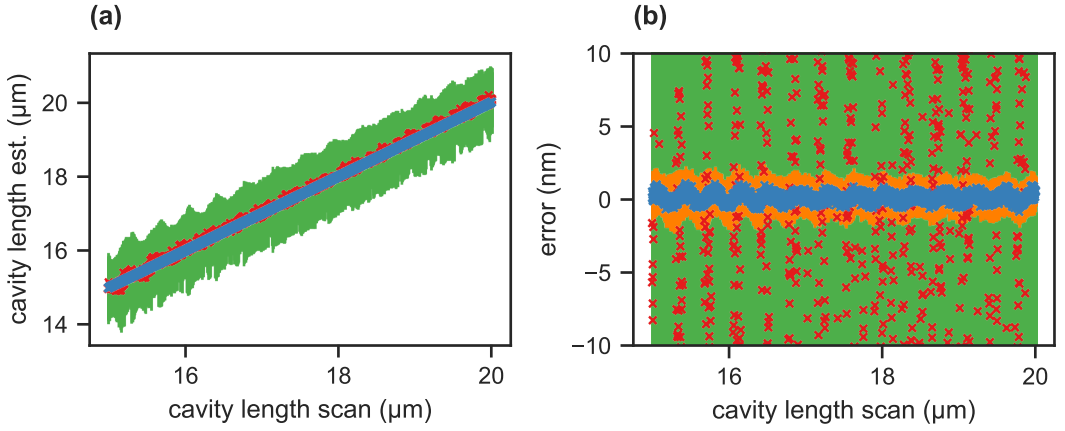

FIGURE 2.9: Graphical output of the different steps of the white-light fitting procedure. **(a,b):** cavity length estimate and corresponding errors as a function of the cavity length used in the model. The red markers show the estimates (resp. errors) from the first fitting step, with green error bars. The blue markers show the estimates (resp. errors) from the second fitting step, with orange error bars.

data results in an uncertainty on the estimate of the cavity length that is smaller than 10 nm. We believe that the uncertainty is a numerical artifact due to the discrete grid of points used for the modeling rather than an intrinsic limit of the method. Even though this method of measuring the cavity length is robust enough to be used (see experimental results in 4.3.3), we are currently working on improving its resolution.

Chapter 3

CO_2 Ablation of Optical Fiber Mirrors for Fabry-Perot Cavities

The optical cavity is the key component of the experimental platform. The fact that the cavity is to be operated within a ^{4}He cryostat places special constraints on the size of the mirrors and on the coupling of the laser light into the system. These constraints have lead us to chose to work with a Fiber-based Fabry Perot Cavity (FFPC), where the optical fibers are used both as cavity mirrors and as a way to couple light in and out of the cavity. This type of optical cavity satisfies our experimental constraints due to its very small spatial footprint. Additionally, FFPCs interface conveniently with the laser system outside the cryostat and offer excellent optical properties, notably spectral tunability, high finesse and a small mode volume [41]. The fiber mirrors used in this work have been shaped in-house using the CO_2 ablation setup presented in Section 2.1 and then sent to an external company (LaserOptik) for the coating to be deposited.

CO_2 laser ablation is a complex, multi-physical process in which the dynamics of heat transfer, phase transitions and liquid flow all come into play. The dominant phenomena for determining the shape created at the ablation site are strongly material dependent and change even for small variations in ablation parameters [112]. For instance, when the surface temperature is not raised above the vaporization temperature, material removal is minimal and the ablation site mainly undergoes smoothing [113]. When vaporization occurs, for certain ablation parameters a combination of vaporization and of melt displacement driven by recoil pressure can result in the formation of a concave shape [114]. Finally, if solidification occurs slowly enough, capillary forces can make the geometry evolve further, eventually leading to a convex shape [115]. Mainly due to a lack of quantitative understanding of the interplay between those phenomena during the ablation process and to a lack of data on material properties at high temperature, models have yet to demonstrate the ability to accurately predict the shape resulting from CO_2 laser ablation within an experimentally relevant range of ablation parameters [112, 115–117]. Modeling is especially problematic for optical fibers since radial boundary effects come into play [67]. This motivated us to study in detail the specific effect of each ablation parameter, aiming to guide our choice of ablation parameters for the fabrication of our mirrored fibers.

The main focus over the past few years has been developing multi-shot ablation procedures in order to improve control over the geometry of the concave shape [104, 118–120]. Multi-shot ablation procedures make it possible to realize mirror templates with a large radius of curvature and a large useful diameter, leading to significant progress in experiments that benefit from low loss millimeter-sized optical cavities, such as trapped ion CQED [55], trapped atom CQED [54], solid-state

QED [53], and optomechanics [59]. On the other hand, single-shot ablation procedures are well suited to realizing mirror templates with a small radius of curvature [43, 121], which benefit to experiments requiring optical cavities with a small mode volume [122, 123].

Our experiment falling into this last category, we decided to use single-shot ablation. This chapter describes how we optimized the CO_2 ablation process in a first fabrication run, and how we applied this knowledge to produce fiber mirrors for use in our experimental system in a second fabrication run.

3.1 Effects of Ablation Parameters on Structure Shape

Few systematic studies of the effects of fabrication parameters on the geometry of structures created on the tip of an optical fiber by a single ablation pulse have been performed since the pioneering work from [67] has been published. In order to try and optimize mirror templates obtained with a single shot ablation procedure, we fabricated a first batch of fibers in order to optimize the CO_2 ablation process. For this batch, we used a broad range of pulse powers, pulse durations, and spot sizes, and characterized in detail the influence of each of those three ablation parameters on the shape of the resulting structures, and more specifically on their radius of curvature, depth, and diameter. We machined 129 mirror templates onto the end-facets of Thorlabs 780HP single mode optical fibers, whose core and cladding diameters are 4.4 and 125 µm respectively. The ablation procedure was performed as described in Section 2.1.2, with no calibration, pre-smoothing or post-smoothing shots. We used pulse durations τ of 10, 30, and 50 ms and defocusing distances Δz of 0, -0.1, -0.2, -0.3, and -0.4 mm, corresponding to spot sizes w of 32, 36, 45, 56, and 67 µm. For each combination of those parameters, we performed a series of ablations with varying pulse power P_{CO2}. We then measured the height profile of the fiber facets, which can be flat, concave, convex or a mixture of convex and concave. For the 123 fibers that were concave in their centers, we fit this concave part to extract the geometrical characteristics of the structure.

In order to illustrate the effect of ablation pulse power on the shape, linecuts through the height profiles of a selection of fibers are plotted in Fig. 3.1(a). We distinguish phenomenologically 5 different regimes of pulse power, each of them leading to a different type of modification of the surface of the fiber, some of which might not be observed depending on the value of the other ablation parameters. 1) For very low pulse powers, no modification of the surface occurs. 2) For low pulse powers, the overall geometry is not modified, but the area exposed to the laser is smoothed. 3) For medium pulse powers, concave structures are created, whose depth and outer diameter increase with pulse power. 4) For high pulse powers, concave structures whose depth and outer diameter decrease with pulse power are created within an increasingly convex shape. Such a shape effectively reduces the lateral dimensions of the fiber mirror, thus preventing cleaving imperfections from limiting the minimum length of optical cavities, which usually requires additional processing steps [124]. 5) For very high pulse power, a fully convex shape is created. The change from a concave to convex-concave geometry associated with the transition from regime 3 to 4 is highlighted in Fig. 3.1(b), where we plot the curvature of a convex parabola fitted to the outer part of the fibers whose linecuts are shown in Fig. 3.1(a). We now focus on the concave structures that are obtained in regimes 3 and 4, and discuss the effects of pulse power, pulse duration, and spot size on their geometry.

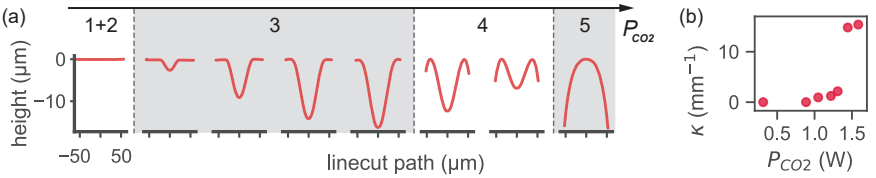

FIGURE 3.1: **(a):** Linecuts taken through the measured height profiles of fibers ablated with increasing pulse power. The axis shows the direction along which P_{CO2} increases and illustrates the power regimes defined in the main text. The values of P_{CO2} used were 0.3, 0.9, 1.0, 1.2, 1.3, 1.4, 1.6 and 0.5 W for fibers from left to right. A spot size of 45 µm was used for all fibers. A pulse duration of 30 ms was used for all fibers but the rightmost, which was subjected to a 300 ms ablation pulse. **(b):** Plot as a function of P_{CO2} of the curvature κ of a convex parabola fitted to the outer part of the fibers whose linecuts are shown in (a) and for which a pulse duration of 30 ms was used.

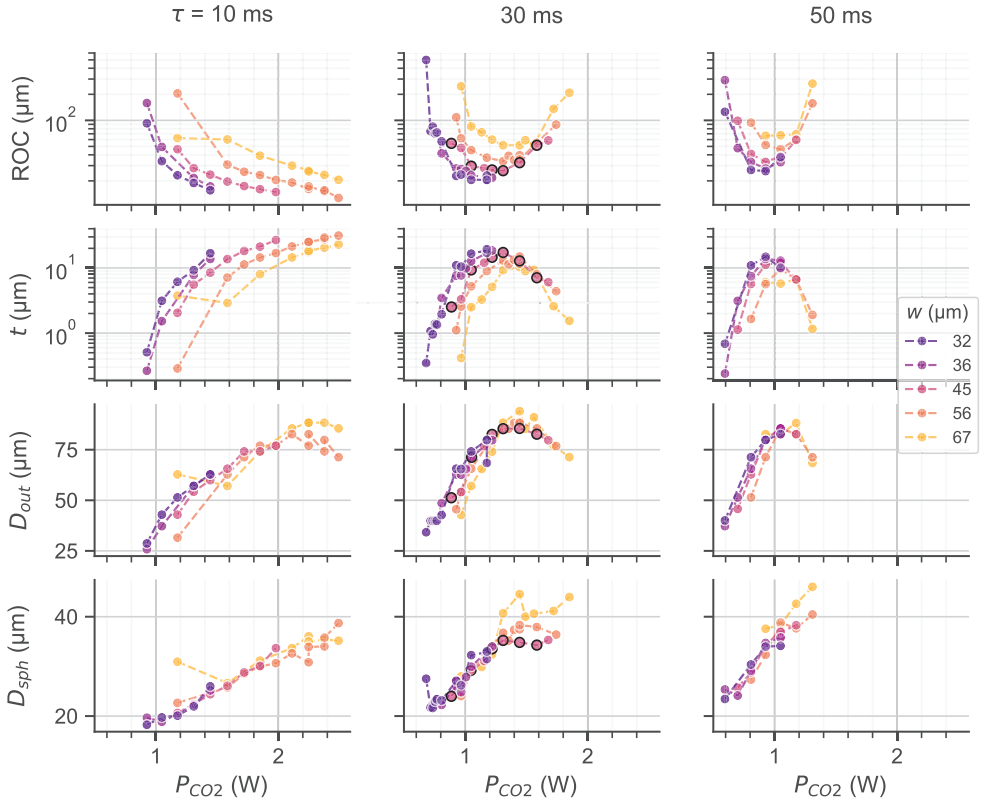

FIGURE 3.2: Geometrical characteristics of ablated concave structures plotted as a function of ablation parameters. The different rows show plots of ROC, t, D_{out}, and D_{sph} as a function of the pulse power P_{CO2}. The pulse duration τ is varied across columns, and the spot size w is encoded in the color of the points. Points corresponding to the fibers belonging to regime 3 and 4 which are shown in Fig. 3.1(a) are outlined in black.

The geometrical characteristics ROC, t, D_{out}, and D_{sph}, obtained by fitting the profiles of the fibers exhibiting concave structures following the procedure outlined in 2.1.2, are plotted in Fig. 3.2 as a function of the ablation parameters P_{CO2}, τ, and w. In the low power regime (regime 3), an increase in pulse power leads to a decrease in ROC, and an increase in depth, outer diameter and spherical diameter. In the high power regime (regime 4), an increase in pulse power leads to an increase in ROC, a decrease in depth and outer diameter, and an increase in spherical diameter. In both power regimes, an increase in spot size leads to an increase in ROC, a decrease in depth and has no significant effect on the outer and spherical diameter. Increasing the pulse duration has a more complex effect: it generally shifts values of the geometrical characteristics to lower pulse powers and narrows their distribution. This results in a decrease in the pulse power corresponding to the onset of regime 4, associated with an increase in the sensitivity of the geometry to changes in the pulse power. As a consequence, shorter pulse durations give a finer control over the geometry of the structures since deviations in pulse power have a smaller effect. In addition, decreasing the pulse duration decreases the minimum achievable ROC, increases the maximum achievable depth, and decreases the minimum achievable outer and spherical diameter. Note that we do not observe the defocusing distance to have a significant effect on crater asymmetry, which we measure to be 5 % on average.

3.2 Relationships Between the Geometrical Characteristics of Concave Structures

We then studied the relationships between ROC, t, and D_{sph}, and identified regimes of ablation parameters that lead to templates with favorable geometries for use in CQED and optomechanics.

Fiber-based Fabry-Perot optical microcavities are widely used in the fields of CQED [45–52, 54, 55] and optomechanics [20, 21, 56–60], with additional applications in sensing [125–127]. For most of these applications, it is desirable to minimize the waist w_0 of the cavity mode and to maximize its finesse $\mathcal{F}$. To achieve this, it is necessary to optimize several geometrical characteristics simultaneously while complying with experimental requirements specific to each application. We have studied the relationships between the geometrical characteristics of the concave structures, showing that they can be independently chosen to a larger extent than previously reported [43, 121] by varying τ, w, and P_{CO2}. We then developed strategies to fabricate mirror templates tailored for two commonly used cavity geometries and their associated applications.

The relationship between the radius of curvature and the depth of the structures is shown in Fig. 3.3 (top). It is most relevant to fiber-based cavity QED with solid-state emitters, or to other applications where an optical emitter is located on or near one of the mirrors. The optimal cavity geometry is the planar-concave geometry, for which the waist of the fundamental mode is given by: $w_0^2 = \lambda L_{cav}/\pi\sqrt{1/\varepsilon - 1}$, with $\varepsilon = L_{cav}/\mathrm{ROC} \in [0, 1]$. ROC is the radius of curvature of the concave mirror and L_{cav} is the cavity length. It is usually desirable to minimize both the cavity length and the radius of curvature in order to decrease the mode waist, the physical limit for L_{cav} being the depth of the structure. One should additionally make sure that $L_{cav} < \mathrm{ROC}/2$ in order to prevent finesse deterioration due to diffraction losses [75]. A rough guideline for the best cavity geometry is then $L_{cav} = t = \mathrm{ROC}/2$ (shown as a gray dashed line in Fig. 3.3 (top)), with ROC and t as small as possible.

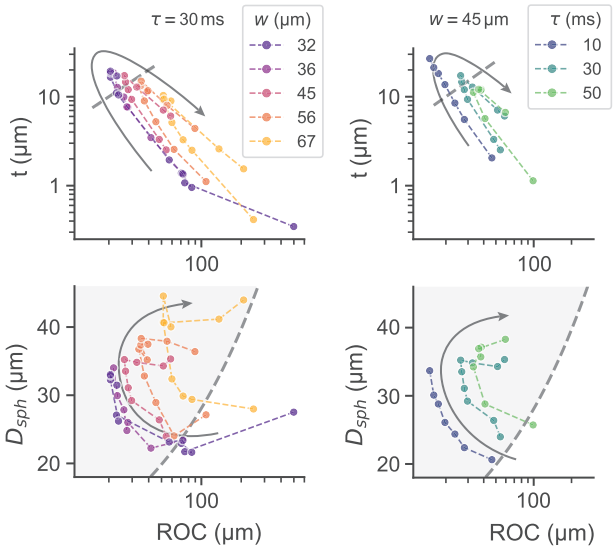

FIGURE 3.3: Plots of the relationships between geometrical characteristics, with the direction of increasing pulse power shown by the gray arrows. **(top):** Structure depth as a function of radius of curvature for various spot sizes and pulse durations respectively. The dashed line follows $t = \mathrm{ROC}/2$. **(bottom):** Spherical diameter as a function of radius of curvature for various spot sizes and pulse durations respectively. The shaded area shows the region where clipping losses are small in the case when $\varepsilon = 1$.

The ablation results plotted in Fig. 3.3 (top) show a strong nonlinear relationship between the radius of curvature and the depth of structures ablated with varying pulse power at constant spot size and pulse duration. However, we observe that this relationship depends strongly on the values of spot size and pulse duration. Structures with favorable geometries can be produced using short pulse durations, small spot sizes and high pulse powers within regime 3. Smaller spot sizes can be achieved both by decreasing Δz and by using a focusing lens with a larger numerical aperture.

In contrast, another category of applications exists for which experimental constraints limit how short the cavity can be made. Fiber-based cavity QED with trapped atoms or ions, fiber-based cavity optomechanics, or other applications where the emitter or mechanical resonator is located in between the two mirrors belong to this category. The preferred cavity geometry is then the symmetric geometry. For these relatively long cavities, one of the the main difficulties is to maintain a high finesse. Finesse is degraded by clipping losses, which arise when the spot size of the fundamental mode of the cavity on the end mirrors becomes large compared to the spherical diameter. The condition on D_{sph} for clipping losses not to significantly degrade the finesse of a symmetric cavity is given by [41]: $D_{\mathrm{sph}}^2 \geq \ln(5\mathcal{F}/\pi)\lambda L_{\mathrm{cav}}/(\pi\sqrt{\varepsilon\,(2-\varepsilon)})$, with $\varepsilon \in [0, 2]$. In order to minimize waist while maintaining a high finesse, one should choose structures with the smallest radius possible which satisfy both the above condition and $\mathrm{ROC} > L_{\mathrm{cav}}$. The relationship between the spherical diameter and the radius of curvature of the structures is plotted in Fig. 3.3(bottom), with the small clipping losses region shown for $L_{\mathrm{cav}} = \mathrm{ROC}$. Craters fabricated with a high pulse power within regime 4 exhibit the largest spherical diameters, while pulse duration or spot size can be changed to adjust the radius of curvature.

3.3 Fabricating Fibers for the Qubit Optomechanics Experiments

Leveraging these observations, we planned a second batch of fibers, for use in our experiment. Since we did not have practical experience of using the fibers at that point, we decided to fabricate templates spanning a wide range of crater geometries we thought could work for us. We mainly played around the trade-off between mode volume and cavity length, with craters with short ROC (around 30 µm) leading to small cavities with low mode volume but where it might be difficult to insert a sample, and large ROC (around 100 µm) leading to cavities with larger mode volume but where a sample can be inserted relatively comfortably.

For this fabrication run, we made several changes to our procedure. We designed custom holders so that fibers can be handled in groups of 10 for each step of the process. We also came up with a technique to improve the concentricity of the crater with the core of the fiber. Finally, we experimented with using some pre-processing and post-processing smoothing laser pulses. These smoothing pulses are performed with a large spot size and a low power, aiming to melt and re-solidify a thin layer of the surface of the whole fiber without changing the its existing shape. The pre-processing smoothing pulses are meant to remove any surface roughness left by the cleaving process. The post-processing smoothing pulses are meant to remove any irregularities left by the ablation process (ripples, ejections ...).

Since the fibers in this batch are destined for use in our experimental system, we also had to fulfill additional requirements. Each fibers had to be threaded through a ceramic ferrule, by which it is held in the experimental setup. The fibers need to be sent to an external company, LaserOptik, for the mirror coating to be deposited. They have to fit in their system and withstand the coating process.

This section describes in details the processing of the optical fibers for use as fiber mirrors in our fiber-based optical cavity.

3.3.1 Preparing the fibers, custom holders

For use in our system, we chose to make mirror templates on both single mode and multimode optical fibers. The fibers needed to be compatible with the wavelength of our laser, which can be tuned between 915 nm and 985 nm. Additionally, LaserOptik requested the coating of the fibers not to be the usual acrylate. We picked the Cu800 single-mode fiber (SMF) and the Cu50/125 multi-mode fiber (MMF) from IVGfiber, which both have a cladding diameter of 125 µm. The properties of these two fibers as specified by the manufacturer are listed in Table 3.1. The fibers are coated with 20 µm of copper, over a thin sticking layer of carbon. One added advantage of the copper coating is that it decreases the short and long-term bending radii, which is very useful to fit the cavity in the small space of our cryostat. We use 30 cm pieces of these fibers, which are manageable during fabrication, and can be spliced to the input and output fibers inside the cryostat.

In order to facilitate the handling of the fiber and make the entire procedure more efficient, we designed holding plates that can house 10 fibers. The holding plates can be stacked in a pack of 7, which can be attached directly to the ion-beam sputtering system used by LaserOptik to deposit the mirror coating. Each plate of 10 fibers is prepared for CO_2 ablation by:

1. stripping the copper coating on 52 mm by dipping the fibers for 10 minutes in a ferric chloride based copper etchant from Sigma-Aldrich,

	Cu800	Cu50/125
fiber type	SMF	MMF
wavelength range	800 to 1000 nm	600 to 2000 nm
numerical aperture	0.13	0.22
mode field diameter	6.0 ± 0.5 µm	–
core diameter	–	50 µm
cladding diameter	125 ± 1 µm	125 ± 1 µm
coating diameter	165 ± 10 µm	165 ± 10 µm
core-clad concentricity	< 0.5 µm	< 5 µm
short-term bending radius	> 10 mm	> 10 mm
long-term bending radius	> 25 mm	> 25 mm

TABLE 3.1: Properties of copper-coated fibers from IVG fibers used for this work.

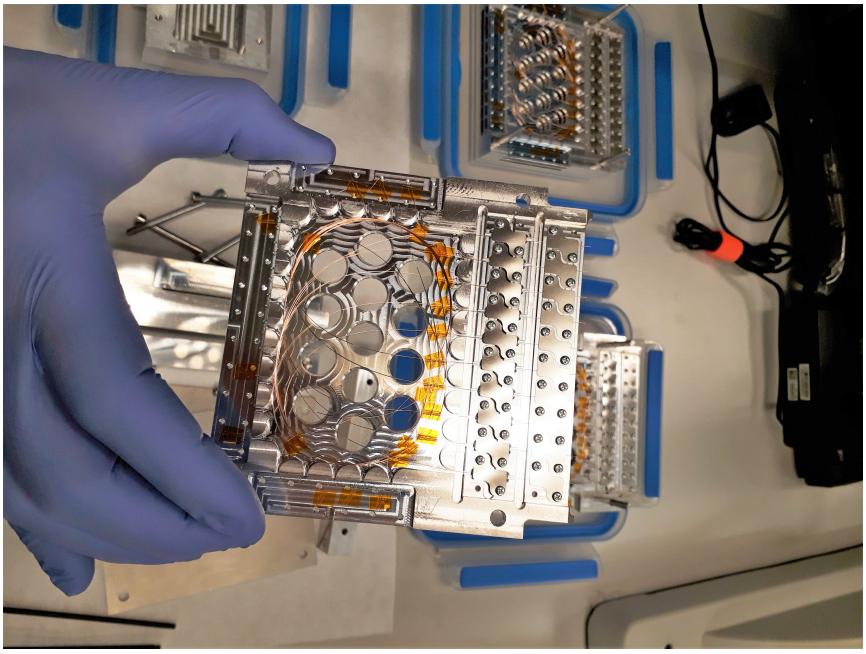

FIGURE 3.4: Picture of a custom handling plate filled with copper coated fibers.

2. rinsing with water, then with IPA, and blow drying,
3. burning the carbon layer using a lighter, then cleaning with IPA,
4. inserting the fibers in a Thorlabs CF126 ferrule (diameter 2.5 mm, length 10.5 mm, bore size 126 µm),
5. cleaving the fibers using a Photon Kinetics PK11 ultrasonic cleaver, shortening the fiber by 20 mm,
6. positioning in a holding plate with the facet 2 mm from the edge,
7. clamping the fibers and ferrules to the plate with springs,
8. coiling the rest of the fiber within the holding plate, securing with tape.

The final result is pictured in Fig. 3.4.

It takes about 3 hours for a trained person to perform these steps and prepare a plate of 10 fibers. Each plate is numbered so that each fiber can be tracked by its plate number and position on the plate. The plates are stacked in plastic boxes which protects them from dust and shocks during storage or transport within the building. The fibers are then ready to undergo the CO_2 ablation procedure.

3.3.2 CO_2 ablation setup and procedure

The fibers are then machined using the CO_2 ablation setup described in Section 2.1. The procedure was slightly modified compared to the one used for the previous batch of fibers in order to adapt to the new holding plates and to improve the accuracy of the crater positioning:

1. attach the holding plate to the positioning stages,
2. position the core of the fiber at the focal point of the imaging arm,
3. translate the holder by a calibrated distance so that the core of the fiber is located at the focal point of the CO_2 laser beam,
4. offset the fiber by about 25 µm,
5. shoot a small calibration crater,
6. return to the imaging arm focus and measure the offset from the expected crater position,
7. return to the CO_2 laser focus, using the corrected calibrated distance,
8. (optional) perform a smoothing shoot sequence,
9. send the crater forming shot with desired parameters,
10. (optional) perform a smoothing shoot sequence,
11. image the resulting crater.

The concentricity of the crater with the fiber core was originally limited by precision issues in the positioning stages. By shooting a calibration crater away from the fiber core, we can make fine corrections to the positioning calibration for each fiber and achieve a centering error ε_c of 1.3 ± 0.6 µm on average.

This procedure is repeated for all 10 fibers in the holding plate. The time needed to machine a full plate of fibers is about 15 minutes.

It should be noted that the multimode fibers behave somewhat differently than single mode fibers when subjected to CO_2 laser ablation, especially when exposed to smoothing pulses. We had to make small changes to our ablation parameters when targeting MMF in order to adapt to this different behavior.

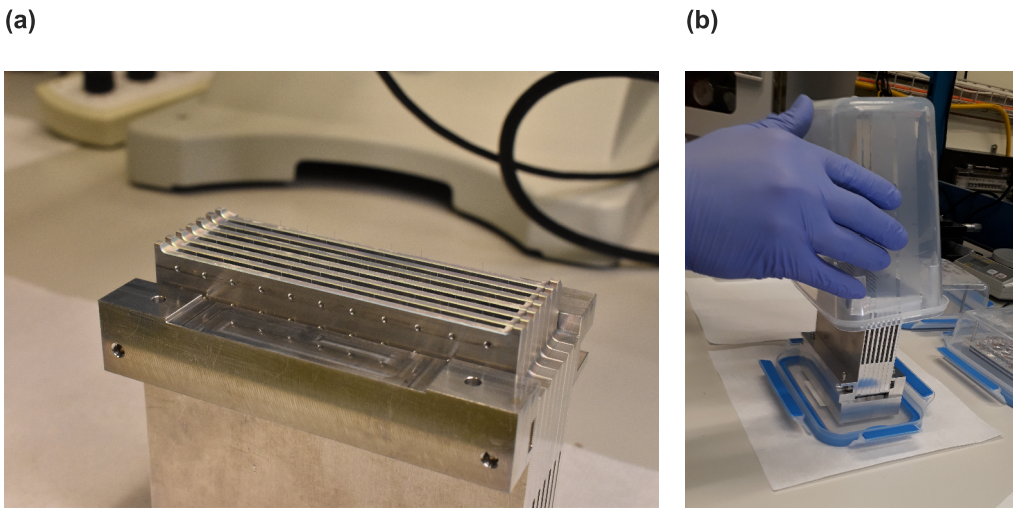

FIGURE 3.5: **(a)** stack of 7 fiber handling plates, **(b)** its shipping box

3.3.3 Profilometry and fitting the profiles

The next step is to measure the height profile of the machined fiber using a Keyence VK-X200K laser scanning confocal microscope, as described in Section 2.1. This is carried out on a stack of 7 handling plates (Fig. 3.5(a)). For each of the 70 fibers in the stack, we navigate to the fiber, perform a focus calibration and run the profiling procedure. The pre-processing of the data is carried out manually within the Keyence software. The data is then exported for further fitting in Python. The time needed to perform the profilometry step is about 4 hours for a stack of handling plates containing 70 fibers.

3.3.4 Shipping for external low loss coating deposition

Up to 4 stacks of 7 handling plates are then each fixed in a customized box using 4 screws (Fig. 3.5(b)), and shipped to LaserOptik.At LaserOptik, the stacks are removed from their shipping box and attached directly to 4 slots in a custom fixture plate that is then inserted in their IBS system. Additional mirror blanks were also attached to the fixture plate and underwent the same coating run. After the coating had been deposited, the stacks were fixed in their shipping boxes again and returned to us.

We chose the coating B-05213-01 for this deposition run. It is nearly a quarter wave stack, consisting of Nb_2O_5 and SiO_2. The first 2 layers (towards the substrate) are adjusted to achieve a residual transmittance of about 100 ppm. The last layer (on top) is SiO_2, to achieve a phase shift which leads to the standing wave field anti-node being about 30 nm above the mirror. The layer sequence is: substrate | 1.82473H 0.59165L (H L)^{12} H 0.93331L, with layer thicknesses given in units of quarter wave optical thickness, reference wavelength 944.6 nm, H: Nb_2O_5 ($n_{950\,\mathrm{nm}} = 2.242$), L: SiO_2 ($n_{950\,\mathrm{nm}} = 1.482$). The extinction coefficient for both materials is in the range of 1×10^{-6}. Overall the coating consists of 28 layers, with a total coating thickness of 3716 nm. The transmission spectrum of the coating as measured by LaserOptik is shown in Fig. 3.6. With this coating, we aimed at achieving a finesse in the range of 15000 in a wide stopband. As will be detailed later, a disadvantage of the wide

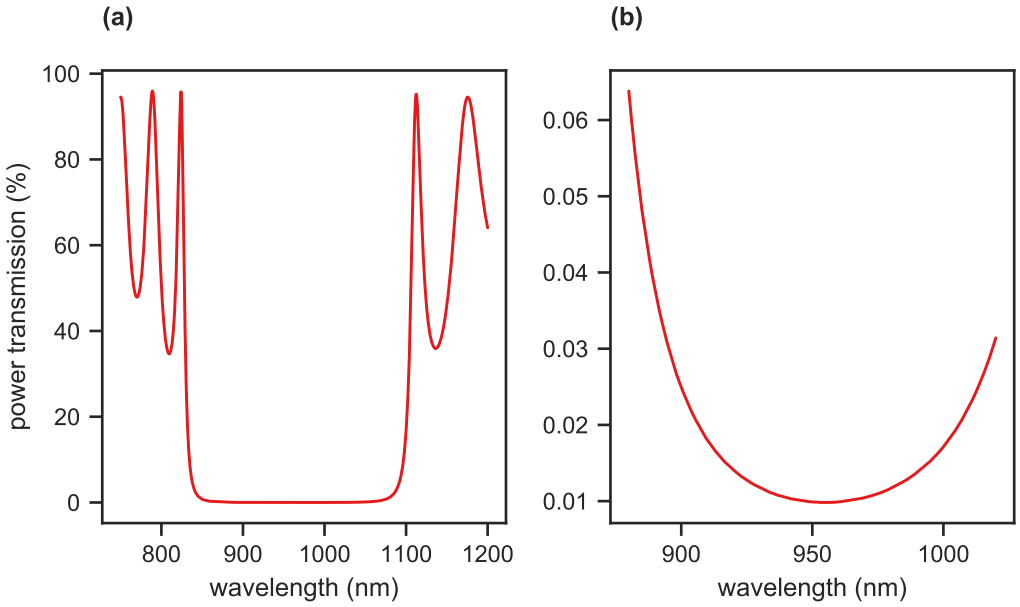

FIGURE 3.6: Transmission of the coating as measured by LaserOptik after the coating run. **(a):** wide range **(b):** zoom in on the stopband

stopband is than it prevents us from tuning the finesse of the cavity by operating at the edge of the coating.

In total 80 SMF, 60 MMF, and several mirror blanks were coated by LaserOptik.

3.3.5 Preparing the fibers for making cavities

After receiving the fibers from LaserOptik, we disassemble the stacks and place the handling plates in storage boxes. In order to make fibers ready for insertion in our setup, we:

1. remove the securing tape with acetone and uncoil fibers,
2. remove the clamping springs,
3. transfer the fibers to a different handling plate,
4. pull the fiber through the ferrule so that the mirror template sits at the desired distance from the front of the ferrule,
5. glue the fiber to the ferrule using Araldite,
6. use TorrSeal to make a strain relief at the back of the ferrule.

One issue we encountered during this process is that some particles of coating got stuck to the cladding of the optical fibers. This prevented the fibers from being pulled in as close to the ferrule end as we wanted to. In a future coating run, this could be prevented by using a larger ferrule or by shielding the side of the fiber from the sputtering beam better.

3.3.6 Summary

Because we have used this batch for experimenting with smoothing, some fibers cannot be used as mirror templates. Within the single-mode fibers, 52 are suitable for use in our experiments : 16 flat, 8 with ROC under 25 µm, 16 with ROC between

fiber	type	R_c (µm)	$R_{c,a/b}$ (µm)	t (µm)	D_{sph} (µm)	D_{out} (µm)	ε_c (µm)
181	Cu800	28.5	28.5/28.5	1.30	14.0	26.7	2.11
182	Cu800	28.4	28.5/28.3	1.27	13.5	26.7	0.42
196	Cu800	69.0	71.1/67.0	0.35	14.7	17.6	0.79
197	Cu800	92.2	93.6/90.8	0.23	14.5	20.6	0.88
315	Cu800	39.0	41.1/37.0	0.47	11.9	17.6	0.39
216	Cu50/125	56.7	59.6/53.9	1.12	19.3	32.7	1.14
262	Cu50/125	126.5	137.7/115.3	0.86	26.4	35.7	0.99
263	Cu50/125	68.3	68.9/67.6	0.94	19.1	32.7	1.17
266	Cu50/125	71.6	73.6/69.7	0.33	14.8	17.6	1.16

TABLE 3.2: Geometrical characteristics of the mirrored fibers used in this work.

25 µm and 55 µm, 7 with ROC between 55 µm and 130 µm and 5 with ROC between 130 µm and 500 µm. Within the multi-mode fibers, 38 are suitable for use in our experiments: 10 with ROC under 25 µm, 16 with ROC between 25 µm and 55 µm, 11 with ROC between 55 µm and 130 µm and 1 with ROC between 130 µm and 500 µm. Fibers with ROC under 25 µm yield very short cavities and are best used in a planar-concave configuration. Fibers with ROC between 25 µm and 55 µm can be used in a concave-concave configuration but require significant precautions if a sample is to be inserted between them. Fibers with ROC between 55 µm and 130 µm can be used rather comfortably in a concave-concave configuration with an object in the middle of the cavity. Fibers with ROC larger than 130 µm can be used very comfortably in a concave-concave configuration with an object in the middle of the cavity, but the cavity will have weaker interactions with this object due to the larger mode volume.

The characteristics of the fibers used in experiments described in this thesis are given in Table 3.2 for later reference.

Chapter 4

Building and Characterizing the Experimental Platform

We call experimental platform the ensemble of elements required to implement and operate our membrane-in-the-middle optomechanical system in high vacuum and at cryogenic temperature. The experimental platform is pictured in Fig. 4.1 and consists of a ^{4}He bath cryostat inside which is placed a high-vacuum insert at the end of which is attached a mechanical housing (probe) containing the MIM system. In this chapter we describe the process of designing, assembling and testing this experimental platform. Part of those results have been published in [69].

4.1 Designing the Experimental Platform

The design for the experimental platform is based on existing low-temperature probes used in the lab [128], with modifications to fit an optical cavity. Some key requirements for the experimental platform were that it should provide optical fiber access to the optical cavity, allow for electronic signals to be sent and collected, have a high level of mechanical stability and vibration isolation, and introduce minimal misalignements in the experimental system when cooling down to 4 K. In this section we will first discuss the ^{4}He cryostat and its insert (Fig. 4.1(a)) and then the design of the probe (Fig. 4.1(b,c)).

4.1.1 Cryogenic system

The experimental platform is based on a superconducting magnet system hosted in a LN_2-shielded ^{4}He bucket cryostat from Cryomagnetics. The system allows for monitoring of the levels of both He and LN_2, and can remain cold for more than a week before He needs to be refilled. The magnet provides up to 8 T of central field at 4.2 K and is controlled using the Model 4G-100 Power System. The cryostat is placed on top of a passive vibration isolation platform[1] with a cutoff frequency of a few Hz, which provides shielding against seismic noise.

A custom high-vacuum insert is used to position a vacuum can containing the probe in the 12.7 cm-diameter, 25 cm-long bore of the superconducting magnet. The head of the insert can be screwed to the top of the cryostat and provides interfaces for connecting a turbo pump[2], a vacuum gauge[3], BNC cables and optical fibers. The turbo pump is connected via an electrically insulated valve, and can bring the inside of the insert at a pressure below 10^{-6} mbar, as measured by the gauge. The tube

[1] Minus K 1000BM-1CMM
[2] Agilent TPS compact
[3] Pfeiffer IKR 251

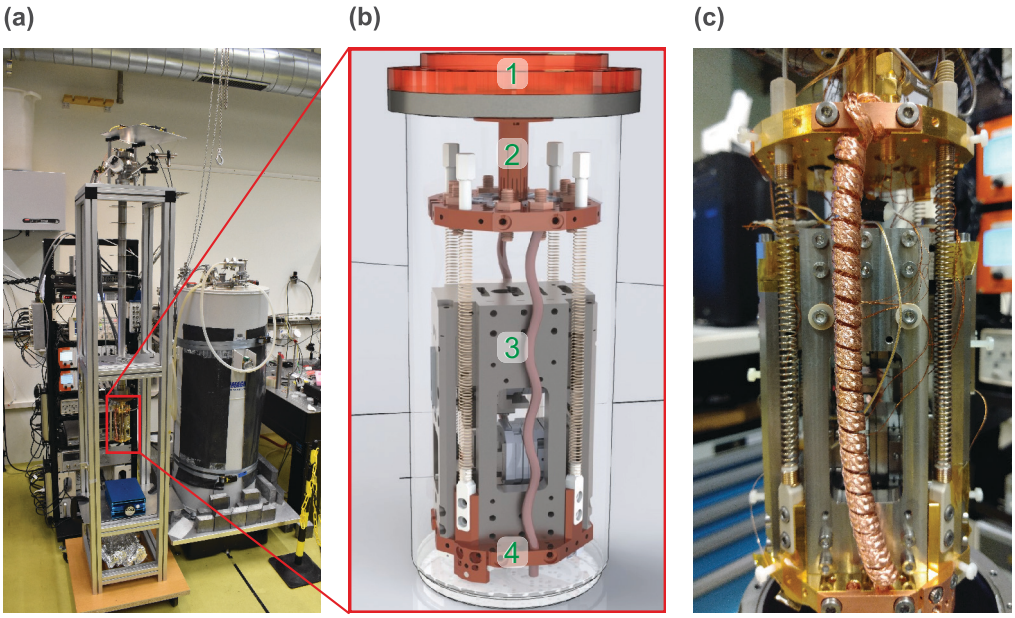

FIGURE 4.1: The experimental platform. **(a)** left to right: high-vacuum insert and ^{4}He cryostat. **(b)**: CAD model of the probe attached to the bottom of the insert. The steel vacuum can is shown transparent. 1: copper flange, 2: top copper plate, 3: titanium cage, 4: bottom copper plate. **(c)**: Actual assembled probe.

of the insert guides several single-mode and multi-mode optical fibers[4], 4 coaxial cables[5], 10 phosphor bronze twisted pairs and 12 manganin wires. The phosphor bronze wires have a resistance of 6 Ω, suitable for driving piezoelectric stepper positioners. The manganin wires have a lower thermal conductivity at the cost of a higher resistance of 50 Ω and are meant for all other low frequency electronic signals. At the bottom of the tube, a copper flange (pictured at the top of Fig. 4.1(b)) is soldered, which comes into direct contact with the helium bath and provides a thermal link to the probe which attaches to its center part. The copper flange also serves as a mating interface for the indium vacuum seal which is formed with the stainless steel can that attaches to its outer part and completes the insert. The entire insert can be lifted from the cryostat and held in a custom cart in order to work on the probe, as shown in Fig. 4.1(a).

4.1.2 Probe design

The probe comprises a copper top plate which attaches to the bottom of the insert and a copper bottom plate onto which the cage hosting the experimental system is mounted (Fig. 4.1(b,c)). The bottom plate is suspended to the top plate by four 16 cm-long copper beryllium springs with a spring constant of $0.023\,\mathrm{N}\cdot\mathrm{mm}^{-1}$ which further shield the experimental system from mechanical noise. Two copper braids, arranged so as to minimally influence the suspension system, provide a thermal link between the two copper plates. A temperature sensor[6] mounted on the bottom plate

[4] IVG fiber Cu800 & Cu50-125
[5] UT-085-SS-SS, Microstock
[6] Lakeshore CX-1030-MT-1.4L

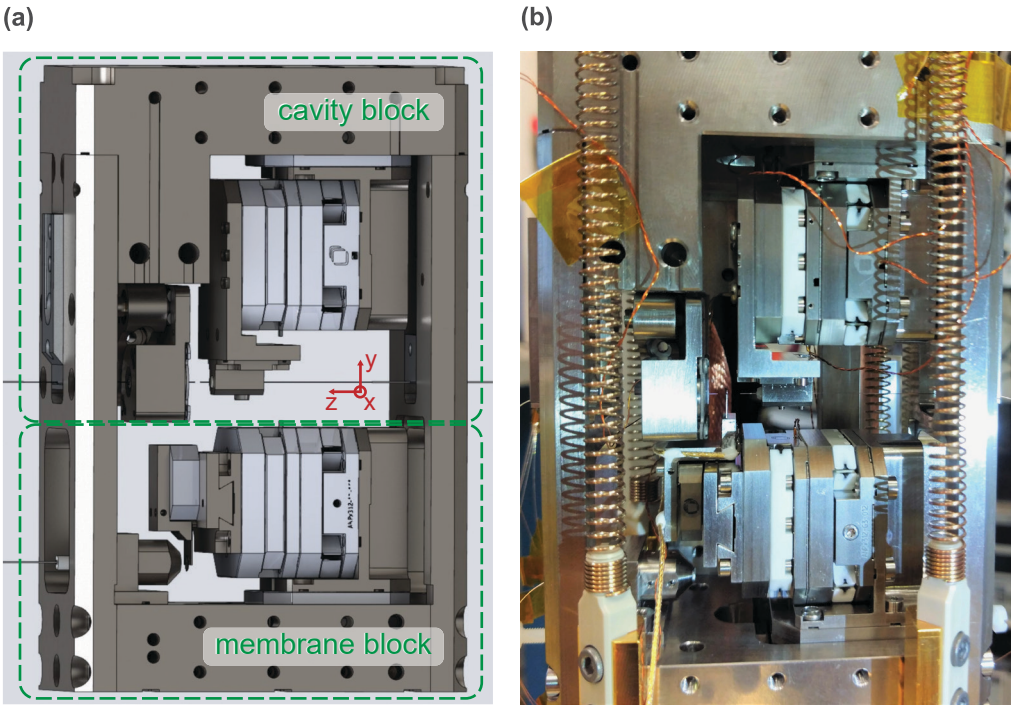

FIGURE 4.2: **(a)** CAD model and **(b)** picture of the titanium cage hosting the experimental system. The top part (cavity block) holds the fiber-based Fabry-Perot cavity. The bottom part (membrane block) holds the sample. The coordinate system shown in red in (a) corresponds to the coordinate system used throughout the text. In **(a)** the sample is held in front of a fiber-based confocal microscope, in **(b)** in the middle of the optical cavity.

is used to monitor the temperature of experimental system. The coaxial cables, electrical wires and optical fibers guided through the insert pass through the middle of the copper flange. The coaxial cables are connected to 0 dB attenuators[7] screwed into the top plate, acting as thermal anchors. The electrical wires are soldered to 6-pin connectors fixed on the top plate, to which the elements of the experimental system are then connected. Optical fibers are further guided to the experimental system. The entire probe fits in the vacuum can (inner dimensions: diameter 10.2 cm, height 24.6 cm) without touching it in order to avoid transmitting mechanical vibrations.

The experimental system is hosted in a titanium cage pictured in Fig. 4.2, consisting of two blocks, each holding one part of the MIM system: the membrane block and the cavity block. These two blocks are assembled together by two pillars and the rigidity of the assembly is further increased by two side plates (not shown in Fig. 4.2 for clarity). All structural components are made out of titanium to maximize the mechanical stability of the experimental system, and to favor even thermal contraction.

The cavity block holds the fiber-based Fabry-Perot cavity. On the right side of Fig. 4.3(a), a fiber mirror is held in a fixed mount attached to a stack of 3 piezoelectric steppers[8], providing 6 mm of linear motion in the x, y and z directions. On the left side of Fig. 4.3(a), a second fiber mirror is held in a titanium disk inside the faceplate of a custom-made kinematic mount. As visible in the cutout shown in

[7] XMA 4880-5523-00-CRYO
[8] Attocube ANPx312

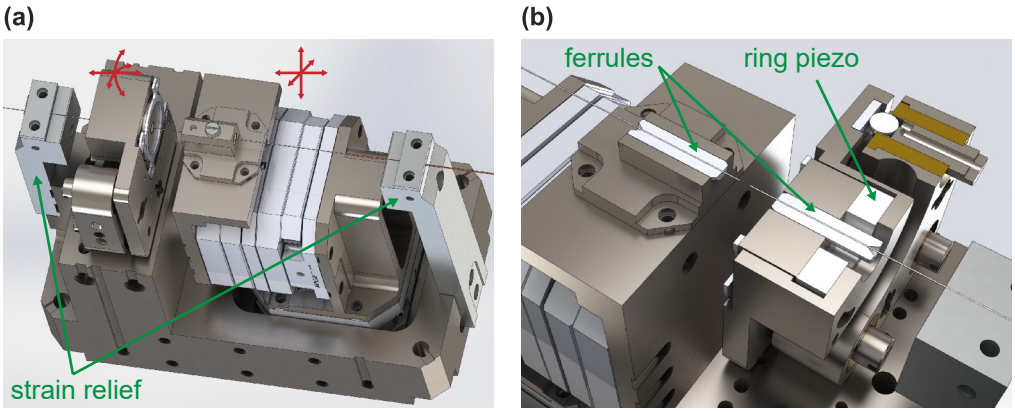

FIGURE 4.3: **(a)**: CAD model of the cavity block. The red arrows indicate the degrees of freedom associated with each element. **(b)**: horizontal cutout showing the inside of the parts holding the fiber mirrors.

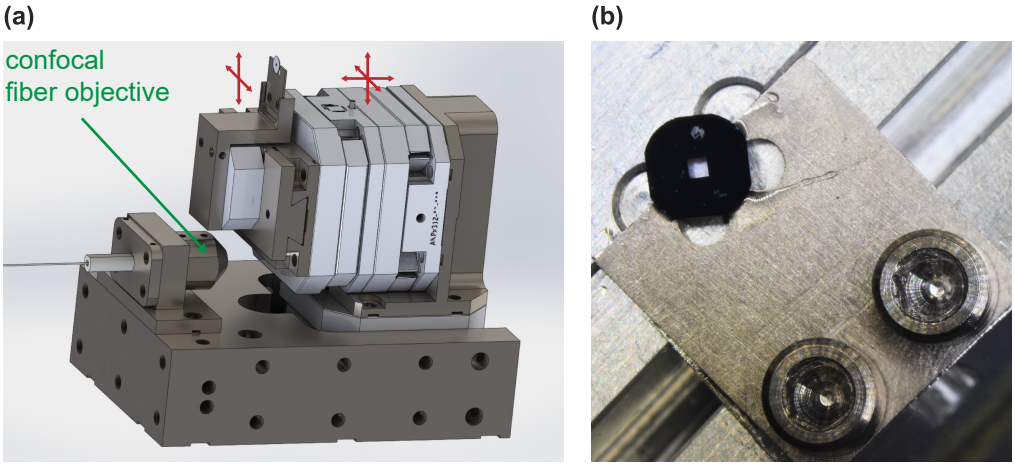

FIGURE 4.4: **(a):** CAD model of the membrane block. The red arrows indicate the degrees of freedom associated with each element. **(b):** picture of one of the carrier plates to which samples are glued.

Fig. 4.3(b), the titanium disk is clamped against a ring piezoelectric positioner by a spring. The kinematic mount allows for manual tip/tilt adjustment of the cavity alignment, while the ring piezo provides short-range, high-bandwidth tunability of the cavity length. Both fibers are guided through a groove acting as a strain relief while allowing for motion along the z direction.

The membrane block can hold the sample in two different configurations. In the first configuration, which is pictured in Fig. 4.4(a), and which is the one used for the results presented in this thesis, the sample is held in-between the two fiber mirrors of the cavity block. In the second configuration, the sample is held in front of a fiber-based confocal reflection microscope, which can be used to interferometrically detect the motion of the sample [128]. In both configurations, the sample is glued on a carrier plate (see Fig. 4.4(b)) which is attached to a L-shaped holder. The design of the carrier and the sample gluing process are described in details in

Section 5.1.2. The L-shaped holder additionally features a 3 mm-diameter, 0.25 mm-thick disk piezoelectric element[9], glued under the place where the sample carrier attaches, and allowing for resonant driving of mechanical modes in the sample. The L-shaped holder is fixed to a xy piezoelectric scanner[10] providing 30x30 µm (resp. 15x15 µm) of continuous motion at room temperature (resp. 4 K). The piezo scanner is itself fixed to the male part of a dovetail assembly, which allows for relatively pain-free sample change. The female part of the dovetail assembly is attached to a stack of 3 piezoelectric steppers[11], providing 6 mm of linear motion in the x, y and z directions.

The mechanical workshop in the Physics Department of the University of Basel provided feedback on the design and machined the many elements of the probe. Overall, the probe offers 5 degrees of freedom for the alignment of the fiber cavity (x/y/z/tip/tilt, of which x/y/z can be actuated remotely and at cryogenic temperatures) and 3 degrees of freedom for the positioning of the sample (x/y/z can be actuated remotely and at cryogenic temperatures). In addition, the length of the fiber cavity can be finely tuned with a high bandwidth, the position of the sample can be continuously scanned in xy, and mechanical resonances of the sample can be resonantly driven.

4.2 Assembling the Experimental Platform

In this section we describe the assembly of the experimental platform and its operation.

4.2.1 Assembling and aligning the fiber cavity

Here we describe the process of assembling the cavity block illustrated in Fig. 4.3. The process begins with adequately prepared fiber mirrors as described in Section 3.3.5. Custom made helper parts are used to transfer these fibers from their storage plate to either a fixed holder or a disk (left and right of Fig. 4.3 respectively). The fiber in the disk holder is usually a single-mode fiber since it is typically used as the input to the cavity for practical reasons. The disk holder is then placed against the ring piezo in the kinematic mount which is held facing upwards during the operation. The assembly of this side of the cavity is completed by clamping the disk holder inside the mount with the spring, then transferring the mount to the cavity block. The other side of the cavity is completed by simply attaching the fixed holder directly on the cavity block. During the whole process, care is being taken to applying shearing forces to the fiber behind the ferrule since it is likely to result in the fiber breaking at this point. The fibers are then guided through a groove which acts as a strain relief while still allowing for the fibers to move along the z axis.

The alignment of the cavity is performed in three steps. The first step is purely visual. Two USB microscopes are set up around the cavity block, which is attached to an optical table. The cameras are placed perpendicular to each other in a plane normal to the cavity axis so that they both show the two fiber mirrors. The xy and tip/tilt degrees of freedom of the cavity block are used to visually align the two fiber mirrors so that they face each other and appear perfectly parallel on both cameras. For the second step a HeNe laser is send to the input fiber and the reflection

[9] PI PIC151
[10] Attocube ANSxy50
[11] Attocube ANPx312

and transmission signals are collected. At this point the fiber mirrors are already aligned well enough to detect a transmission signal, and the xy degree of freedom is used to maximize it. A sawtooth electronic signal is then sent to the positioner controlling the z degree of freedom in order to modulate the length of the cavity. Since the HeNe laser is outside of the stopband of the mirror coating, a low finesse etalon is formed and a sinusoidal amplitude modulation appears on the reflection and transmission signal. The xy and tip/tilt (when tip/tilt is available, i.e. outside the cryostat) degrees of freedom are used to maximize the depth of this modulation. For the third step, the cavity is connected to the laser system described in Section 2.2. A high finesse cavity signal typically appears both in reflection and in transmission upon modulating the cavity length. The xy and tip/tilt (when available) degrees of freedom are used to minimize higher order modes while maximizing the maximum transmission of the fundamental resonance in transmission and minimizing its width, thus ensuring that the best achievable mode-matching is obtained [78]. This optimization step typically starts using the highest gain setting on the transmission photodiode, which is then progressively reduced by up to 3 orders of magnitude as the best alignment is gradually achieved.

Once this alignment process is completed, the properties of the optical cavity are ideally characterized on the tabletop, before transferring the cavity block to the probe.

4.2.2 Assembling the probe

Here we detail the procedures used for assembling or modifying the probe. They are all carried out with the insert fixed on the custom stand shown in Fig. 4.1(a).

The following procedure is used for the initial assembly of the system. It starts from assembled sample and cavity blocks, with the FFPC pre-aligned as described in Section 4.2.1. The top copper plate is first attached to the copper flange at the bottom of the insert, and the bottom copper plate, to which the temperature sensor has been attached, is rigidly held below it using a helper spacer part. The sample block is then bolted on the bottom copper plate, and one pillar and one side plate are attached to it. The cavity plate is taken from the tabletop, flipped upside down, inserted carefully with the fiber going through the opening in the side pillar, and bolted in place. The second pillar and the second side plate can then be attached. At this point the two fiber mirrors are spliced to the adequate optical fibers from the insert, and the splice is then protected using a thin layer of silver epoxy. We found that silver epoxy adds strength to te splice while remaining flexible enough to allow the fiber to be coiled in custom PEEK fiber reels located under the bottom copper plate. The two fiber mirrors must be bent just outside the strain relief posts of the cavity block so that they do not touch the sides of the vacuum can later on (see Fig. 4.1(c)). This is one of the most delicate steps, during which the fiber mirrors are at risk of being broken. Once the desired shape is achieved, the fibers are secured to the side pillars using Kapton tape and copper wire. At this point the wires from the stepper positioners, sample scanner, ring piezo, shaker piezo, and temperature sensor are connected. The copper braids are then clamped to the top and bottom copper plate and the copper beryllium springs joining the two plates are installed. The helper spacer part is finally removed, and the lengths of the springs are fine tuned so that the bottom of the probe hangs straight from the top plate. Nylon screws are added to all four sides of the cage to serve as bumpers preventing the probe and most importantly the fibers from hitting the can once the system is closed.

The following procedure is used for changing the fiber cavity. The existing fibers are first uncoiled from the fiber reels and the splices are cut. The stepper positioners of the fiber block, and the ring piezo are disconnected. One side plate and one side pillar are removed, allowing for the extraction of the cavity block from the probe. The cavity block is then modified as needed on the tabletop. The reverse steps are followed to install the fiber block back into the probe. While changes to the fiber cavity are a significant undertaking, the design of the probe makes the process as painless as possible, with no probe element apart from the cavity block needing to be unplugged or removed.

The following procedure is used for changing the sample. The sample scanner and shaker piezo are first disconnected. One side plate is then removed, allowing for the extraction of the sliding dovetail part which holds the sample assembly. The sample assembly is then modified as needed, and the reverse steps are followed to install it back into the probe. Changing the sample is convenient enough that it can be done routinely.

At this point the insert only needs to be connected to the laser system, and to the piezo controllers to become fully operational. The experimental platform can come to be operated under a variety of different experimental conditions which impact the characteristics of the individual experimental systems, and in particular the stability of the optical cavity. For instance, the insert can be on the stand outside the cryostat, or fixed inside the cryostat, where it benefits from the additional shielding from seismic noise provided by the passive vibration isolation platform. The probe can be rigidly fixed to the copper top plate with the helper spacer part, or suspended from it with the springs. The probe can be exposed to air currents when the vacuum can is not installed, or shielded from them either at room pressure or in high vacuum. The temperature of the experimental system can be either room temperature, nitrogen temperature or ^{4}He temperature depending on the contents of the bucket cryostat. Finally, when the cryostat in at 4 K, the superconducting magnet can be turned on and the magnetic field can be tuned between 0 and 8 T.

4.2.3 Operating the experimental platform

Here we describe the different procedures for achieving the experimental conditions previously mentioned. These include closing and operating the vacuum system, transferring the insert into the bucket cryostat, and operating the cryostat.

The following procedure is used for closing the vacuum system, which requires sliding the vacuum can over the probe and achieving a vacuum seal with the copper flange at the bottom of the insert. The mating surfaces between the copper flange and the vacuum can are first cleaned with isopropanol. A piece of indium wire is wiped with IPA and placed into a dedicated ridge on the top surface of the vacuum can. A lab jack is then used to carefully lift the vacuum can and slide it over the probe, avoiding contact as much as possible. The vacuum can is bolted to the copper flange with stainless steel screws, which are progressively tightened following a star pattern. The turbo pump is then connected to the valve at the top of the insert and the system is brought to high vacuum. We usually expect the pressure measured by the vacuum gauge at the top of the insert to arrive in the 10^{-6} mbar range within a few hours. At this point the insert is ready to be transferred to the cryostat.

The following procedure is used for transferring the insert to the cryostat. The cavity fibers are taken apart so that they are separated by about 100 µm and the sample is positioned roughly in the middle of them so that possible shocks to the probe do not lead to them crashing into each other. The HeNe laser is connected

to the cavity during the process, and the cavity transmission signal is monitored. The valve to the vacuum system is then closed and the pump is disconnected from the insert, as well as all BNC cables, leaving only the optical fibers connected to the insert during the procedure. The cart on which the insert is mounted is rolled under the crane, which is hooked to the top of the insert. The insert is lifted from its cart until it clears the top of the cryostat and is translated directly above the bucket of the cryostat. The insert is then slowly let down into the cryostat, lowering the vacuum can past the baffles and finally into the magnet bore. Any jerking motion during those steps makes the probe oscillate laterally and hit the side of the vacuum can, potentially damaging or misaligning the experimental system. The top plate of the insert is then bolted to the top of the cryostat, and the pump and BNC cables are connected to the insert once again. At this point, the system is ready for cooldown.

The cooldown procedure depends on the state of the experimental platform. If the cryostat is empty and at room temperature, the bucket is first filled with nitrogen. The temperature at the bottom copper plate of the probe is monitored until it reaches 77 K. The liquid nitrogen is then pushed out of the bucket with helium gas, and liquid helium is transferred into it. If the insert was taken out of the cold cryostat for a quick modification, the vacuum can is first dipped into a bucket of liquid nitrogen until it reaches 77 K, then the insert is transferred to the cryostat while it still contains liquid helium. In both cases, the temperature at the bottom copper plate of the probe is monitored until it reaches 4.2 K. The transmission of the HeNe laser through the cavity is monitored during the cooldown, and lateral xy adjustments of the fiber mirror position are made to compensate misalignments caused by thermal contraction of the probe. If the cavity signal is lost, it can be found again following the alignment procedure described previously (starting from the HeNe laser step).

With the cryostat at 4.2 K, the current in the superconducting magnet can be ramped up in order to achieve the desired magnetic field. At this point, the magnet is usually operated in persistent mode in order to avoid heating the system up, thus maintaining a low level of helium consumption.

4.3 Testing the Fiber-Based Optical Cavity

In this section we present experimental results illustrating the operation of fiber cavities and their characterization procedure. On the basis of these results, we highlight and discuss the fine points of their behavior. We then use the fiber cavity to evaluate the mechanical stability of the experimental system under different environmental conditions.

4.3.1 Fundamental and higher-order resonances of the fiber cavity

Here we discuss the basic cavity scan experiment introduced in Section 2.2.2. The experimental data presented in this subsection were not acquired in the cavity block described above, but using a modified probe dedicated to characterizing single fiber mirrors. In this probe, a fiber mirror is placed in front of a flat mirror which was coated during the same run. The degrees of freedom of the system are the same as in the cavity block described above, and it is similarly connected to the laser system with the fiber mirror under test acting as the input to the cavity. In addition, the cavity modes can be imaged through the flat mirror using a simple CMOS sensor[12]. Fiber 181 (see Table 3.2) was used for the measurement shown here.

[12] Thorlabs DCC3240N

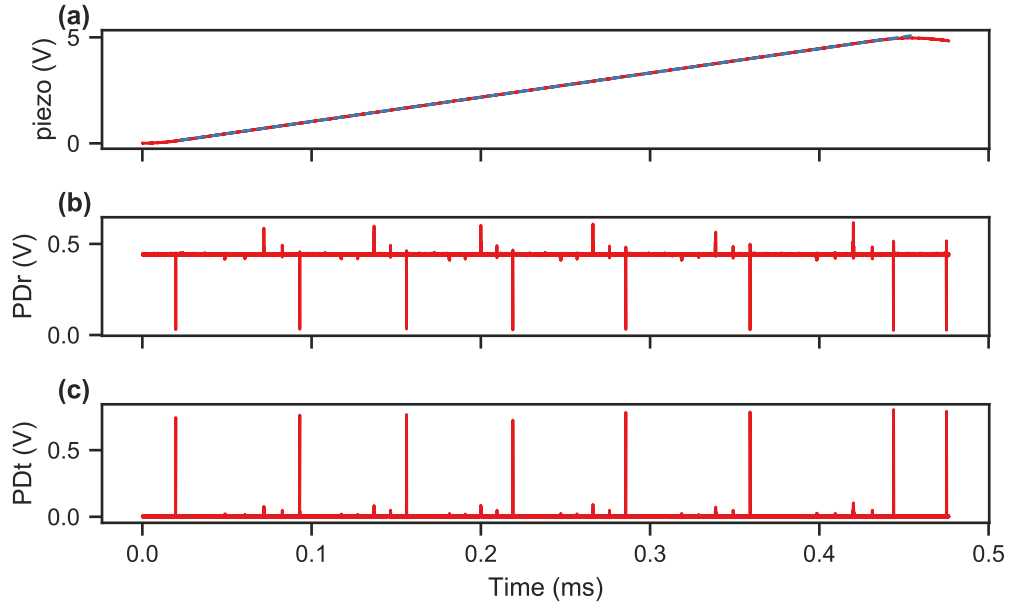

FIGURE 4.5: Data acquired during a cavity scan. **(a)**: voltage ramp sent to the piezo controller. The blue line is a fit to the linear part. **(b, c)**: signal collected on the reflection and transmission photodiodes.

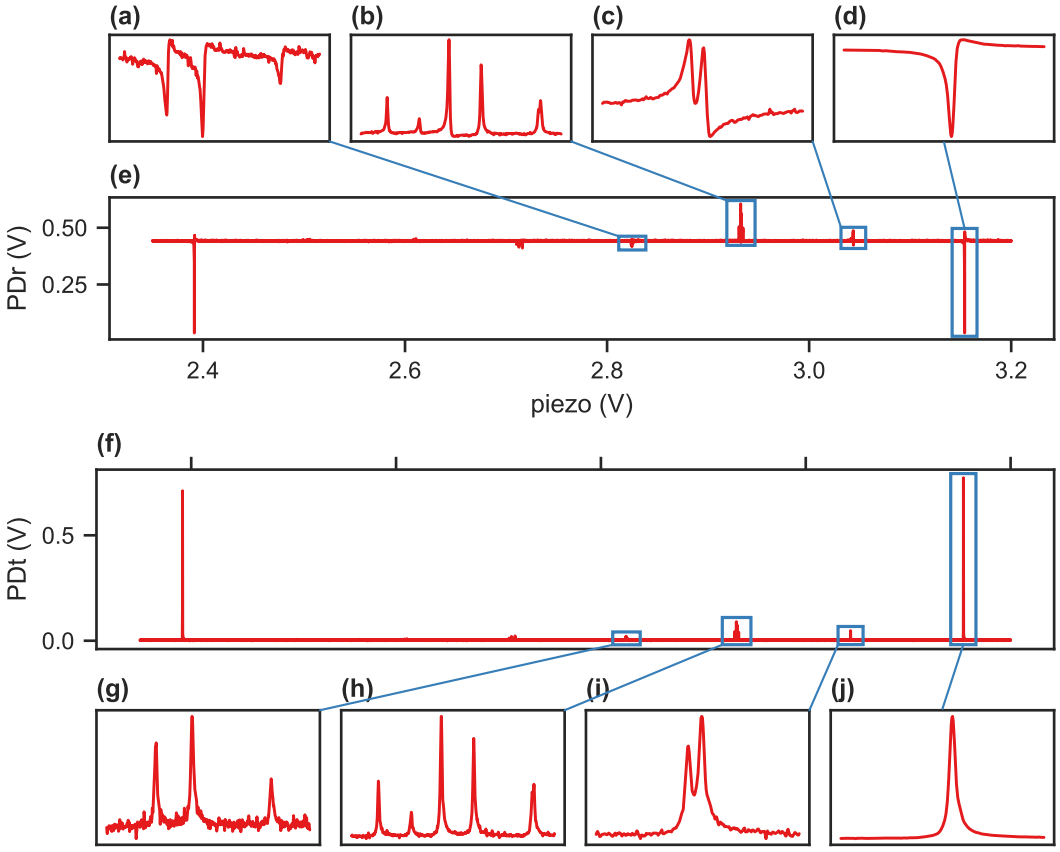

FIGURE 4.6: Data extracted from Fig. 4.5. **(e, f)**: reflection and transmission signals versus piezo voltage. **(a-d, g-j)**: zoom ins on resonances.

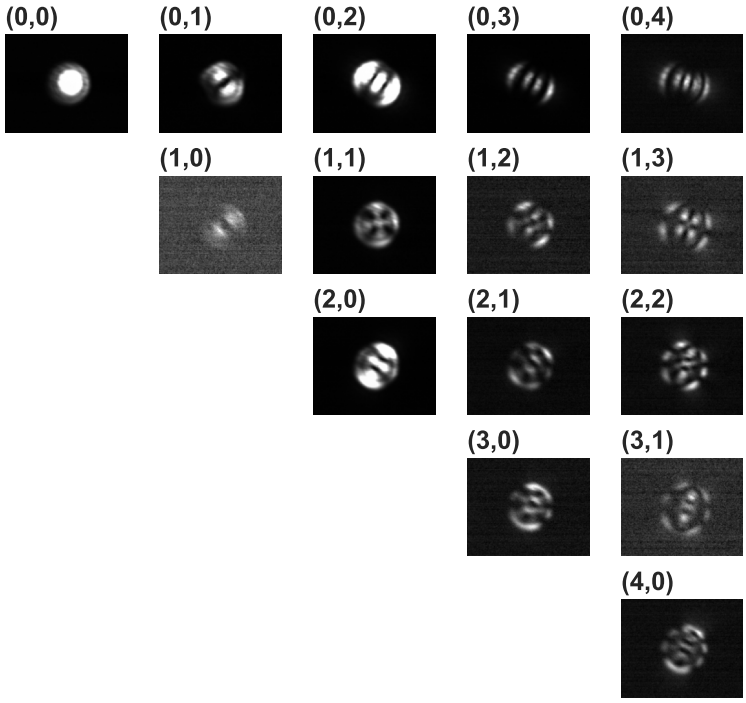

FIGURE 4.7: Pictures of the cavity modes taken through the transmission mirror. **(0,0)** corresponds to Fig. 4.6(j), order 1 modes **(1,0)** and **(0,1)** to (i), order 2 modes to (j), order 3 modes to (i).

As detailed in Section 2.2.2, a cavity scan is performed by continuously varying the detuning between the cavity and the laser held at a fixed wavelength by changing the cavity length. This is achieved by sending a S-shaped voltage ramp to a piezoelectric positioner controlling the cavity length, which can be either the DC input of the stepper piezo for long range scans or the ring piezoelectric element for short range scans. The data acquired by a fast DAQ during a long range scan is shown in Fig. 4.5. The piezo voltage in Fig. 4.5(a) is the voltage sent to the piezo controller, which is multiplied internally by a factor of 15 before being applied to the actual piezoeletric element. The blue dashed line in Fig. 4.5(a) is a fit to the linear part of the voltage ramp. Only the data acquired within this time interval is used for analysis, and the best fit values of the piezo voltage are used when other parameters are plotted against it in order to reduce jitter. The cavity transmission and reflection signal shown in Fig. 4.5(b,c) confirm that the scan spans several times the cavity free spectral range, with the fundamental cavity resonances appearing as the highest peaks or deepest dips, while higher-order resonances appear in-between.

Figure 4.6(e) and (f) respectively show a slice of the reflection and transmission data in Fig. 4.5, taken around one free spectral range of the cavity, and plotted against the piezo voltage. Figure 4.6(a-d) and (g-j) respectively show zoom ins on individual cavity resonances in (e) and (f), and are a first step towards confirming the identification of the fundamental cavity resonances, as well as that of other resonances corresponding to higher order modes. The even spacing of those higher order resonances, evident from Fig. 4.6(e) and (f), suggest they correspond to modes of successive order 1, 2, and 3 as per Eq. (1.60), but the number of peaks in the corresponding zoom ins do not match the expected 2, 3 and 4 separate modes at this mode order.

In order to investigate this matter further, we set the piezo voltage so as to individually tune each of the cavity modes in resonance with the laser and image

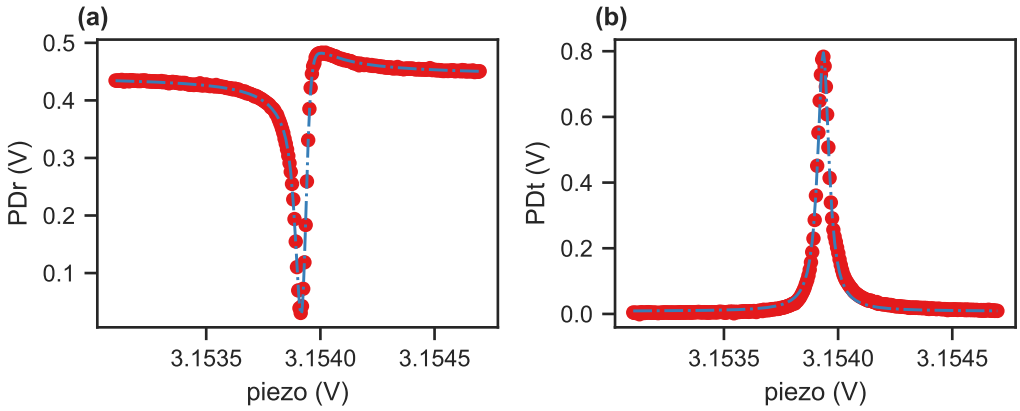

FIGURE 4.8: **(a,b)**: data in Fig. 4.6(d, j), fitted using Eqs. (1.21) and (1.76).

the cavity mode through the back mirror. The images are shown in Fig. 4.7, with mode (0,0) taken within the voltage range of window (j) in Fig. 4.6, modes of order 1 within (i), modes of order 2 within (h), modes of order 3 within (g), and modes of order 4 corresponding to the next group of peaks. These images further confirm that the higher-order resonances in Fig. 4.6 correspond to the expected mode order. The fact that the fine splitting between higher-order modes of the same order does not immediately correspond to what is expected from Eq. (1.60) can have various explanations, which will be discussed in 4.3.2. The rather large coupling to higher-order modes displayed in this data is due to the short radius of curvature of fiber 181, which leads to a cavity waist that is significantly smaller than the fiber mode size, resulting in significant mismatch with the fundamental cavity mode.

Figure 4.8 shows fits to the lineshapes of the fundamental resonance in reflection and transmission, respectively using Eq. (1.76) and Eq. (1.21) as the fit functions, with the Lorentzian part replaced by a pseudo-Voigt profile to account for Gaussian peak broadening. The Gaussian part is below 0.05 for both fits, indicating a low amount of Gaussian broadening in the timescale of the scan around resonance. A dispersive shape of the reflection signal is observed, as expected for fiber cavities [78, 129]. The fits give access to the cavity linewidth in terms of voltage κ_V, and to the parameters A, B and C in Eq. (1.76). As discussed in Section 2.2.2, the cavity linewidth κ can be determined if the input field is modulated at a known frequency (see Section 4.3.3). Then, given a separate characterization of $|\beta|$ obtained by comparing the direct reflection from the cavity with that from a calibrated retroreflector [108], one can extract cavity parameters $|\alpha|^2 \kappa_{ex,1}$ and ξ from A, B and C by solving the coupled equations Eq. (1.77) [60]. Extracting the value of $\kappa_{ex,2}$ requires a full calibration of the optical losses in the experiment.

4.3.2 Mode-mixing effects in fiber cavities

Here we discuss mode-mixing effects in fiber cavities [75] by analyzing cavity scans taken at increasingly long values of cavity length. The experimental data presented in this subsection were acquired in an early version of the cavity block described above, operated on the tabletop, with fiber 197 as the input fiber and fiber 266 as the transmission fiber.

The data plotted in Fig. 4.9 was acquired and transformed following the procedure described in [75]. The cavity length is first shortened to the minimum desired

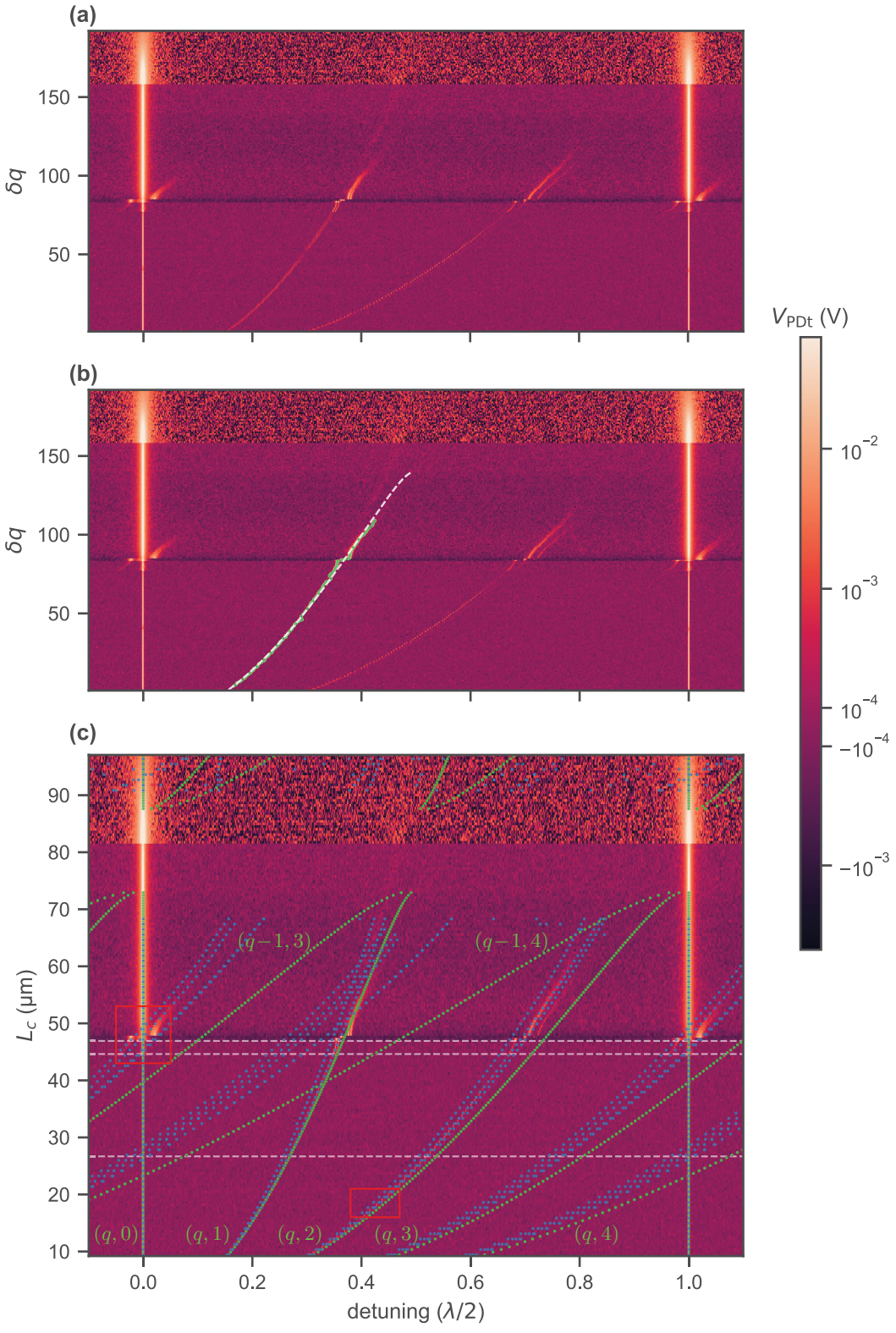

FIGURE 4.9: Resonance spectrum of the cavity as a function of cavity length. **(a)**: experimental data. The changes in background level at $\delta q \approx \{85, 160\}$ are due to changes in photodiode gain. **(b)**: green dots show the points fitted to Eq. (1.61), the resulting best fit is the dashed white line. **(c)**: blue markers are the resonance frequencies according to Eq. (1.60) up to mode order 4, green markers are those obtained from the mode-mixing simulation using the measured fiber profiles, and are annotated with their mode order. The horizontal dashed lines correspond to dips in the measured finesse (Fig. 4.10). The red outlines correspond to zooms in shown in Fig. 4.12.

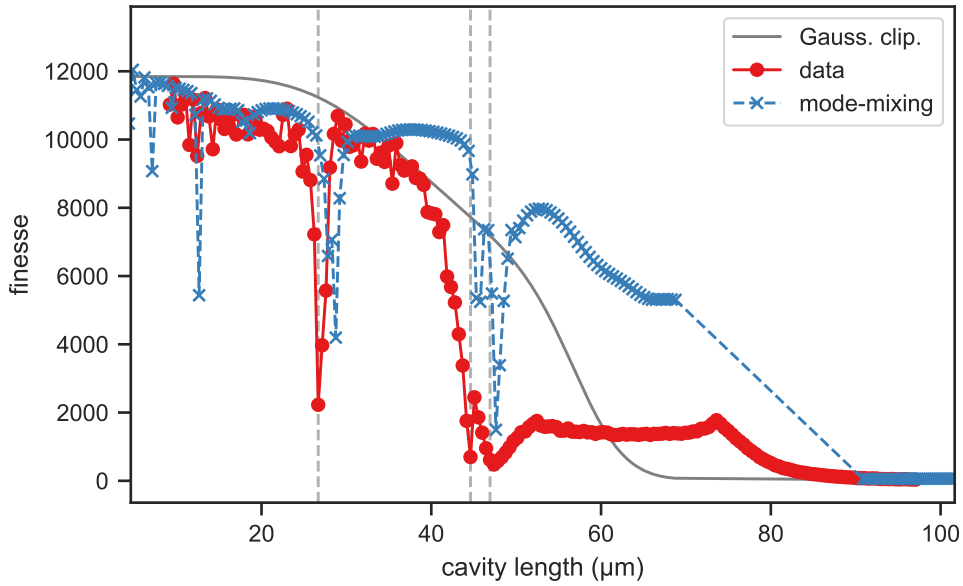

FIGURE 4.10: Finesse of the fundamental mode of the cavity as a function of cavity length. The red curve corresponds to the finesse measured from the experimental data presented in Fig. 4.9. The blue curve is calculated numerically while the green curve is calculated analytically from clipping losses as per Eq. (1.47). The blue and green curves have been rescaled to match the start of the experimentally measured finesse.

length. The first cavity scan is taken and data is acquired as described in the previous subsection. After the cavity scan, the stepper controlling the length of the optical cavity is stepped to increase the length of the cavity by about one third of the free spectral range. Another cavity scan is taken and the process is repeated until the maximum desired cavity length is reached (usually when all signal is lost). The gain of the transmission photodiode is adjusted as necessary for each cavity length.

Post-processing is performed on the transmission data when possible, since it provides the largest range of usable cavity lengths thanks to the adjustable gain . Stepping by less than one time the FSR between each scan makes it possible to track fundamental resonances of the same order across different cavity scans. For each available order δq of the fundamental mode, we select a window of data between δq to $\delta q + 1$ from within cavity scans in which this range appears. An effort is made to ensure each selected window of data starts at approximately the same piezo voltage in order to limit the effect of piezo nonlinearities. The coordinate axis of each selected window is then normalized by the FSR so that the resonance δq is centered at 0 and resonance $\delta q + 1$ is centered at 1, yielding a detuning. Finally, the transmission signal in each window is plotted as a function of detuning and δq, with each row of the plot showing data between $\delta q = \text{row}$ and $\delta q = \text{row} + 1$. The resulting plot of the cavity resonance spectrum is shown in Fig. 4.9(a).

The detuning of the first higher order mode as a function of δq can be fitted with Eq. (1.61). From this fit, one can extract the radii of curvature of the fiber mirror $R_{c,1}$ and $R_{c,2}$, as well as the order of the first mode present in the data q_0 such that $q = q_0 + \delta q$. The value of q_0 provides a quantitative estimate of the cavity length $L_c = (q_0 + \delta q)\,\lambda/2$. Figure 4.9(b) shows the data that was used for this fit as green markers overlayed on the experimental data, with the best fit curve shown as a white

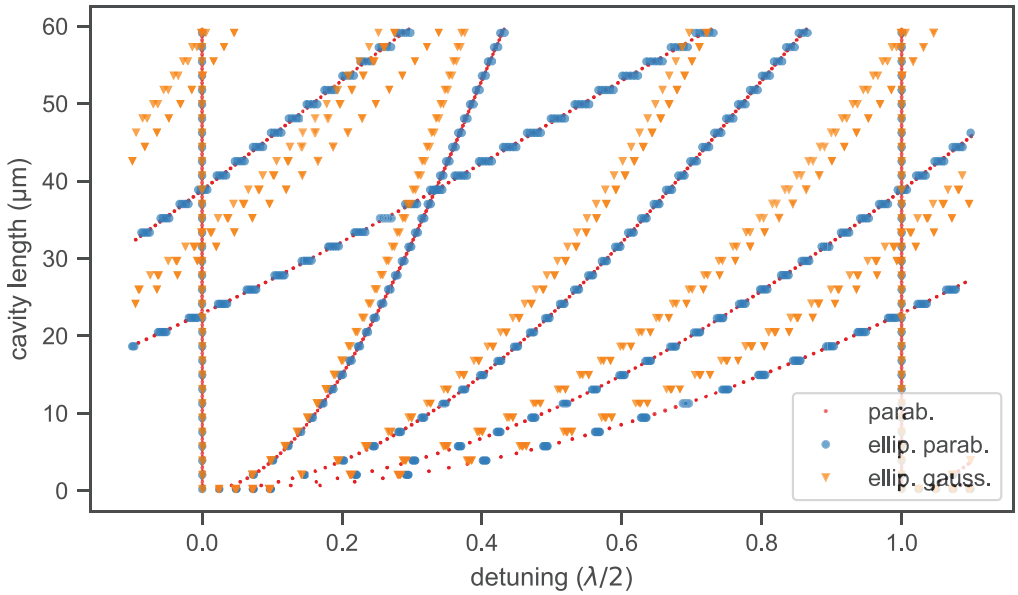

FIGURE 4.11: Mode-mixing simulations of cavity resonance spectra up to order 4, using ideal mirror profiles of various shapes.

dashed line. The fit yielded $q_0 = 19$, $R_{c,1} = 73.3\,\mu\text{m}$ and $R_{c,2} = 87.4\,\mu\text{m}$, with the radii of curvature matching reasonably well those estimated from the profilometric data (Table 3.2). Figure 4.9(c) uses the calibrated cavity length on the y axis.

The fundamental resonance lineshape for each value of δq is fitted using a pseudo-Voigt profile to determine its finesse as per Eq. (2.3). The finesse of the fundamental mode is plotted as a function of cavity length in Fig. 4.10 (red markers). In order to support the discussion of the experimental data, a numerical simulation of the cavity resonance spectrum and of the associated losses has been performed following the formalism introduced in Section 1.1.4, using the actual profilometer-measured fiber mirror shapes for the calculation. The result of this simulation is shown in blue in Fig. 4.9(c) and in Fig. 4.10. As a point of comparison, the cavity resonance spectrum calculated using Eq. (1.60) and the values of $R_{c,1}$ and $R_{c,2}$ extracted from the fit is plotted in green in Fig. 4.9(c), and the finesse calculated using Eq. (1.47) for Gaussian clipping losses and aperture diameters estimated from profilometric measurements for each fiber mirror (see Table 3.2) is plotted in green in Fig. 4.10. The simulated and calculated finesse were both rescaled to match the measured finesse for the shortest cavity lengths.

Looking at the measured data in Fig. 4.10, three components of the evolution of finesse can be distinguished. The most prevalent effect is a rapid decrease when the cavity length approaches 50 µm, which matches the Gaussian clipping model loosely and is due to the spot size of the fundamental cavity mode becoming comparable with the value of D_{sph} of the mirrors. Secondly, sharp dips in finesse occur at specific cavity lengths, which are reproduced in the mode-mixing simulation. Matching guides for the eyes corresponding to these dips are included in Fig. 4.9(c), showing that the dips occur at cavity lengths where higher order modes of longitudinal order q become resonant with the fundamental mode of longitudinal order $q + 1$. Finally, both the measured data and the mode-mixing simulation exhibit a gradual decrease in finesse at cavity lengths shorter than about 10 µm, which does not match the Gaussian clipping model.

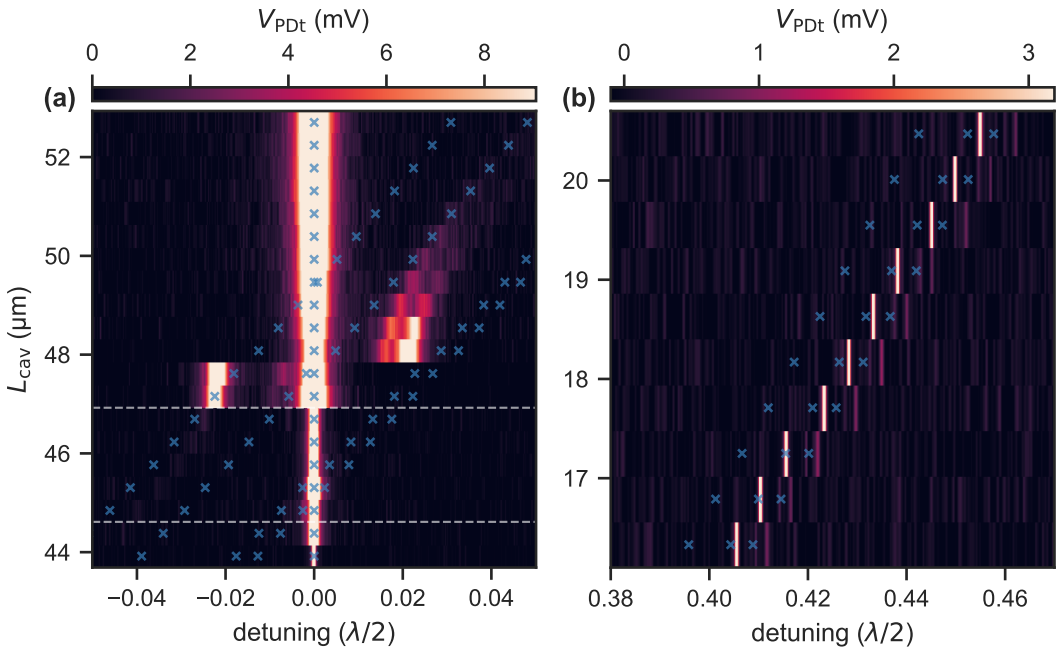

FIGURE 4.12: Zoom ins on parts of the resonance spectrum outlined in red in Fig. 4.9(c). **(a)**: mode crossing between the fundamental mode and the third order high-order modes. **(b)**: fine splitting of the second order transverse mode.

We attribute the discrepancy between measured data and the mode-mixing simulation for long cavities to a change in the alignment of the cavity as the cavity length is increased.

In order to investigate the physical origin of these effects, as well as the discrepancies between the measured and calculated resonance spectra, we performed mode-mixing simulations using ideal mirror profiles, following the procedure described in 1.1.4. The mirror profiles used for these simulations were parabolic, parabolic with elliptic cross-section, parabolic with elliptic cross-section and a finite diameter, gaussian with elliptic cross-section, and gaussian with elliptic cross-section and added small-scale roughness. In all cases the profiles were chosen so that the radius of curvature in their center matches the value of R_c (or $R_{c,a/b}$ in the case of elliptic cross-section) of fibers 197 and 266 (Table 3.2). Similarly, the finite diameter case uses the value of D_{sph} of fibers 197 and 266. The resonance spectrums obtained from the mode-mixing simulations and corresponding to the paraboloid, elliptical paraboloid and elliptical gaussian are plotted in Fig. 4.11. The finesse values obtained from the mode-mixing simulations and corresponding to the elliptical paraboloid, clipped elliptical paraboloid, elliptical gaussian and elliptical gaussian with added roughness are plotted in Fig. 4.13.

In Fig. 4.11, the resonances obtained for the symmetric cross-section paraboloid match the resonances calculated with Eq. (1.60) and shown in green in Fig. 4.9(c) exactly. The resonances obtained with the elliptical paraboloid show a lifting of the degeneracy between high-order modes of the same transverse order, which still perfectly matches the expectations from Eq. (1.60). On the other hand, the resonances obtained with the elliptic gaussian profile significantly deviate from the standard theory, both in their overall behavior and in the fine splitting between high-order

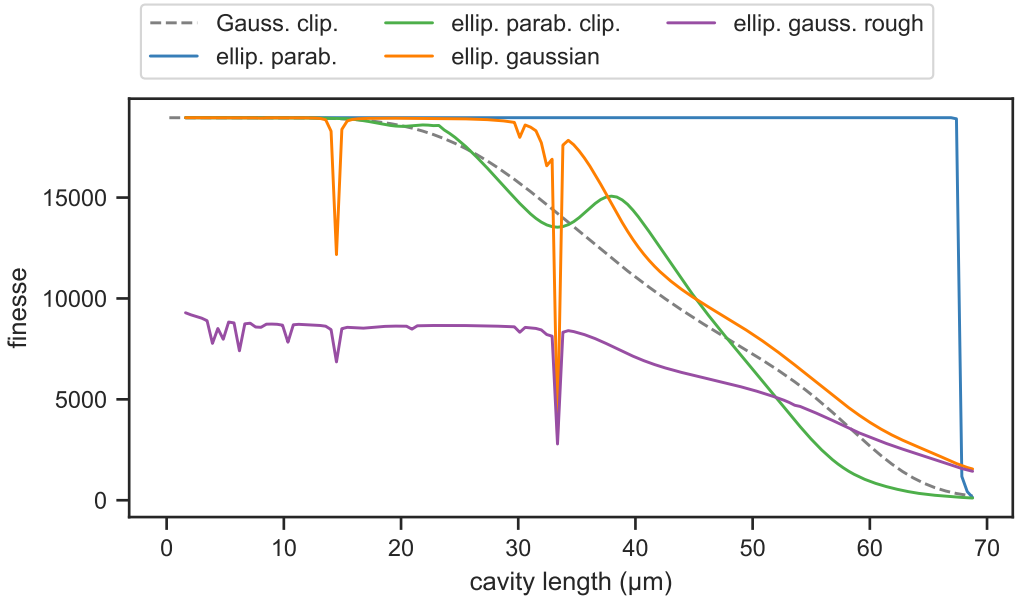

FIGURE 4.13: Mode-mixing simulations of the finesse of the fundamental cavity mode, using ideal mirror profiles of various shapes.

modes of the same transverse order. Both these effects are due the radius of curvature of the gaussian profile increasingly deviating from the radius of curvature of the ideal parabolic mirror as the distance from the center increases. This causes an increasingly large deviation from the expected detuning as the cavity length and thus the spot size of the modes on the mirrors increase. In addition, modes that sample different areas of the mirror, for instance (0,2)/(2,0) and (1,1), experience different effective radii of curvatures leading to a modification of the fine splitting, with (1,1) being increasingly split from (0,2)/(2,0) which remain nearly degenerate. This fine splitting effect is also observed in the experimental data, as can be seen in Fig. 4.12, which shows zoom ins on the data from Fig. 4.9(c). The deviation from the standard theory is a sign that the higher-order modes of the cavity deviate from pure Hermite-Gauss modes, and are instead mixtures of Hermite-Gauss modes.

In Fig. 4.13, the finesse obtained for the infinite paraboloid stays constant until the cavity length reaches the end of the stability regime as expected. The overall behavior of the finesse obtained for the finite diameter paraboloid and for the gaussian profiles matches the finesse calculated using the clipped Gaussian model. The main difference are broad dips for the finesse obtained for the finite diameter paraboloid, and sharp dips for the finesse obtained with the gaussian profiles. Those dips correspond to high-order modes of longitudinal order q becoming resonant with the fundamental mode of longitudinal order $q+1$, fulfilling Eq. (1.62). The onset of clipping losses as calculated using the clipped Gaussian model (Eq. (1.47)) indicates that the spot size of the fundamental mode is getting large enough to feel the finite dimension of the mirror. From the mode-mixing point of view, this leads to off-diagonal elements entering the mixing matrices and resonant cavity modes becoming mixtures of Hermite-Gauss modes, leading to increased losses. As a result, when high-order modes become resonant with the fundamental mode, their overlap is non-zero and the fundamental mode hybridizes with the high-order modes. The larger spot size of high-order modes leads to an increase in the clipping losses experienced by the hybridized fundamental mode and therefore a drop in finesse. In

the case of the gaussian profiles, because the mirror shape differs from a paraboloid, the mode-mixing effects appear for shorter cavities. They are also stronger, and the additional fine-splitting between high-order modes lead to sharp dips in the finesse when each of these modes crosses the fundamental mode. The effect of added roughness on the finesse obtained with the gaussian profile is three-folds. First, the finesse is decreased for all cavity length due to scatter losses, as explored in [80]. Second, a decrease in finesse occurs for short cavity lengths, which matches what has been observed with experimental data and mode-mixing simulations in Fig. 4.11, as well as published data (e.g. [75]). Third, mode-mixing effects are enhanced, leading to new dips appearing in the finesse data.

In light of these observations, several remarks can be made regarding the operation and characterization of fiber cavities. Mode-mixing effects arising from the gaussian-like shape of CO_2 ablated fiber mirrors lead to a significantly shortened range of cavity lengths at which a high finesse cavity can be maintained. The choice of radius of curvature with which to work must take this into account, or advanced CO_2-ablation technique should be used to modify the shape of the fiber mirrors [104]. Because the fit to the high-order mode separation assumes pure Hermite-Gauss modes, mode-mixing effects are a source of error for the extraction of the cavity length. On the positive side, high-order modes can be harnessed to achieve higher resolution in microscopy applications [125], to locally enhance the cavity field potentially increasing the interaction with systems inside the cavity [130], or to achieve a more homogeneously distributed field intensity [131].

4.3.3 Measuring cavity length, linewidth and finesse

Here we discuss the pros and cons of the different methods available to characterize the length, linewidth and finesse of the fiber cavity. The experimental data presented in this subsection were acquired in the cavity block described above, operated on the tabletop, with fiber 196 as the input fiber and fiber 262 as the transmission fiber.

Cavity length

Knowledge of the cavity length is not only a prerequisite to the determination of other cavity parameters, but it is also crucial from a practical point of view in order to avoid collisions between the fiber mirrors and the sample. A distinction has to be made between the optical cavity length L_c (used for the calculation of $\Delta\omega_{\mathrm{FSR}}$), the geometric cavity length $L_{c,\mathrm{geom}}$, and the distance d_{fibers} between the facets of the fiber mirrors. These quantities are related through:

$$L_c(\lambda) = L_{\tau,1}(\lambda) + L_{c,\mathrm{geom}} + L_{\tau,2}(\lambda) \tag{4.1}$$

$$d_{\mathrm{fibers}} = L_{c,\mathrm{geom}} - t_1 - t_2 \tag{4.2}$$

where $L_{\tau,i}(\lambda)$ is the frequency penetration depth of the cavity field into mirror i [111], and t_i is the depth of the crater on fiber mirror i.

Several methods can be used to measure the cavity length: optical microscopy, scanning the laser wavelength across one free spectral range of the cavity, sending white light into the cavity and collecting the transmitted and/or reflected spectrum as introduced in Section 2.3.2, and fitting the higher order mode separation as introduced in Section 4.3.2.

The fiber cavities discussed in this work are operated without direct optical access to them in most cases, with cavity lengths ranging between 10 µm and 200 µm.

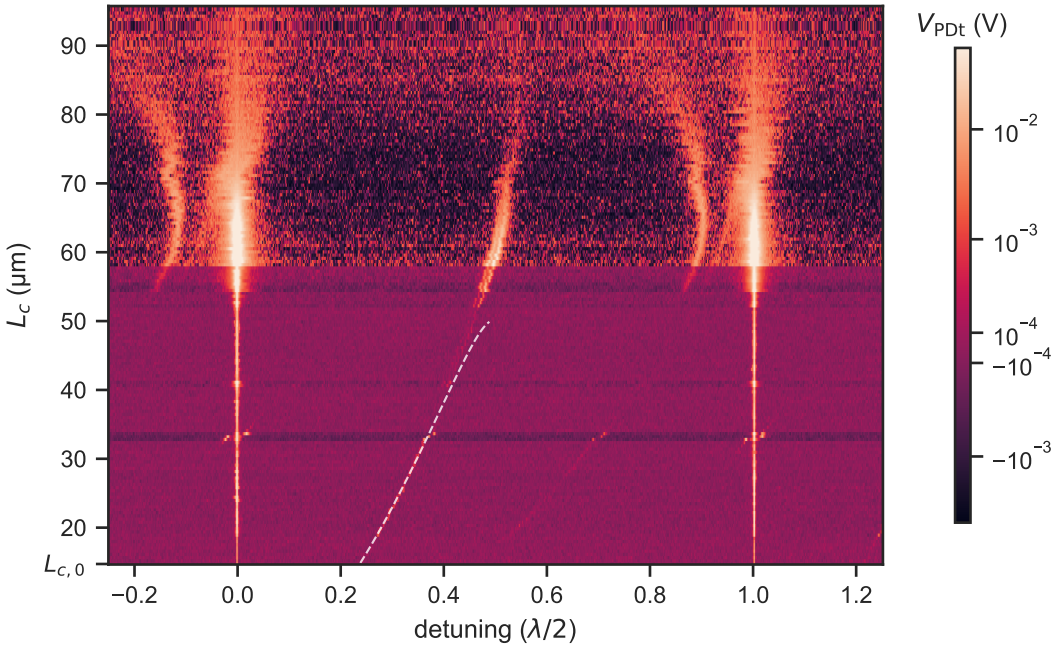

FIGURE 4.14: Resonance spectrum of the cavity as a function of cavity length. The white dashed line is the best fit to higher order mode separation. The changes in background level at $L_c = \{33, 41, 55, 85\}$ µm are due to changes in photodiode gain.

The depth of the mirrors is on the order of 1 µm. Due to the absence of optical access and because crater depth can represent a large portion of the cavity length, optical microscopy is not a suitable method. Scanning the laser wavelength across one free spectral range of the cavity is technically impractical due to the large free spectral range of short cavities which requires to tune the laser wavelength across more than 80 nm in the most extreme cases. In cases when it is technically possible, scanning the laser is time consuming and requires a complex experimental procedure involving performing continuous cavity scans while the laser wavelength is being tuned in order to not miss the sharp cavity resonances. Fitting the higher order mode separation is technically possible, and the time consuming scan of the cavity length across about 40 µm that is necessary to obtain a reliable estimate only has to be performed once. However the deviation of the shape of fiber mirrors from perfect parabola introduces some errors in the fit and fitting higher order modes sometimes requires some level of misalignment to be introduced so that they are not fully suppressed. Sending white light to the cavity and analyzing the transmitted and/or reflected spectrum is fast and practical, but requires either a high resolution spectrometer operating within the mirror stopband or careful consideration of the wavelength dependence of the properties of the mirror coating outside of the mirror stopband

Figure 4.14 shows the resonance spectrum of the fiber cavity considered in this subsection. A fit to the higher order mode separation yields $q_0 = 31$, which corresponds to $L_{c,0} = 14.3\,\mu\text{m}$. Taking into account a modal penetration depth $L_D = 0.34\,\mu\text{m}$, the geometric cavity length $L_{\text{geom},0} = 13.6\,\mu\text{m}$ is obtained.

Figure 4.15 shows the result of a white-light spectroscopy measurement of the cavity length (following the procedure introduced in Section 2.3.2), which was performed before the start of the acquisition of the data for Fig. 4.14. The fit yields an estimate of the geometric cavity length $L_{\text{geom},0} = 9.2\,\mu\text{m}$. The discrepancies between

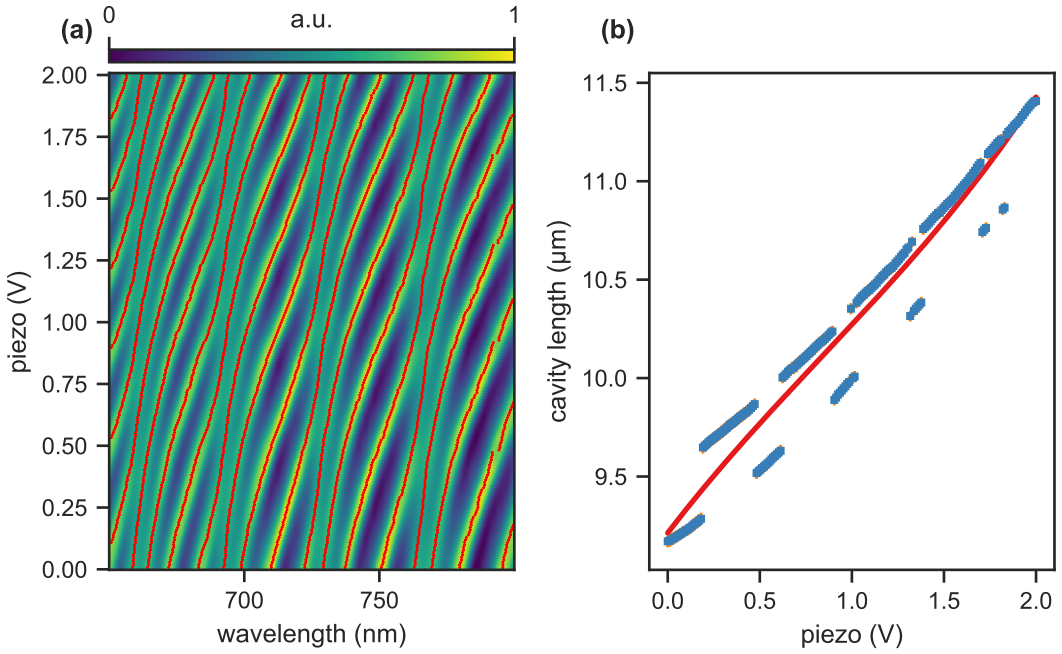

FIGURE 4.15: **(a):** normalized white light transmission spectrum. Red markers show the peak positions extracted from the data. **(b):** geometric cavity length extracted from the fit to this data following Section 2.3.2.

the two estimates of the geometric cavity length are currently being investigated. We note that the amplitude of the discrepancy does not scale with cavity length and is therefore significant only for very short cavities.

Cavity linewidth and finesse

An absolute measurement of the cavity linewidth requires the use of a calibration tone serving as a frequency reference, as illustrated in Section 2.2.2. Figure 4.16 shows the cavity reflection and transmission taken around a fundamental resonance, and corresponding to the first row in Fig. 4.14. During this measurement, the EOM was driven with a single tone at $\omega_{\mathrm{EOM}} = 8.03\,\mathrm{GHz}$. A fit to the data using the sum of three pseudo-Voigt-based lineshapes yields $\kappa_V = 0.042\,\mathrm{mV}$ and $d_{\mathrm{sb},V} = 0.352\,\mathrm{mV}$. These values are inserted into Eq. (2.1) to obtain $\kappa/(2\pi) = 0.97\,\mathrm{GHz}$.

Having characterized both the linewidth and the cavity length, the finesse can now be calculated from Eq. (2.2). Using $L_{\mathrm{geom},0} = 13.6\,\mu\mathrm{m}$ from the fit of higher order mode separation yields $\mathcal{F} = 11379$, while using $L_{\mathrm{geom},0} = 9.2\,\mu\mathrm{m}$ from the fit to white light transmission peaks yields $\mathcal{F} = 16821$. As a point of comparison, the finesse calculated using Eq. (2.3) is $\mathcal{F} = 11199$, which seems to indicate that the fit to higher order mode separation provides an accurate estimate of the cavity length while the fit to white light transmission peaks underestimates it.

Figure 4.17 shows both the finesse calculated using Eq. (2.3) as in Fig. 4.10 and the finesse calculated from Eq. (2.2) using the cavity length estimated from the fit to higher order separation, as a function of cavity length. The two values of finesse are in good general agreement over the whole range of cavity lengths, with the finesse estimated from the cavity length looking smoother. This is expected since the finesse estimated from the FSR is more sensitive to nonlinearities in the displacement of the

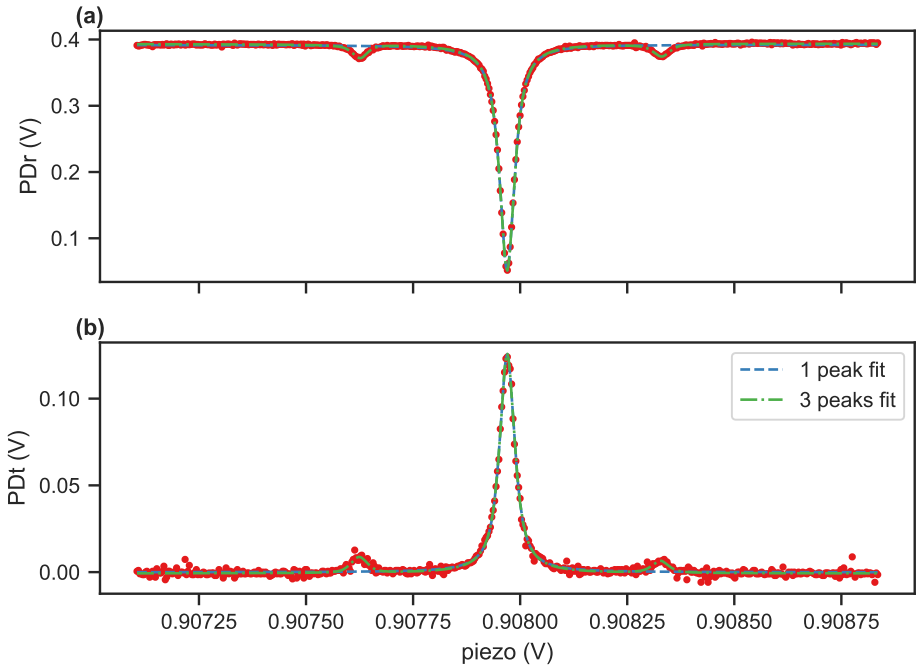

FIGURE 4.16: **(a,b):** cavity reflection and transmission around a fundamental resonance, corresponding to the first row in Fig. 4.14. The blue and green dashed lines are fits to the experimental data using one or three pseudo-Voigt lineshapes, respectively.

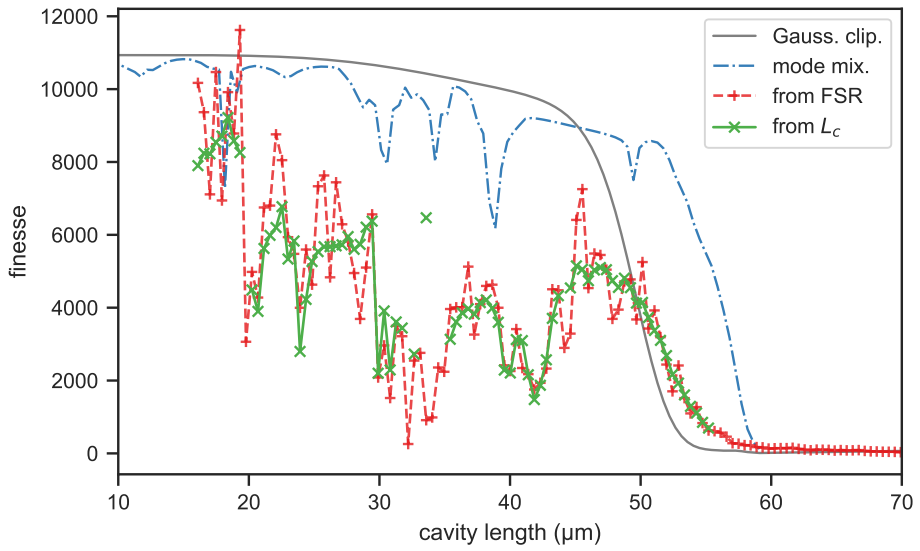

FIGURE 4.17: Finesse of the fundamental mode as a function of cavity length, corresponding to data in Fig. 4.14. Red markers are calculated using Eq. (2.3), with κ_V and $d_{\mathrm{FSR},V}$ extracted from the cavity resonance spectra. Green markers are calculated using Eq. (2.2), with κ extracted from the cavity resonance spectra and L_c extracted from the fit to higher order mode separation in the cavity resonance spectra. The blue and grey curves are respectively calculated with a mode-mixing simulation and a Gaussian clipping model.

piezoelectric element, to noise in the voltage ramp and to small variations in the cavity length due to mechanical instabilities, as previously pointed out in [108]. In light of these observations, we favor the finesse estimated using the cavity length when available, but fall back to the fairly accurate estimate from FSR when necessary.

4.3.4 Stabilizing the fiber cavity

Here we describe the stabilization of the fiber cavity to the laser frequency using the Pound-Drever-Hall technique. The experimental data presented in this subsection were acquired in the cavity block described above, operated on the tabletop, with fiber 197 as the input fiber and fiber 262 as the transmission fiber.

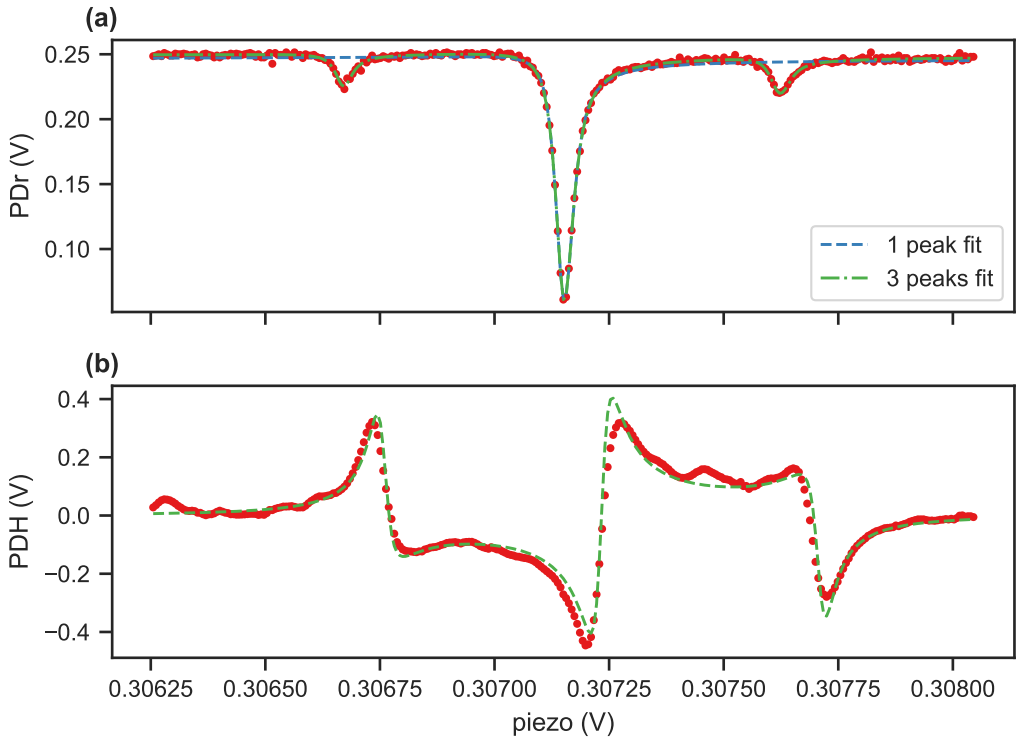

FIGURE 4.18: Cavity scan around a fundamental resonance. **(a)**: cavity reflection signal. The blue and green dashed lines are fits using one or three pseudo-Voigt lineshapes, respectively. **(b)**: Q quadrature of the Pound-Drever-Hall error signal as measured by the lock-in amplifier . The green dashed line is a fit to the imaginary part of Eq. (1.32).

The Pound-Drever-Hall error signal, generated following the procedure outlined in Section 2.2.3 and measured during a cavity scan, is plotted in Fig. 4.18 alongside the cavity reflection signal. The error signal matches the expected PDH response very well, as evidenced by the fit to Eq. (1.32) shown in Fig. 4.18(b), which uses the values of the fit to the cavity reflection, with the only two fit parameters being a scaling factor and a shift in the center detuning. We attribute the shift in center detuning to delay in the electronics.

The results of a response analysis characterization of the system are shown in Fig. 4.19. The vector network analyzer module of the PyRPL GUI is used to drive the system at a frequency that is ramped between 0.5 kHz and 20 kHz while recording the magnitude and phase of the system response at this frequency. The drive is added to the feedback signal sent to the ring piezo.

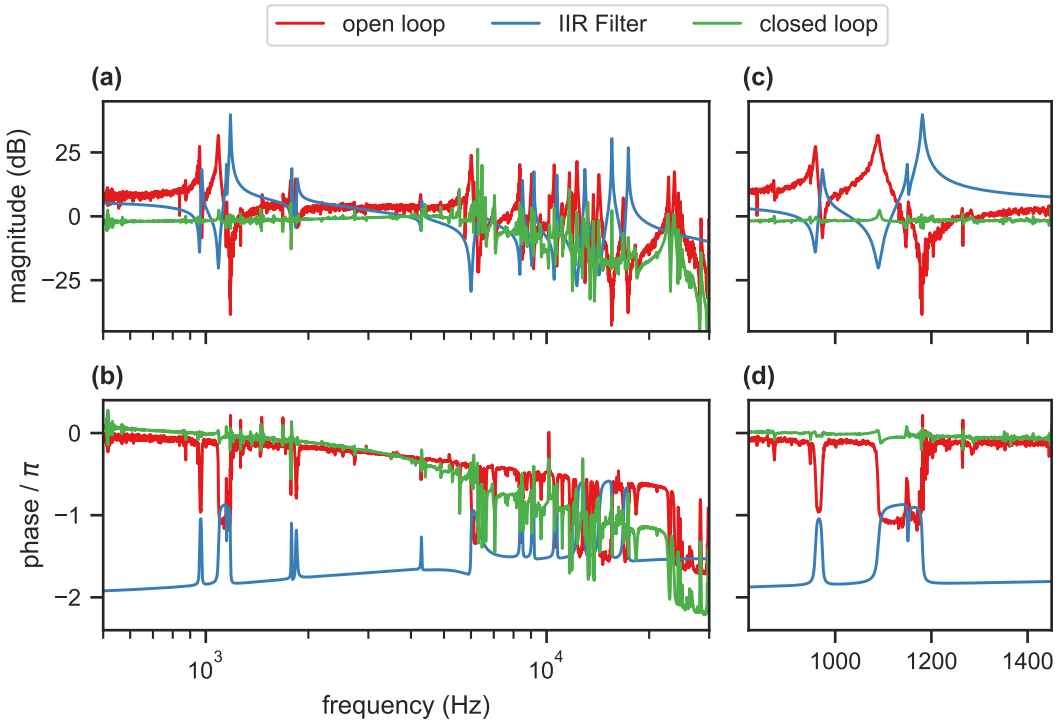

FIGURE 4.19: Response analysis of the cavity lock. Red: open loop response of the error signal. Blue: IIR filter designed to compensate for system resonances. Green: closed loop response of the error signal with IIR filter applied. **(a, b)**: magnitude and phase of the response. **(c, d)**: zoom ins on the first system resonances in (a, b).

This measurement is first performed with the system in quasi open-loop configuration. In this configuration, the feedback signal sent to the ring piezo is low-pass filtered at 10 Hz so as to only cancel low-frequency drifts of the cavity resonance. The magnitude and phase of the system response detected in the error signal, shown in red in Fig. 4.19, is a measure of the mechanical transfer function of the closed-loop system. The first system resonances are a group of three resonances around 1 kHz, which we tentatively attribute to resonances in the stepper positioners which are expected in this frequency range. The next major resonances appear starting from 6 kHz, which we tentatively attribute at least in part to the cantilever mode of the fiber mirrors, which is expected in this frequency range due to the fibers protruding by about 4 mm from the ferrules in which they are glued.

The system resonances strongly hinder the cavity lock, heavily reducing the lock bandwidth and the maximum achievable gain due to any feedback at these frequencies driving the system. We use an Infinite Impulse Response (IIR) filter to cancel the system resonances in the feedback signal before sending it to the ring piezo. The IIR filter is designed in the IIR module of the PyRPL GUI by manually placing zeros and poles in order to obtain a filter that is as close to the inverse of the system transfer function as possible (shown in blue in Fig. 4.19).

The measurement is then performed in closed-loop configuration, with the feedback signal being sent to the ring piezo after application of the IIR signal and low-pass filtering at high frequency. The closed-loop system response, detected in the IIR filtered error signal and shown in green in Fig. 4.19, exhibits heavily attenuated

resonances. We roughly estimate a lock bandwidth of 6 kHz, corresponding to the frequency at which the phase crosses $-\pi$. A more in-depth investigation of the system transfer function and of the lock performance is currently underway.

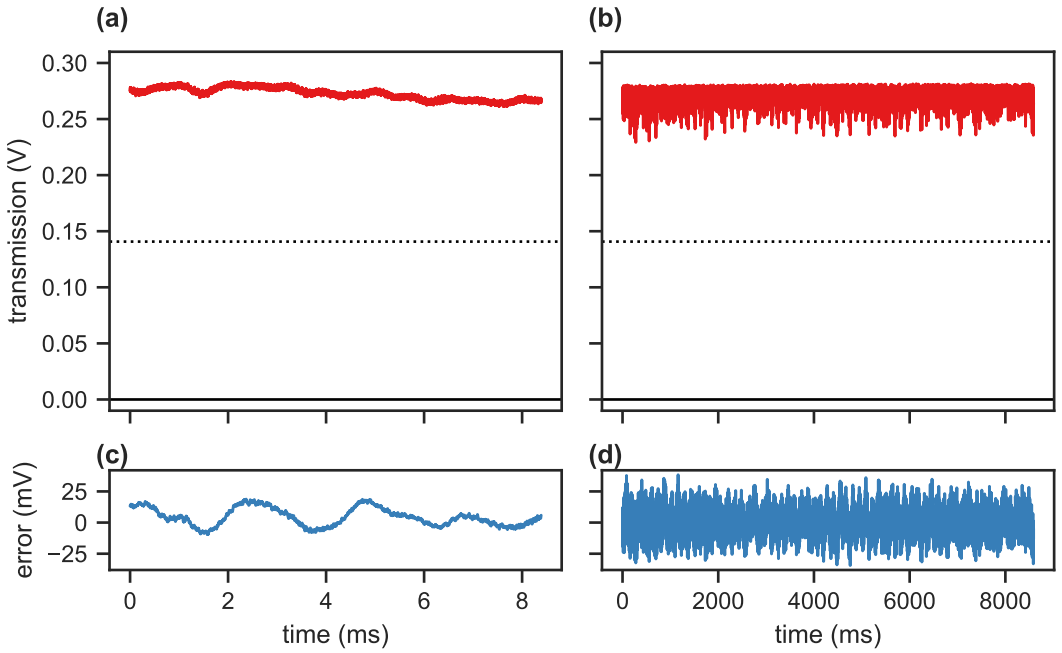

FIGURE 4.20: **(a, b)**: closed-loop cavity transmission as a function of time, for short and long timescales respectively. The dashed line corresponds to half of the cavity maximum transmission. **(c, d)**: corresponding PDH error signal.

The stability of the closed-loop transmission signal is demonstrated in Fig. 4.20, where the cavity detuning stays within 10 % of the maximum cavity transmission for the duration of the measurement. Considering a typical cavity linewidth of 50 pm, we estimate the locked cavity to be stable to within 5 pm. We observed this to remain true on much longer timescales, and the lock to remain stable for many hours without a re-locking system.

4.3.5 Estimating the mechanical stability

Here we present the results of a preliminary study of the mechanical stability of the experimental platform under some of the experimental conditions presented above.

Mechanical noise within the experimental platform is most obvious when looking at the high finesse optical cavity behavior, and is most detrimental to our ability to stabilize it. More specifically, the optical cavity is most sensitive to displacement of the fiber mirrors along the cavity axis, which induces variations in the cavity length and thus in the detuning between the cavity and the fixed laser. Lateral motion of the fiber mirrors comes in as a second order effect, resulting in a misalignment of the optical cavity which induces variation in the maximum transmission (resp. minimum reflection) at resonance, but also small variations in the cavity length. The cavities studied here have a rather small linewidth of around 50 pm in terms of length due to their relatively high finesse of about 10000. This makes it technically challenging to perform a quantitative characterization of the displacement noise of the fiber mirrors since the cavity is a highly nonlinear transducer of any motion on the order of 50 pm

or more, as noted in [74]. Our goal is to reduce noise sources, to increase the shielding of the probe from those noise sources and to dampen mechanical vibrations of the probe until the cavity is stable enough to be actively stabilized to the laser using the PDH error signal. A PDH lock can usually be achieved when the position of the cavity resonance is stable to within the cavity linewidth or less. In order to get a rough estimate of the cavity stability, we perform repeated cavity scans around a fundamental resonance. Assuming that run to run variations in the position of the resonance peak are dominated by variations in the length of the cavity and not for instance to the repeatability of the displacement of the piezoelectric element used for the scan, this measurement should provide a rough estimate of the mechanical stability of the fiber cavity.

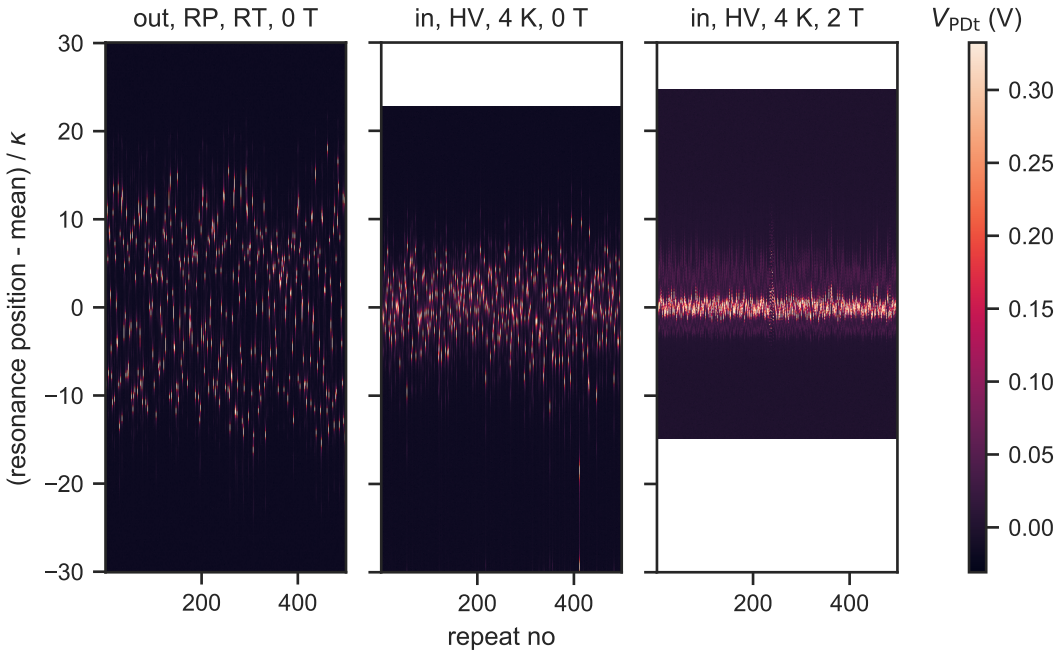

FIGURE 4.21: Repeated cavity scans around a fundamental resonance, under different experimental conditions. (out,RP,RT,0T): probe at room pressure and room temperature, insert fixed outside of the cryostat. (in,HV,4K,0T): probe in high vacuum at 4 K, insert inside the cryostat, magnet off. (in,HV,4K,2T): probe in high vacuum at 4 K, insert inside the cryostat, magnet set to 2 T.

This measurement was performed under three of the different experimental conditions previously listed: with the probe at room pressure and room temperature with the insert fixed outside of the cryostat (RP,RT,0T), with the probe in high vacuum at 4 K with the insert inside the cryostat and the magnet off (HV,4K,0T), and in the same conditions but with the magnet set to 2 T (HV,4K,2T). The repeated cavity scans are shown in Fig. 4.21, with the detuning axis centered around the mean resonance position and normalized to the cavity linewidth. Figure 4.21 provides a visual representation of the variations of the cavity resonance. The fact that there is a very clear effect of experimental conditions on the results of the measurement indicates that they are indeed a major source of run to run variations in the position of the resonance.

A statistical analysis of the run to run variations in the position of the resonance is presented in Fig. 4.22. The standard deviation of the position of the resonance

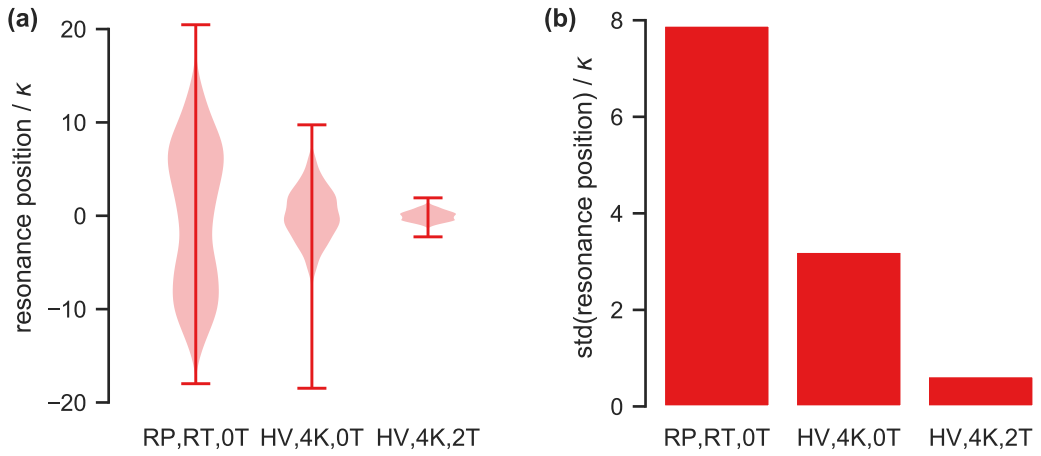

FIGURE 4.22: Statistical analysis of the data in Fig. 4.21. **(a)**: violin plot showing the spread of the resonance positions. **(b)**: bar plot showing the standard deviation of the resonance positions under the different experimental conditions considered. (RP,RT,0T): probe at room pressure and room temperature, insert fixed outside of the cryostat. (HV,4K,0T): probe in high vacuum at 4 K, insert inside the cryostat, magnet off. (HV,4K,2T): probe in high vacuum at 4 K, insert inside the cryostat, magnet set to 2 T.

plotted in Fig. 4.22(b) provides a rough estimate of the amplitude of the mechanical noise, which is conveniently expressed in terms on the cavity linewidth. Transferring the insert from (RP,RT,0T) to (HV,4K,0T) leads to an improvement of the cavity stability from 8 to 3 times the cavity linewidth, which we tentatively attribute to either the increase in shielding from seismic noise of the passive vibration isolation stage or to the decrease in the sensitivity of the piezoelectric elements to voltage noise at 4 K. Increasing the magnetic field in the cryostat to 2 T leads to a further improvement of the cavity stability to less than 1 cavity linewidth, which we attribute to a strong damping of the motion of the bottom copper plate by eddy currents.

Since this preliminary data was taken, we have discovered that electronic noise in the voltage sent to the piezoelectric positioners contributed significantly to the vibrations experienced by the fiber mirrors. The deformation coefficient of the piezoelectric stack in the stepper positioners is $50\,\mathrm{pm}\cdot\mathrm{mV}^{-1}$ at room temperature, and $5\,\mathrm{pm}\cdot\mathrm{mV}^{-1}$ at 4 K. The specified output noise of the ANM300 amplifiers is $<5\,\mathrm{mV}$, which corresponds to a displacement of the fiber mirror by 5 times the cavity linewidth at room temperature, and 0.5 times the cavity linewidth at 4 K. Electronic filters designed and built by the electronics workshop of the Physics Department of the University of Basel are now used to decrease the voltage noise, resulting in a vast improvement in the stability of the optical cavity, in particular at room temperature. During our investigation of electronic noise in the system, several ground loops have also been found and eliminated.

We are now carrying out a more systematic study of the mechanical noise in the improved system under the different experimental conditions, and of the quality of the lock in those conditions. Possible sources of noise are either external to the probe such as seismic noise, acoustic noise, helium boiloff or internal to the probe such as voltage noise to the piezo elements, or thermal motion of the fiber mirrors. We currently believe that acoustic noise is one of the most impactful sources of noise, since the cavity is particularly sensitive to people talking in the lab, leading to noise at

around 400 Hz which could correspond to acoustic resonances of the room. Possible mitigation strategies include improvements to the acoustics of the lab and to the acoustic shielding of the experimental platform. We also expect that thermal motion of the fibers will come to limit the performance of our lock due to the low frequency of their cantilever mode. We are planning to produce new fiber mirrors which protrude less from the ferrules, which would lead to an increase in the frequency of their cantilever mode and a reduced amplitude of their thermal motion.

Chapter 5

Fiber-Based Membrane-in-the-Middle Optomechanics with hBN

In parallel to our work on the experimental platform, we identified hexagonal boron nitride (hBN) as a promising material to be used as the hybrid mechanical resonator. In this chapter we discuss the sample design and fabrication, and present early experimental characterization of the optomechanical interaction between an hBN mechanical resonator and the optical cavity described in the previous chapter.

5.1 hBN as a Hybrid Mechanical Resonator

Motivated by the growing interest in hBN as a host material for bright strain-coupled quantum emitters [61] and for optomechanics [22, 65, 132], we decided to investigate hBN flakes for our hybrid mechanical resonators. Our goal is to generate interesting experimental results about the vibrational properties of hBN while our experiment is maturing towards studying hybrid optomechanical effects. In this section we discuss the design and fabrication of the hBN hybrid mechanical resonator.

5.1.1 Designing the hBN hybrid mechanical resonator

We fabricate suspended hBN drum mechanical resonators by transferring a exfoliated hBN flake on top of a 200 nm-thick pre-patterned holey SiN membrane centered within a 200 µm-thick silicon frame[1], as illustrated in Fig. 5.1. The Norcada frames are ideally suited for our experimental platform since the thin SiN membrane and the backside cavity allow a short fiber cavity to be formed around the sample, in addition to the frames being convenient to mount and to handle, and commercially available. Here we discuss the design parameters for such devices.

The main selection parameter for the hBN flake is its thickness, which determines its reflectivity and plays a role in determining the resonance frequencies and zero-point fluctuation amplitude of the drum mechanical resonator. The main design parameters for the SiN membrane are its dimensions and intrinsic stress, which determine its mechanical resonance frequencies, and the diameter of the holes, which plays a role in determining the resonance frequencies and zero-point fluctuation amplitude of the drum mechanical resonator. Key figures of merit considered for the design of the hBN drum mechanical resonators were their fundamental resonance frequency and bare optomechanical coupling strength $g_0 = G\, x_{\mathrm{zpf}}$, where $x_{\mathrm{zpf}} = \sqrt{\hbar/(2\, m_{\mathrm{eff}}\, \Omega_m)}$ is the zero-point fluctuation amplitude.

[1] Norcada micro-porous range of membranes

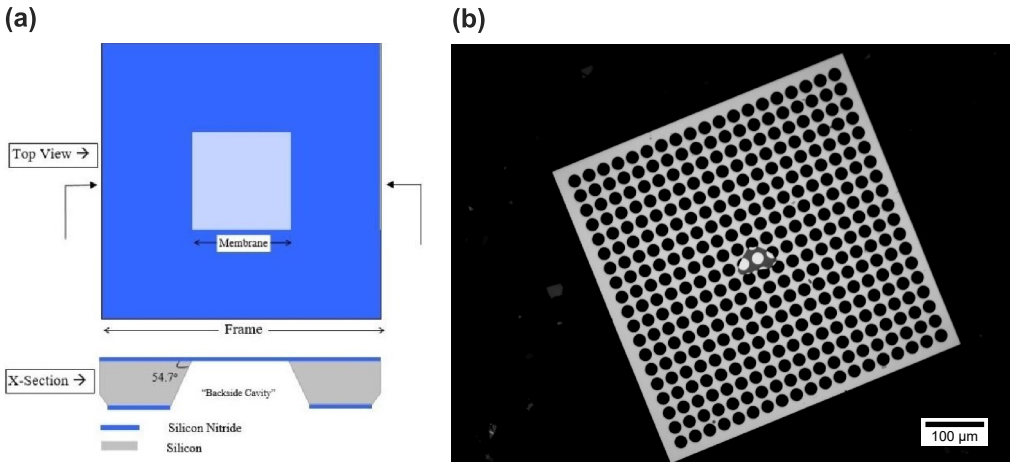

FIGURE 5.1: **(a)**: drawing of a standard Norcada SiN membrane (adapted from www.norcada.com). **(b)**: optical microscope picture of a hBN flake transferred onto a Norcada NH050D2019 micro-porous SiN membrane with 20 µm-diameter holes (sample HS10).

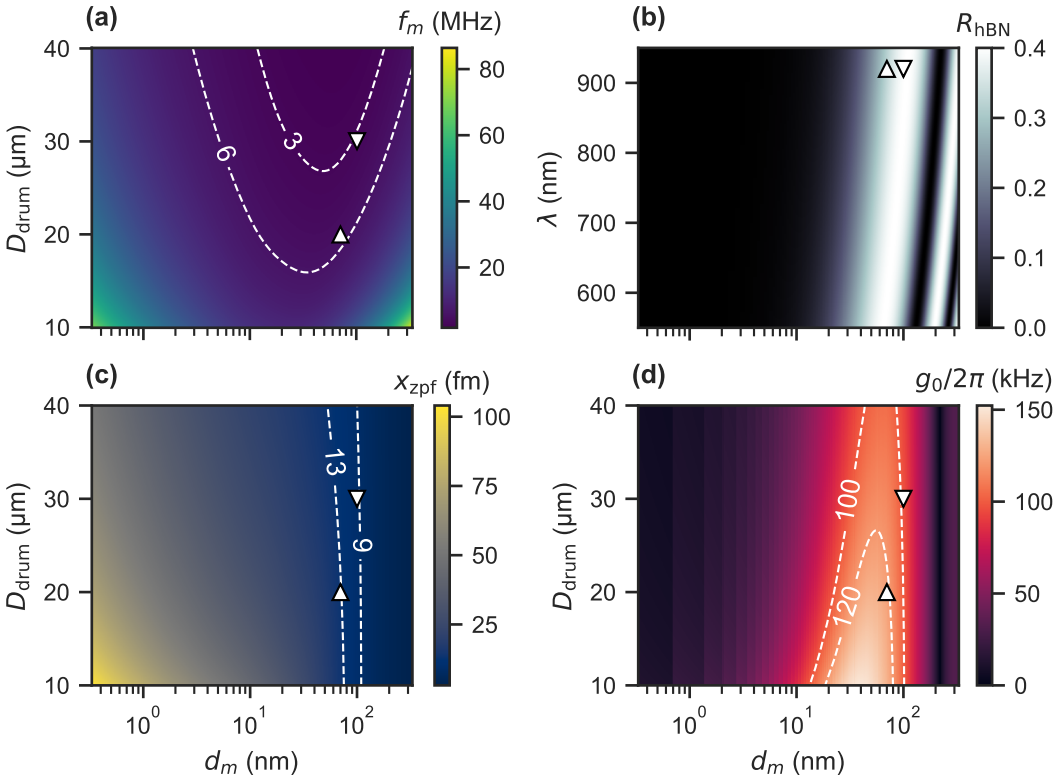

FIGURE 5.2: **(a,c,d)**: predicted fundamental mechanical resonance frequency, zero-point fluctuation amplitude, and bare optomechanical coupling rate of an hBN drum as a function of drum diameter D_{drum} and thickness d_m. **(b)**: power reflectivity of few-layer hBN as a function of thickness and wavelength. Estimated values for samples HS10 and HS12 are shown as up and down white triangles, respectively. The white dashed curves are isocurves, labeled with their corresponding value.

The estimates for these figures of merit are plotted as a function of the diameter and thickness of the hBN drum in Fig. 5.2, with thickness taken between 0.33 and 330 nm, corresponding to 1 to 1000 layers. The values of material properties were taken from [64], and G was calculated numerically using the coupling matrix method introduced in Section 1.2.2. The highest optomechanical coupling strength is obtained by optimizing for high mechanical frequency, low mass and large reflectivity. The values which correspond to the two samples discussed in this chapter are highlighted with markers. Sample HS10 was fabricated on a commercially available Norcada NH050D2019 micro-porous membrane with 20 µm-diameter holes. Sample HS12 was fabricated on a custom Norcada micro-porous membrane which features high stress (900 MPa) stoichiometric SiN, 30 µm-diameter holes and a smaller window size.

For the second generation HS12 sample, we made an effort to separate the mechanical resonance frequencies of the hBN drum and of the SiN membrane, which we suspect could be overlapping in the case of sample HS10, preventing easy identification and study of the hBN drum modes. To this end we designed and ordered a set of custom holey membranes from Norcada which use high-stress SiN, have smaller window size and have larger holes. As a result the frequency of the SiN membrane modes is expected to increase while the frequency of the hBN drum modes should decrease compared to HS10.

5.1.2 Fabricating and mounting the hBN hybrid mechanical resonator

Here we describe the process through which the devices are fabricated, and how they are mounted in the experimental platform. Since sample fabrication was carried out by David Jaeger and will be described in detail in his upcoming PhD dissertation, only a brief summary is given here. Efforts related to creating single photon emitters in the hBN flakes and localizing them deterministically within the drum are ongoing and will be discussed in David Jaeger's dissertation.

The fabrication process starts with the exfoliation of hBN flakes from bulk hBN crystals[2] onto a Si/SiO2 substrate by the scotch-tape technique. Candidate flakes are identified under an optical microscope, giving preference to large flakes with no visible steps or wrinkles and a thickness between 70 and 100 nm (estimated from the color on SiO2[133]). The substrate is then spin coated with PMMA, the SiO2 layer is etched away in 2M NaOH, leaving a PMMA membrane with hBN flakes attached to it. Using a micromanipulator, a wet transfer technique is then used to precisely position the target hBN flake on top of the central hole of a Norcada holey membrane. The PMMA is finally dissolved in acetone, completing the fabrication process (see Fig. 5.1(b)).

A custom titanium carrier was designed to mount the samples in the experimental platform. The sample is glued to this carrier, which is then attached to the dovetail assembly introduced in Section 4.1.2. The design of the carrier and the sample gluing process (illustrated in Fig. 5.3) take into account previous reports associating contact surface between glue and the sample to a decrease in mechanical Q factor [134, 135]. The cutouts in the carrier minimize the contact points with the sample and prevents the glue from spreading. The gluing process is carried out under an optical microscope with the sample firmly pinned against the titanium carrier by a rounded-point scribe, preventing the glue from flowing under the sample and thus

[2] HQ graphene

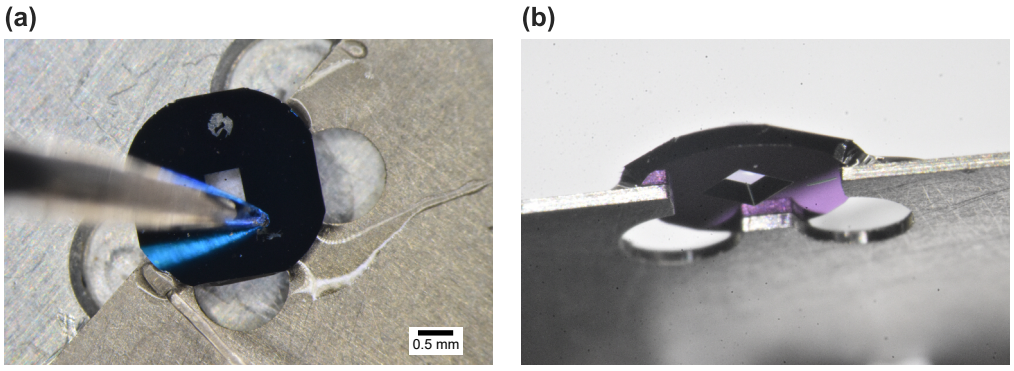

FIGURE 5.3: **(a)**: Norcada holey membrane being glued to the custom titanium carrier. **(b)**: view from below of the resulting assembly.

ensuring the sample rests flat on the carrier. Three small drops of UV glue[3], pre-cured to increase its viscosity, are applied to the corners of the sample in contact with the carrier before being fully cured under UV light. The cross-section of the glue points can be seen in Fig. 5.3(b).

5.2 Optomechanics with an hBN Mechanical Resonator in the Fiber Cavity

In this section we first describe how the hBN mechanical resonator is inserted in the fiber cavity and how the resulting MIM optomechanical system is operated. We then discuss the characterization of the dispersive and dissipative optomechanical coupling in a static measurement. The results presented in this section were obtained using fibers 197 and 262 and sample HS10.

5.2.1 System alignment and sample navigation

In order to form the MIM optomechanical system, the Norcada holey membrane must be inserted in the fiber cavity, its position relative to the two fiber mirrors must be tuned, and the hBN mechanical resonator must be positioned within the cavity mode.

For inserting the membrane within the fiber cavity, we follow a procedure similar to the one described in [58]. Started from an aligned cavity, the fiber mounted on the z stepper is retracted by about 2 mm and the dovetail assembly to which the sample is mounted is inserted into the experimental platform so that the membrane is between the two fiber mirrors. Using a usb microscope, and with the HeNe laser coupled into the cavity input fiber, the membrane is roughly centered laterally on the red laser spot and brought close to the input fiber mirror. Using the white-light interferometry technique described in Section 4.3.3, with the membrane acting as the second mirror, the distance between the input fiber mirror and the membrane is tuned to the desired value, usually about 15 µm. The output fiber mirror can then be brought back in, entering the backside cavity of the Norcada holey membrane. A camera picture of the experimental platform at this step in the process in shown in Fig. 5.5(a).

[3] Norland Optical Adhesive NOA 65

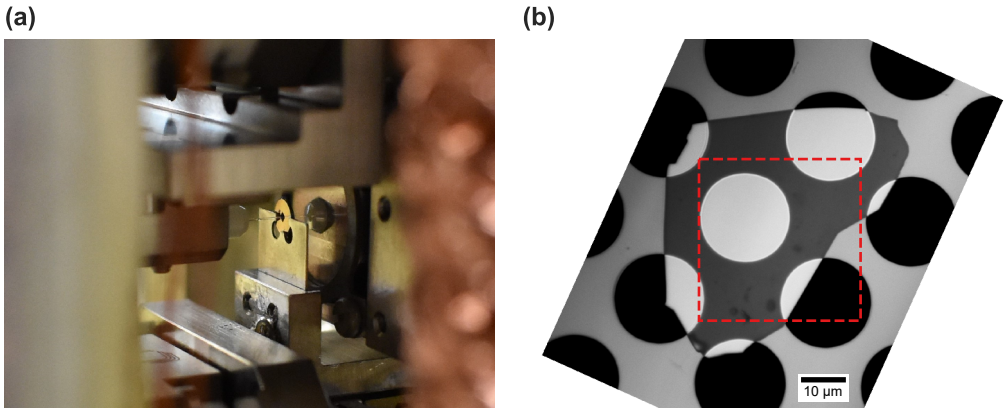

FIGURE 5.4: **(a)**: pre-aligned MIM system. **(b)**: microscope picture of the hBN drum mechanical resonator on sample HS10, rotated and flipped to match membrane scanner maps in Figs. 5.5 and 5.6. The red dashed square corresponds to the scanning area.

With the membrane close to the input fiber mirror and the output fiber mirror close enough, the reflection and transmission of the HeNe laser can be monitored while the lateral position of the membrane is scanned using a combination of stepping with the xy steppers and scanning with the xy scanner. For large scale navigation on the membrane we avoid making maps using both the x and y steppers because repetitively stepping back and worth leads to unwanted behavior [136]; instead, we typically make maps by stepping in x and scanning in y or vice versa. We use this navigation technique to locate the hBN drum resonator, and fine tune the sample position by making xy scanner maps, manually stepping the xy steppers in-between maps. Figure 5.5 shows a membrane scanner map of the transmission and reflection of the HeNe laser. The map area corresponds to the red dashed square in Fig. 5.4(b), and includes a partly empty hole, SiN, hBN on SiN and a full hBN drum, as highlighted in the figure. The interference pattern that appears in the reflective areas is caused by the axes of the scanner not being perfectly perpendicular to the cavity axis.

With the sample map available, we form an empty cavity again by moving to a membrane hole, so that the cavity alignment can be fine-tuned. The cavity length is tuned to the desired value using the white-light interferometry technique.

With the input fiber mirror connected to the laser system, we perform continuous scans of the cavity length and optimize the lateral alignment of the cavity. At this point the distance between the membrane and both fiber mirrors is known, and the cavity is operational. Figure 5.6 shows a membrane scanner map of the resonant cavity transmission and reflection, acquired by performing a cavity scan at each point of the membrane scan and selecting the value of transmission and reflection at resonance. The cavity is undisturbed within the hole, and cavity signal can be found in other areas where clipping losses are small, namely the center of the hBN drum and the center of the hBN/SiN pads. The peak cavity signal in those areas is significantly weaker and displays a complex structure which seems to echo the interferometric pattern found in Fig. 5.5. Even though the fine points of this measurement require more in-depth investigation, Fig. 5.6 shows that a MIM system can be formed around the suspended hBN drum, as well as around the SiN and hBN/SiN areas of the membrane.

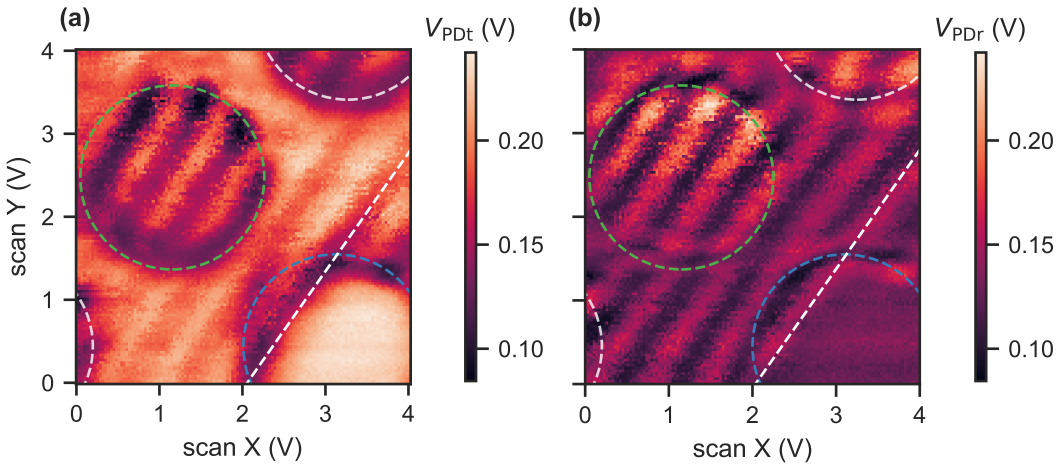

FIGURE 5.5: **(a,b)**: xy sample scanner maps of the reflection and transmission of the HeNe laser. Dashed circles are guides for the eye highlighting holes in the SiN membrane. The green circle corresponds to the hBN drum, the blue circle corresponds to the empty hole. The dashed line white indicates the edge of the hBN flake.

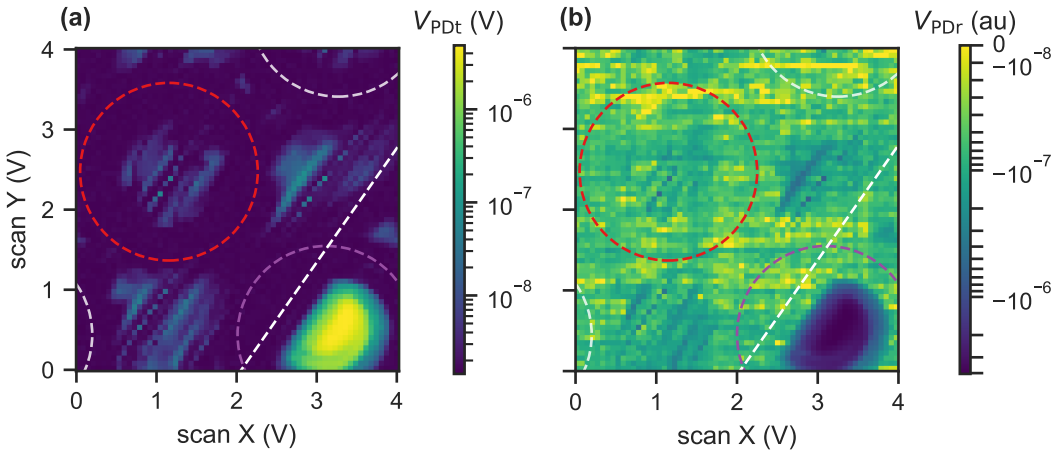

FIGURE 5.6: **(a,b)**: xy sample scanner maps of the reflection and transmission signal of the cavity at resonance. Dashed circles are guides for the eye highlighting holes in the membrane. The red circle corresponds to the hBN drum, the purple circle corresponds to the empty hole. The dashed line is a guide for the eye indicating the edge of the hBN flake.

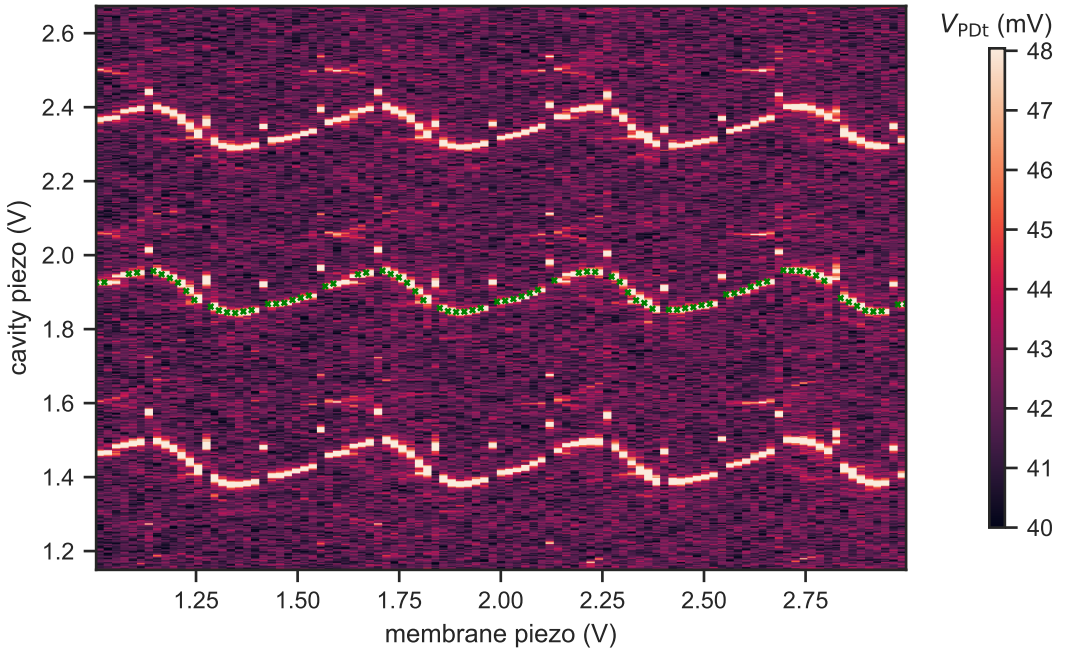

FIGURE 5.7: Resonance spectrum of the MIM system as a function of membrane z position. The green markers correspond to the fundamental resonance which properties are plotted in Fig. 5.8.

5.2.2 Static dispersive and dissipative optomechanical coupling

The dispersive and dissipative optomechanical coupling strength in a MIM system can be characterized statically by measuring the changes in cavity resonance frequency and losses as the position of the membrane within the cavity is varied in the longitudinal direction. Here we present the results of such a measurement, performed with the hBN drum centered laterally within the cavity mode.

The data shown in Fig. 5.7 was acquired with the membrane scanner set to the middle of the red dashed circle in Fig. 5.6, placing the suspended hBN drum in the middle of the fiber cavity. Cavity scans were taken and the voltage sent to the piezo controlling the z position of the membrane was increased between each scan. A subset of the acquired data is plotted in Fig. 5.7, selected to show three consecutive fundamental resonances of the cavity and four periods of the dependence on the position of the membrane, and with each cavity scan gaussian filtered for visual clarity. The position of the fundamental resonance exhibits a significant periodic dependence on the membrane position, which is the signature of dispersive optomechanical coupling. We believe the jumps in the position of the fundamental resonance observed at regularly spaced membrane positions might be due to coupling to higher order modes, which otherwise faintly appear in the data. More in-depth investigations are currently underway.

In order to characterize the dispersive and dissipative optomechanical coupling, the position and linewidth of a fundamental resonance tracked across cavity scans (green markers in Fig. 5.7) are extracted. The variations in resonance position normalized by the FSR are fitted to Eq. (1.91), with $|r_m|$, ϕ_r, and a linear conversion scale for the z_m axis as fit coefficients. The variations in resonance position and in resonance linewidth are then differentiated with respect to z_m to obtain the dispersive effect and the dissipative effect of the membrane position. Figure 5.8 shows

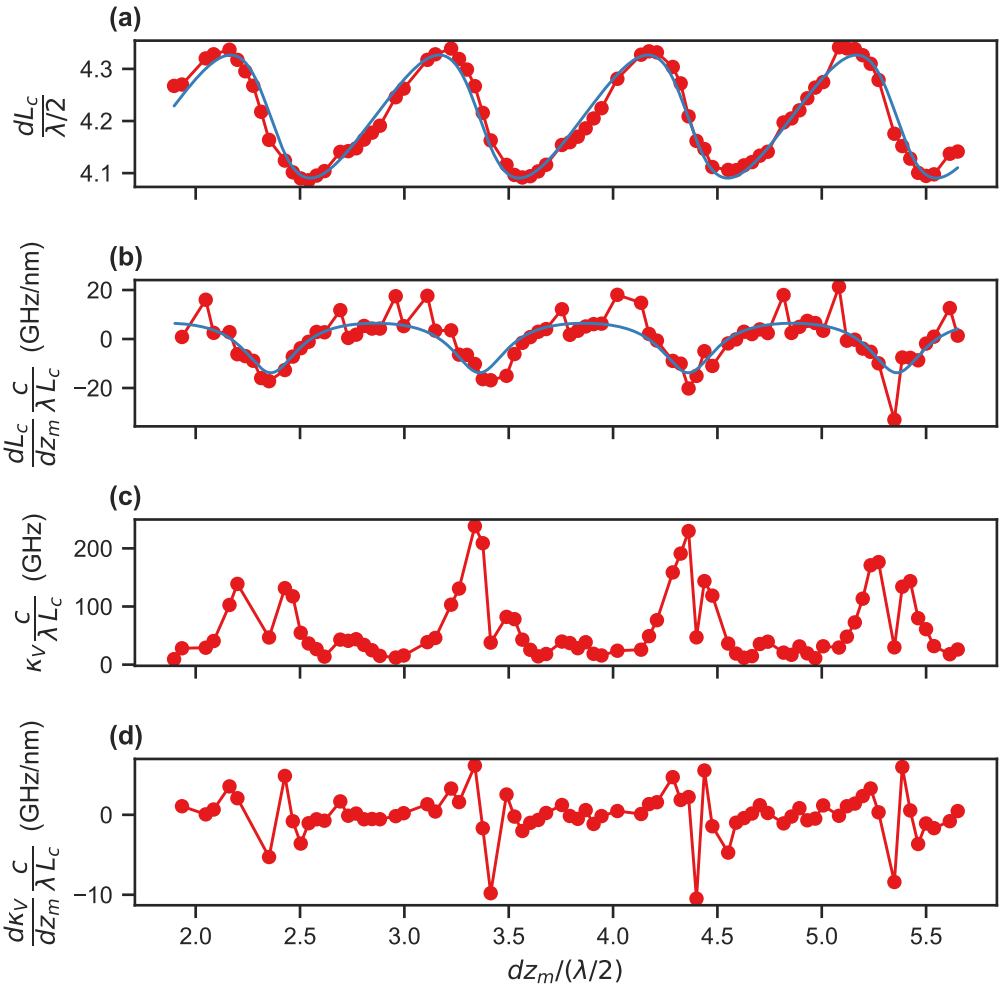

FIGURE 5.8: **(a-d)**: resonant length, dispersive effect, linewidth, and dissipative effect as a function of the membrane position. The blue curve in (a) is the best fit to the data using Eq. (1.91). The blue curve in (b) is the derivative of the blue curve in (a).

the results of this data analysis procedure. The good quality of the fit to Eq. (1.91) displayed in Fig. 5.7(a) confirms that the dispersive behavior of the MIM system matches the theoretical expectations. The fit value for $|r_m|$ is 0.36, significantly lower than the expected value of 0.63 for 70 nm-thick hBN at 920 nm. The large dissipative coupling is unexpected since optical absorption in hBN is vanishingly small, and the two fiber mirrors have identical reflection coefficients. We believe it is due to membrane tilt, leading to part of the light reflected by the membrane being scattered out of the cavity mode. Membrane tilt is likely to be present considering the design of the experimental platform, and would also explain the reduced $|r_m|$, as well as the strong reduction of finesse from the empty cavity finesse (4000 to 400). However, we cannot presently rule out issues with the surface quality of the hBN flake, or contamination of the sample. We are currently planning a modification of the experimental platform in order to allow for the tip and tilt of the sample to be tuned, which will make it possible to investigate the matter further.

The asymmetric behavior of the variations in resonance position is due to the cavity scanning scheme, where only the output fiber mirror is displaced. In contrast, when both mirrors are scanned symmetrically around the membrane, a symmetric

behavior of the variations in resonance position is observed [60]. This effect of the cavity scanning scheme leads to the asymmetry of the dispersive effect around zero observed in Fig. 5.8, which could be interpreted as a boost in the dispersive optomechanical coupling. However, due to the membrane being roughly positioned in the middle of the optical cavity, we expect the variation in resonance frequency to have a symmetric behavior as shown in Fig. 1.10. Because of this discrepancy in cavity resonance condition when expressed in terms of cavity length or in terms of frequency, caution should be exercised when quoting the value for dispersive and dissipative optomechanical coupling from the dispersive and dissipative effects measured by performing cavity scans. This issue is specific to MIM systems and has been treated lightly in recent works. In [85], the membrane is close to the input mirror and the cavity scan is performed using the output mirror, making the measured asymmetric behavior of the variations in resonance position match the expected asymmetric behavior of the resonance frequency. In [60], the membrane is close to the middle of the optical cavity and the cavity scan is performed by scanning the mirrors symmetrically around the membrane, making the measured symmetric behavior of the variations in resonance position match the expected symmetric behavior of the resonance frequency. Potential errors in the conversion between the dispersive effect measured from cavity scans and the dispersive optomechanical coupling $G = d\omega/dz$ have not been discussed. We are currently working on measuring the dispersive and dissipative optomechanical coupling from laser frequency scans, which is more involved experimentally since it requires the cavity length to be actively stabilized.

In order to estimate the dispersive optomechanical coupling, we insert the results of the fit in 1.93 and differentiate with respect to z_m, leading to a maximum dispersive coupling $|G|/(2\pi) = 5.9\,\mathrm{GHz}\cdot\mathrm{nm}^{-1}$. This value is only slightly lower than the predicted value of $9.3\,\mathrm{GHz}\cdot\mathrm{nm}^{-1}$, and we believe the discrepancy to be at least partly explained by sample tilt as discussed previously.

Similar results have been obtained with the MIM system formed around a SiN region.

5.2.3 Dynamical optomechanics

Properties of the MIM system that have yet to be characterized are the frequency and quality factor of the mechanical resonances of the hBN drum resonator and the amplitude of their zero-point fluctuations.

We are currently performing driven response measurements using the shaker piezo to parametrically drive the mechanical resonances of the hBN drum and SiN membrane in order to access those quantities. Once the mechanical frequency of the drum mode is found, we aim to characterize the dynamical optomechanical interaction in the MIM system by measuring the optical spring and damping effects and by performing OMIT measurements.

Conclusion and Outlook

During the present thesis work, we successfully designed, assembled and characterized an experimental platform built around a fiber-based membrane-in-the-middle optomechanical system.

We fabricated fiber mirrors with a geometry optimized for realizing hybrid optomechanical systems in the membrane-in-the-middle configuration [68]. We formed Fabry-Perot cavities between these fiber mirrors, held in a titanium cage that we specially designed for operating the MIM system within a ^{4}He bath cryostat and in high vacuum, while maintaining both a high level of tunability and a high level of mechanical stability. We characterized the optical properties of these fiber cavities extensively, showing that they can be operated in a widely tunable range of cavity lengths (10 to 100 µm), and that they retain their maximum finesse on the order of 10 000 between 10 and 35 µm. At a typical cavity length of 30 µm cavity, we estimate a mode waist on the order of 3 µm and a mode volume on the order of $250\lambda^3$, which compares well to the state-of-the-art system demonstrated in [60]. Furthermore, we were able to stabilize the length of our FFPC cavity to within 5 pm (or 10 % of the cavity linewidth) using the Pound-Drever-Hall technique [69]. The lock has a bandwidth on the order of 10 kHz and remains stable for many hours, both at room temperature and at 4 K, which to the best of our knowledge has not been demonstrated yet in a high finesse tunable fiber Fabry-Perot cavity. State-of-the-art fiber Fabry-Perot cavities are either using a low finesse cavity [58], not operating at cryogenic temperatures [51, 60, 137], not tunable in-situ [137, 138], or unable to maintain the lock for extended periods of time at cryogenic temperatures [138, 139].

The optical properties of our fiber cavities are currently limited by the mirror coating designed for a finesse of 15000, and we believe that the lock bandwidth is limited by the low frequency cantilever mode of the overhanging fiber mirrors. We therefore expect to further improve the optical properties of our system in the near future by fabricating new fiber mirrors and having an ultra-low loss coating deposited onto their tip. This should lead to a reduction in the cavity linewidth from $\kappa/(2\pi) \approx 500$ MHz to 50 MHz. Using larger ferrules to hold the fibers should also avoid the overhang issue.

In parallel to the development of the experimental platform, we fabricated hBN drum micromechanical resonators on SiN holey membranes. We inserted these micromechanical resonators in the middle of the fiber cavity, realizing a functional membrane-in-the-middle optomechanical system in which the membrane can be freely positioned and scanned laterally. We observed the dispersive and dissipative effect of the hBN drum on the resonance of the MIM system. Based on this measurement, we estimate a linear dispersive optomechanical coupling on the order of $6\,\mathrm{GHz}\cdot\mathrm{nm}^{-1}$, which again compares well to [60]. It is however associated with a strong dissipative optomechanical coupling, and a significant reduction of the cavity finesse when the hBN flake is within the cavity. We expect to be able to elucidate the origin of the dissipative coupling by implementing a way to tune the tip and tilt of the membrane within the cavity.

Our immediate next step will be to finalize the acquisition of a clean set of measurements demonstrating the optical properties and the mechanical stability of our fiber cavity platform, which is to be integrated in our upcoming publication [69]. It is interesting to note that, based on the estimated value of the mode waist, we expect to measure a near-perfect mode-matching efficiency to the cavity mode $|\alpha|^2$, limited by the concentricity between the crater defining the mirror and the fiber core.

Our following step will be to observe dynamical optomechanical effects in the MIM system, and in particular to measure its OMIT response. Based on our estimation of the linear dispersive optomechanical coupling with the hBN drum, and using the values from [64] to calculate Ω_m, x_{zpf}, and Γ_m, we predict a single photon optomechanical coupling rate $g_0/(2\pi) \approx 50\,\mathrm{kHz}$ for the fundamental drum resonance at $\Omega_m/(2\pi) \approx 3\,\mathrm{MHz}$. Note that this prediction is based on a very modest mechanical quality factor of 100, which should potentially reach higher values similar to those obtained with graphene [22, 62, 63]. Studying the dynamical optomechanical effects with the hBN drum in our MIM system should provide valuable data on the mechanical properties of hBN, and may help answer some of the open questions about the dynamics of 2D material membranes [66].

The completion of this step will fully demonstrate the viability of our experimental platform as a testbed for hybrid optomechanical system. Once we succeed in deterministically localizing single photon emitters within the hBN drum, we will measure the impact of a quantum emitter positioned within the hBN drum on its OM interaction with the cavity field [34, 140, 141].

Finally, we believe that due to its high sensitivity and its versatility, the experimental platform introduced here is suitable for studying a very broad array of nanomechanical resonators such as for example : silicon carbide nanowires [21], nanowires with embedded emitters [46], carbon nanotubes [20], magnetic 2D materials [142], or functionalized membranes [143].

Bibliography

[1] M. Aspelmeyer, T. J. Kippenberg, and F. Marquardt. "Cavity Optomechanics". In: *Reviews of Modern Physics* 86.4 (Dec. 30, 2014), pp. 1391–1452. DOI: 10.1103/RevModPhys.86.1391 (cit. on pp. 1, 20, 23).

[2] M. Poot and H. S. J. van der Zant. "Mechanical Systems in the Quantum Regime". In: *Physics Reports*. Mechanical Systems in the Quantum Regime 511.5 (Feb. 2012), pp. 273–335. DOI: 10.1016/j.physrep.2011.12.004 (cit. on p. 1).

[3] W. P. Bowen and G. J. Milburn. *Quantum Optomechanics*. Taylor & Francis, Nov. 12, 2015. 381 pp. (cit. on p. 1).

[4] J. D. Teufel, T. Donner, D. Li, J. W. Harlow, M. S. Allman, K. Cicak, A. J. Sirois, J. D. Whittaker, K. W. Lehnert, and R. W. Simmonds. "Sideband Cooling of Micromechanical Motion to the Quantum Ground State". In: *Nature* 475.7356 (July 21, 2011), pp. 359–363. DOI: 10.1038/nature10261 (cit. on p. 1).

[5] J. Chan, T. P. M. Alegre, A. H. Safavi-Naeini, J. T. Hill, A. Krause, S. Gröblacher, M. Aspelmeyer, and O. Painter. "Laser Cooling of a Nanomechanical Oscillator into Its Quantum Ground State". In: *Nature* 478.7367 (Oct. 6, 2011), pp. 89–92. DOI: 10.1038/nature10461 (cit. on p. 1).

[6] G. Anetsberger, O. Arcizet, Q. P. Unterreithmeier, R. Rivière, A. Schliesser, E. M. Weig, J. P. Kotthaus, and T. J. Kippenberg. "Near-Field Cavity Optomechanics with Nanomechanical Oscillators". In: *Nature Physics* 5.12 (12 Dec. 2009), pp. 909–914. DOI: 10.1038/nphys1425 (cit. on p. 1).

[7] A. Schliesser, O. Arcizet, R. Rivière, G. Anetsberger, and T. J. Kippenberg. "Resolved-Sideband Cooling and Position Measurement of a Micromechanical Oscillator Close to the Heisenberg Uncertainty Limit". In: *Nature Physics* 5.7 (July 2009), pp. 509–514. DOI: 10.1038/nphys1304 (cit. on p. 1).

[8] J. D. Teufel, T. Donner, M. A. Castellanos-Beltran, J. W. Harlow, and K. W. Lehnert. "Nanomechanical Motion Measured with an Imprecision below That at the Standard Quantum Limit". In: *Nature Nanotechnology* 4.12 (12 Dec. 2009), pp. 820–823. DOI: 10.1038/nnano.2009.343 (cit. on p. 1).

[9] M. Aspelmeyer. *Cavity Optomechanics : Nano- and Micromechanical Resonators Interacting with Light*. In collab. with F. Marquardt and T. J. Kippenberg. Quantum Science and Technology. Berlin, Heidelberg: Springer Berlin Heidelberg, 2014. viii+357 (cit. on p. 1).

[10] J. D. Thompson, B. M. Zwickl, A. M. Jayich, F. Marquardt, S. M. Girvin, and J. G. E. Harris. "Strong Dispersive Coupling of a High-Finesse Cavity to a Micromechanical Membrane". In: *Nature* 452.7183 (Mar. 6, 2008), pp. 72–75. DOI: 10.1038/nature06715 (cit. on p. 1).

[11] T. P. Purdy, R. W. Peterson, and C. A. Regal. "Observation of Radiation Pressure Shot Noise on a Macroscopic Object". In: *Science* 339.6121 (Feb. 15, 2013), pp. 801–804. DOI: 10.1126/science.1231282 (cit. on p. 1).

[12] M. Underwood, D. Mason, D. Lee, H. Xu, L. Jiang, A. B. Shkarin, K. Børkje, S. M. Girvin, and J. G. E. Harris. "Measurement of the Motional Sidebands of a Nanogram-Scale Oscillator in the Quantum Regime". In: *Physical Review A* 92.6 (Dec. 2, 2015), p. 061801. DOI: 10.1103/PhysRevA.92.061801 (cit. on p. 1).

[13] R. W. Peterson, T. P. Purdy, N. S. Kampel, R. W. Andrews, P.-L. Yu, K. W. Lehnert, and C. A. Regal. "Laser Cooling of a Micromechanical Membrane to the Quantum Backaction Limit". In: *Physical Review Letters* 116.6 (Feb. 8, 2016), p. 063601. DOI: 10.1103/PhysRevLett.116.063601 (cit. on p. 1).

[14] W. H. P. Nielsen, Y. Tsaturyan, C. B. Møller, E. S. Polzik, and A. Schliesser. "Multimode Optomechanical System in the Quantum Regime". In: *Proceedings of the National Academy of Sciences* 114.1 (Jan. 3, 2017), pp. 62–66. DOI: 10.1073/pnas.1608412114 (cit. on p. 1).

[15] M. Rossi, D. Mason, J. Chen, Y. Tsaturyan, and A. Schliesser. "Measurement-Based Quantum Control of Mechanical Motion". In: *Nature* 563.7729 (Nov. 2018), pp. 53–58. DOI: 10.1038/s41586-018-0643-8 (cit. on p. 1).

[16] D. Mason, J. Chen, M. Rossi, Y. Tsaturyan, and A. Schliesser. "Continuous Force and Displacement Measurement below the Standard Quantum Limit". In: *Nature Physics* 15.8 (Aug. 2019), pp. 745–749. DOI: 10.1038/s41567-019-0533-5 (cit. on p. 1).

[17] Y. Tsaturyan, A. Barg, E. S. Polzik, and A. Schliesser. "Ultracoherent Nanomechanical Resonators via Soft Clamping and Dissipation Dilution". In: *Nature Nanotechnology* advance online publication.8 (June 12, 2017). DOI: 10.1038/nnano.2017.101 (cit. on p. 1).

[18] Y. Tsaturyan. "Ultracoherent Soft-Clamped Mechanical Resonators for Quantum Cavity Optomechanics". PhD thesis. University of Copenhagen, Faculty of Science, Niels Bohr Institute, Danish Center for Quantum Optics, 2019 (cit. on pp. 1, 25).

[19] S. Bernard, C. Reinhardt, V. Dumont, Y.-A. Peter, and J. C. Sankey. "Precision Resonance Tuning and Design of SiN Photonic Crystal Reflectors". In: *Optics Letters* 41.24 (Dec. 15, 2016), pp. 5624–5627. DOI: 10.1364/OL.41.005624 (cit. on p. 1).

[20] S. Stapfner, L. Ost, D. Hunger, J. Reichel, I. Favero, and E. M. Weig. "Cavity-Enhanced Optical Detection of Carbon Nanotube Brownian Motion". In: *Applied Physics Letters* 102.15 (Apr. 15, 2013), p. 151910. DOI: 10.1063/1.4802746 (cit. on pp. 1, 2, 42, 88).

[21] F. Fogliano, B. Besga, A. Reigue, P. Heringlake, L. Mercier de Lépinay, C. Vaneph, J. Reichel, B. Pigeau, and O. Arcizet. "Mapping the Cavity Optomechanical Interaction with Subwavelength-Sized Ultrasensitive Nanomechanical Force Sensors". In: *Physical Review X* 11.2 (Apr. 8, 2021), p. 021009. DOI: 10.1103/PhysRevX.11.021009 (cit. on pp. 1, 2, 42, 88).

[22] P. K. Shandilya, J. E. Fröch, M. Mitchell, D. P. Lake, S. Kim, M. Toth, B. Behera, C. Healey, I. Aharonovich, and P. E. Barclay. "Hexagonal Boron Nitride Cavity Optomechanics". In: *Nano Letters* 19.2 (Feb. 13, 2019), pp. 1343–1350. DOI: 10.1021/acs.nanolett.8b04956 (cit. on pp. 1, 2, 77, 88).

[23] K. Børkje, A. Nunnenkamp, J. D. Teufel, and S. M. Girvin. "Signatures of Nonlinear Cavity Optomechanics in the Weak Coupling Regime". In: *Physical Review Letters* 111.5 (Aug. 2, 2013), p. 053603. DOI: 10.1103/PhysRevLett.111.053603 (cit. on p. 1).

[24] M.-A. Lemonde, N. Didier, and A. A. Clerk. "Nonlinear Interaction Effects in a Strongly Driven Optomechanical Cavity". In: *Physical Review Letters* 111.5 (Aug. 2, 2013), p. 053602. DOI: 10.1103/PhysRevLett.111.053602 (cit. on p. 1).

[25] A. Nunnenkamp, K. Børkje, and S. M. Girvin. "Single-Photon Optomechanics". In: *Physical Review Letters* 107.6 (Aug. 3, 2011), p. 063602. DOI: 10.1103/PhysRevLett.107.063602 (cit. on p. 1).

[26] P. Rabl. "Photon Blockade Effect in Optomechanical Systems". In: *Physical Review Letters* 107.6 (Aug. 3, 2011), p. 063601. DOI: 10.1103/PhysRevLett.107.063601 (cit. on p. 1).

[27] A. D. O'Connell et al. "Quantum Ground State and Single-Phonon Control of a Mechanical Resonator". In: *Nature* 464.7289 (Apr. 1, 2010), pp. 697–703. DOI: 10.1038/nature08967 (cit. on p. 1).

[28] P. Treutlein, C. Genes, K. Hammerer, M. Poggio, and P. Rabl. "Hybrid Mechanical Systems". In: *Cavity Optomechanics*. Quantum Science and Technology. Springer, Berlin, Heidelberg, 2014, pp. 327–351. DOI: 10.1007/978-3-642-55312-7_14 (cit. on p. 1).

[29] M. Wallquist, K. Hammerer, P. Zoller, C. Genes, M. Ludwig, F. Marquardt, P. Treutlein, J. Ye, and H. J. Kimble. "Single-Atom Cavity QED and Optomicromechanics". In: *Physical Review A* 81.2 (Feb. 18, 2010), p. 023816. DOI: 10.1103/PhysRevA.81.023816 (cit. on p. 1).

[30] I. Wilson-Rae, C. Galland, W. Zwerger, and A. Imamoğlu. "Exciton-Assisted Optomechanics with Suspended Carbon Nanotubes". In: *New Journal of Physics* 14.11 (2012), p. 115003. DOI: 10.1088/1367-2630/14/11/115003 (cit. on p. 1).

[31] T. Ramos, V. Sudhir, K. Stannigel, P. Zoller, and T. J. Kippenberg. "Nonlinear Quantum Optomechanics via Individual Intrinsic Two-Level Defects". In: *Physical Review Letters* 110.19 (May 9, 2013), p. 193602. DOI: 10.1103/PhysRevLett.110.193602 (cit. on p. 1).

[32] J. Restrepo, C. Ciuti, and I. Favero. "Single-Polariton Optomechanics". In: *Physical Review Letters* 112.1 (Jan. 3, 2014), p. 013601. DOI: 10.1103/PhysRevLett.112.013601 (cit. on p. 1).

[33] O. Kyriienko, T. C. H. Liew, and I. A. Shelykh. "Optomechanics with Cavity Polaritons: Dissipative Coupling and Unconventional Bistability". In: *Physical Review Letters* 112.7 (Feb. 19, 2014), p. 076402. DOI: 10.1103/PhysRevLett.112.076402 (cit. on p. 1).

[34] J.-M. Pirkkalainen, S. U. Cho, F. Massel, J. Tuorila, T. T. Heikkilä, P. J. Hakonen, and M. A. Sillanpää. "Cavity Optomechanics Mediated by a Quantum Two-Level System". In: *Nature Communications* 6 (Apr. 27, 2015), p. 6981. DOI: 10.1038/ncomms7981 (cit. on pp. 1, 2, 88).

[35] M. Abdi, M. Pernpeintner, R. Gross, H. Huebl, and M. J. Hartmann. "Quantum State Engineering with Circuit Electromechanical Three-Body Interactions". In: *Physical Review Letters* 114.17 (Apr. 28, 2015), p. 173602. DOI: 10.1103/PhysRevLett.114.173602 (cit. on p. 1).

[36] B. Sarma and A. K. Sarma. "Ground-State Cooling of Micromechanical Oscillators in the Unresolved-Sideband Regime Induced by a Quantum Well". In: *Physical Review A* 93.3 (Mar. 24, 2016), p. 033845. DOI: 10.1103/PhysRevA.93.033845 (cit. on p. 1).

[37] M. Wallquist, K. Hammerer, P. Rabl, M. Lukin, and P. Zoller. "Hybrid Quantum Devices and Quantum Engineering". In: *Physica Scripta* 2009.T137 (Dec. 1, 2009), p. 014001. DOI: 10.1088/0031-8949/2009/T137/014001 (cit. on p. 2).

[38] K. Stannigel, P. Rabl, A. S. Sørensen, M. D. Lukin, and P. Zoller. "Optomechanical Transducers for Quantum-Information Processing". In: *Physical Review A* 84.4 (Oct. 31, 2011), p. 042341. DOI: 10.1103/PhysRevA.84.042341 (cit. on p. 2).

[39] J. Košata, O. Zilberberg, C. L. Degen, R. Chitra, and A. Eichler. "Spin Detection via Parametric Frequency Conversion in a Membrane Resonator". In: *Physical Review Applied* 14.1 (July 15, 2020), p. 014042. DOI: 10.1103/PhysRevApplied.14.014042 (cit. on p. 2).

[40] R. Fischer, D. P. McNally, C. Reetz, G. G. T. Assumpção, T. Knief, Y. Lin, and C. A. Regal. "Spin Detection with a Micromechanical Trampoline: Towards Magnetic Resonance Microscopy Harnessing Cavity Optomechanics". In: *New Journal of Physics* 21.4 (Apr. 2019), p. 043049. DOI: 10.1088/1367-2630/ab117a (cit. on p. 2).

[41] D. Hunger, T. Steinmetz, Y. Colombe, C. Deutsch, T. W. Hänsch, and J. Reichel. "A Fiber Fabry–Perot Cavity with High Finesse". In: *New Journal of Physics* 12.6 (2010), p. 065038. DOI: 10.1088/1367-2630/12/6/065038 (cit. on pp. 2, 14, 16, 18, 27, 30, 39, 43).

[42] A. Muller, E. B. Flagg, J. R. Lawall, and G. S. Solomon. "Ultrahigh-Finesse, Low-Mode-Volume Fabry–Perot Microcavity". In: *Optics Letters* 35.13 (July 1, 2010), pp. 2293–2295. DOI: 10.1364/OL.35.002293 (cit. on pp. 2, 27).

[43] L. Greuter, S. Starosielec, D. Najer, A. Ludwig, L. Duempelmann, D. Rohner, and R. J. Warburton. "A Small Mode Volume Tunable Microcavity: Development and Characterization". In: *Applied Physics Letters* 105.12 (Sept. 22, 2014), p. 121105. DOI: 10.1063/1.4896415 (cit. on pp. 2, 40, 42).

[44] D. Riedel, S. Flågan, P. Maletinsky, and R. J. Warburton. "Cavity-Enhanced Raman Scattering for In Situ Alignment and Characterization of Solid-State Microcavities". In: *Physical Review Applied* 13.1 (Jan. 22, 2020), p. 014036. DOI: 10.1103/PhysRevApplied.13.014036 (cit. on p. 2).

[45] Y. Colombe, T. Steinmetz, G. Dubois, F. Linke, D. Hunger, and J. Reichel. "Strong Atom–Field Coupling for Bose–Einstein Condensates in an Optical Cavity on a Chip". In: *Nature* 450.7167 (Nov. 2007), pp. 272–276. DOI: 10.1038/nature06331 (cit. on pp. 2, 42).

[46] A. Muller, E. B. Flagg, M. Metcalfe, J. Lawall, and G. S. Solomon. "Coupling an Epitaxial Quantum Dot to a Fiber-Based External-Mirror Microcavity". In: *Applied Physics Letters* 95.17 (Oct. 26, 2009), p. 173101. DOI: 10.1063/1.3245311 (cit. on pp. 2, 42, 88).

[47] C. Toninelli, Y. Delley, T. Stöferle, A. Renn, S. Götzinger, and V. Sandoghdar. "A Scanning Microcavity for in Situ Control of Single-Molecule Emission". In: *Applied Physics Letters* 97.2 (July 12, 2010), p. 021107. DOI: 10.1063/1.3456559 (cit. on pp. 2, 42).

[48] M. Steiner, H. M. Meyer, C. Deutsch, J. Reichel, and M. Köhl. "Single Ion Coupled to an Optical Fiber Cavity". In: *Physical Review Letters* 110.4 (Jan. 25, 2013), p. 043003. DOI: 10.1103/PhysRevLett.110.043003 (cit. on pp. 2, 42).

[49] J. Miguel-Sánchez, A. Reinhard, E. Togan, T. Volz, A. Imamoglu, B. Besga, Jakob Reichel, and J. Estève. "Cavity Quantum Electrodynamics with Charge-Controlled Quantum Dots Coupled to a Fiber Fabry–Perot Cavity". In: *New Journal of Physics* 15.4 (2013), p. 045002. DOI: 10.1088/1367-2630/15/4/045002 (cit. on pp. 2, 42).

[50] R. Albrecht, A. Bommer, C. Deutsch, J. Reichel, and C. Becher. "Coupling of a Single Nitrogen-Vacancy Center in Diamond to a Fiber-Based Microcavity". In: *Physical Review Letters* 110.24 (June 12, 2013), p. 243602. DOI: 10.1103/PhysRevLett.110.243602 (cit. on pp. 2, 42).

[51] B. Brandstätter et al. "Integrated Fiber-Mirror Ion Trap for Strong Ion-Cavity Coupling". In: *Review of Scientific Instruments* 84.12 (Dec. 1, 2013), p. 123104. DOI: 10.1063/1.4838696 (cit. on pp. 2, 42, 87).

[52] B. Besga, C. Vaneph, J. Reichel, J. Estève, A. Reinhard, J. Miguel-Sánchez, A. Imamoğlu, and T. Volz. "Polariton Boxes in a Tunable Fiber Cavity". In: *Physical Review Applied* 3.1 (Jan. 28, 2015), p. 014008. DOI: 10.1103/PhysRevApplied.3.014008 (cit. on pp. 2, 42).

[53] J. Benedikter, H. Kaupp, T. Hümmer, Y. Liang, A. Bommer, C. Becher, A. Krueger, J. M. Smith, T. W. Hänsch, and D. Hunger. "Cavity-Enhanced Single-Photon Source Based on the Silicon-Vacancy Center in Diamond". In: *Physical Review Applied* 7.2 (Feb. 28, 2017), p. 024031. DOI: 10.1103/PhysRevApplied.7.024031 (cit. on pp. 2, 40).

[54] J. Gallego, W. Alt, T. Macha, M. Martinez-Dorantes, D. Pandey, and D. Meschede. "Strong Purcell Effect on a Neutral Atom Trapped in an Open Fiber Cavity". In: *Physical Review Letters* 121.17 (Oct. 23, 2018), p. 173603. DOI: 10.1103/PhysRevLett.121.173603 (cit. on pp. 2, 39, 42).

[55] H. Takahashi, E. Kassa, C. Christoforou, and M. Keller. "Strong Coupling of a Single Ion to an Optical Cavity". In: *Physical Review Letters* 124.1 (Jan. 2, 2020), p. 013602. DOI: 10.1103/PhysRevLett.124.013602 (cit. on pp. 2, 39, 42).

[56] I. Favero, S. Stapfner, D. Hunger, P. Paulitschke, J. Reichel, H. Lorenz, E. M. Weig, and K. Karrai. "Fluctuating Nanomechanical System in a High Finesse Optical Microcavity". In: *Optics Express* 17.15 (July 20, 2009), pp. 12813–12820. DOI: 10.1364/OE.17.012813 (cit. on pp. 2, 42).

[57] N. E. Flowers-Jacobs, S. W. Hoch, J. C. Sankey, A. Kashkanova, A. M. Jayich, C. Deutsch, J. Reichel, and J. G. E. Harris. "Fiber-Cavity-Based Optomechanical Device". In: *Applied Physics Letters* 101.22 (Nov. 26, 2012), p. 221109. DOI: 10.1063/1.4768779 (cit. on pp. 2, 42).

[58] H. Zhong et al. "A Millikelvin All-Fiber Cavity Optomechanical Apparatus for Merging with Ultra-Cold Atoms in a Hybrid Quantum System". In: *Review of Scientific Instruments* 88.2 (Feb. 1, 2017), p. 023115. DOI: 10.1063/1.4976497 (cit. on pp. 2, 42, 80, 87).

[59] A. B. Shkarin, A. D. Kashkanova, C. D. Brown, S. Garcia, K. Ott, J. Reichel, and J. G. E. Harris. "Quantum Optomechanics in a Liquid". In: *Physical Review Letters* 122.15 (Apr. 15, 2019), p. 153601. DOI: 10.1103/PhysRevLett.122.153601 (cit. on pp. 2, 40, 42).

[60] F. Rochau, I. Sánchez Arribas, A. Brieussel, S. Stapfner, D. Hunger, and E. M. Weig. "Dynamical Backaction in an Ultrahigh-Finesse Fiber-Based Microcavity". In: *Physical Review Applied* 16.1 (July 7, 2021), p. 014013. DOI: 10.1103/PhysRevApplied.16.014013 (cit. on pp. 2, 25, 42, 61, 85, 87).

[61] T. T. Tran, K. Bray, M. J. Ford, M. Toth, and I. Aharonovich. "Quantum Emission from Hexagonal Boron Nitride Monolayers". In: *Nature Nanotechnology* 11.1 (Jan. 2016), pp. 37–41. DOI: 10.1038/nnano.2015.242 (cit. on pp. 2, 77).

[62] A. Castellanos-Gomez, V. Singh, H. S. J. van der Zant, and G. A. Steele. "Mechanics of Freely-Suspended Ultrathin Layered Materials". In: *Annalen der Physik* 527.1-2 (Jan. 1, 2015), pp. 27–44. DOI: 10.1002/andp.201400153 (cit. on pp. 2, 88).

[63] A. Falin et al. "Mechanical Properties of Atomically Thin Boron Nitride and the Role of Interlayer Interactions". In: *Nature Communications* 8.1 (June 22, 2017), p. 15815. DOI: 10.1038/ncomms15815 (cit. on pp. 2, 88).

[64] X.-Q. Zheng, J. Lee, and P. X.-L. Feng. "Hexagonal Boron Nitride Nanomechanical Resonators with Spatially Visualized Motion". In: *Microsystems & Nanoengineering* 3.1 (July 31, 2017). DOI: 10.1038/micronano.2017.38 (cit. on pp. 2, 19, 79, 88).

[65] M. Abdi, M.-J. Hwang, M. Aghtar, and M. B. Plenio. "Spin-Mechanical Scheme with Color Centers in Hexagonal Boron Nitride Membranes". In: *Physical Review Letters* 119.23 (Dec. 5, 2017), p. 233602. DOI: 10.1103/PhysRevLett.119.233602 (cit. on pp. 2, 77).

[66] P. G. Steeneken, R. J. Dolleman, D. Davidovikj, F. Alijani, and H. S. J. van der Zant. *Dynamics of 2D Material Membranes*. Aug. 2021. DOI: 10.1088/2053-1583/ac152c. URL: https://doi.org/10.1088/2053-1583/ac152c (cit. on pp. 2, 88).

[67] D. Hunger, C. Deutsch, R. J. Barbour, R. J. Warburton, and J. Reichel. "Laser Micro-Fabrication of Concave, Low-Roughness Features in Silica". In: *AIP Advances* 2.1 (Mar. 1, 2012), p. 012119. DOI: 10.1063/1.3679721 (cit. on pp. 3, 27, 30, 39, 40).

[68] T. Ruelle, M. Poggio, and F. Braakman. "Optimized Single-Shot Laser Ablation of Concave Mirror Templates on Optical Fibers". In: *Applied Optics* 58.14 (May 10, 2019), pp. 3784–3789. DOI: 10.1364/AO.58.003784 (cit. on pp. 3, 27, 87).

[69] T. Ruelle, D. Jaeger, F. Fogliano, F. Braakman, and M. Poggio. "A tunable fiber Fabry–Perot cavity for hybrid optomechanics stabilized at 4 K". In: *Review of Scientific Instruments* 93.9 (2022), p. 095003. DOI: 10.1063/5.0098140 (cit. on pp. 3, 51, 87, 88).

[70] A. E. Siegman. *Lasers*. University Science Books, Jan. 1986. 1322 pp. (cit. on p. 5).

[71] C. Bond, D. Brown, A. Freise, and K. A. Strain. "Interferometer Techniques for Gravitational-Wave Detection". In: *Living Reviews in Relativity* 19.1 (Dec. 1, 2016), p. 3. DOI: 10.1007/s41114-016-0002-8 (cit. on pp. 5, 14).

[72] R. W. P. Drever, J. L. Hall, F. V. Kowalski, J. Hough, G. M. Ford, A. J. Munley, and H. Ward. "Laser Phase and Frequency Stabilization Using an Optical Resonator". In: *Applied Physics B* 31.2 (June 1, 1983), pp. 97–105. DOI: 10.1007/BF00702605 (cit. on p. 9).

[73] E. D. Black. "An Introduction to Pound–Drever–Hall Laser Frequency Stabilization". In: *American Journal of Physics* 69.1 (Dec. 15, 2000), pp. 79–87. DOI: 10.1119/1.1286663 (cit. on p. 9).

[74] C. Reinhardt, T. Müller, and J. C. Sankey. "Simple Delay-Limited Sideband Locking with Heterodyne Readout". In: *Optics Express* 25.2 (Jan. 23, 2017), pp. 1582–1597. DOI: 10.1364/OE.25.001582 (cit. on pp. 10, 74).

[75] J. Benedikter, T. Hümmer, M. Mader, B. Schlederer, J. Reichel, T. W. Hänsch, and D. Hunger. "Transverse-Mode Coupling and Diffraction Loss in Tunable Fabry–Pérot Microcavities". In: *New Journal of Physics* 17.5 (2015), p. 053051. DOI: 10.1088/1367-2630/17/5/053051 (cit. on pp. 12, 14, 17, 18, 42, 61, 67).

[76] W. B. Joyce and B. C. DeLoach. "Alignment of Gaussian Beams". In: *Applied Optics* 23.23 (Dec. 1, 1984), p. 4187. DOI: 10.1364/AO.23.004187 (cit. on pp. 12, 16).

[77] H. Kogelnik. "Coupling and Conversion Coefficients for Optical Modes". In: (June 1, 1964), p. 333 (cit. on p. 12).

[78] J. Gallego, S. Ghosh, S. K. Alavi, W. Alt, M. Martinez-Dorantes, D. Meschede, and L. Ratschbacher. "High-Finesse Fiber Fabry–Perot Cavities: Stabilization and Mode Matching Analysis". In: *Applied Physics B* 122.3 (Mar. 1, 2016), pp. 1–14. DOI: 10.1007/s00340-015-6281-z (cit. on pp. 12, 15–17, 56, 61).

[79] H. Kogelnik and T. Li. "Laser Beams and Resonators". In: *Proceedings of the IEEE* 54.10 (Oct. 1966), pp. 1312–1329. DOI: 10.1109/PROC.1966.5119 (cit. on pp. 13, 18).

[80] D. Kleckner, W. T. M. Irvine, S. S. R. Oemrawsingh, and D. Bouwmeester. "Diffraction-Limited High-Finesse Optical Cavities". In: *Physical Review A* 81.4 (Apr. 15, 2010), p. 043814. DOI: 10.1103/PhysRevA.81.043814 (cit. on pp. 17, 67).

[81] H. Suzuki, N. Yamaguchi, and H. Izumi. "Theoretical and Experimental Studies on the Resonance Frequencies of a Stretched Circular Plate: Application to Japanese Drum Diaphragms". In: *Acoustical Science and Technology* 30.5 (2009), pp. 348–354. DOI: 10.1250/ast.30.348 (cit. on p. 19).

[82] S. Schmid, L. G. Villanueva, and M. L. Roukes. *Fundamentals of Nanomechanical Resonators*. Springer, June 21, 2016. 183 pp. (cit. on p. 20).

[83] I. Favero, J. Sankey, and E. M. Weig. "Mechanical Resonators in the Middle of an Optical Cavity". In: *Cavity Optomechanics*. Quantum Science and Technology. Springer, Berlin, Heidelberg, 2014, pp. 83–119. DOI: 10.1007/978-3-642-55312-7_5 (cit. on pp. 20, 23).

[84] A. M. Jayich, J. C. Sankey, B. M. Zwickl, C. Yang, J. D. Thompson, S. M. Girvin, A. A. Clerk, F. Marquardt, and J. G. E. Harris. "Dispersive Optomechanics: A Membrane inside a Cavity". In: *New Journal of Physics* 10.9 (2008), p. 095008. DOI: 10.1088/1367-2630/10/9/095008 (cit. on pp. 20, 21).

[85] V. Dumont, S. Bernard, C. Reinhardt, A. Kato, M. Ruf, and J. C. Sankey. "Flexure-Tuned Membrane-at-the-Edge Optomechanical System". In: *Optics Express* 27.18 (Sept. 2, 2019), pp. 25731–25748. DOI: 10.1364/OE.27.025731 (cit. on pp. 21, 85).

[86] C. Biancofiore, M. Karuza, M. Galassi, R. Natali, P. Tombesi, G. Di Giuseppe, and D. Vitali. "Quantum Dynamics of an Optical Cavity Coupled to a Thin Semitransparent Membrane: Effect of Membrane Absorption". In: *Physical Review A* 84.3 (Sept. 12, 2011), p. 033814. DOI: 10.1103/PhysRevA.84.033814 (cit. on pp. 23, 25).

[87] J. C. Sankey, A. M. Jayich, B. M. Zwickl, C. Yang, and J. G. E. Harris. "Improved "Position Squared" Readout Using Degenerate Cavity Modes". In: *Pushing the Frontiers of Atomic Physics*. WORLD SCIENTIFIC, Mar. 1, 2009, pp. 131–149. DOI: 10.1142/9789814273008_0014 (cit. on p. 23).

[88] M. Karuza, M. Galassi, C. Biancofiore, C. Molinelli, R. Natali, P. Tombesi, G. D. Giuseppe, and D. Vitali. "Tunable Linear and Quadratic Optomechanical Coupling for a Tilted Membrane within an Optical Cavity: Theory and Experiment". In: *Journal of Optics* 15.2 (2013), p. 025704. DOI: 10.1088/2040-8978/15/2/025704 (cit. on p. 23).

[89] T. Bodiya, V. Sudhir, C. Wipf, N. Smith, A. Buikema, A. Kontos, H. Yu, and N. Mavalvala. "Sub-Hertz Optomechanically Induced Transparency with a Kilogram-Scale Mechanical Oscillator". In: *Physical Review A* 100.1 (July 29, 2019), p. 013853. DOI: 10.1103/PhysRevA.100.013853 (cit. on p. 24).

[90] V. B. Braginskiĭ and A. B. Manukin. "Ponderomotive Effects of Electromagnetic Radiation". In: *Soviet Journal of Experimental and Theoretical Physics* 25 (Oct. 1, 1967), p. 653 (cit. on p. 25).

[91] A. A. Clerk and F. Marquardt. "Basic Theory of Cavity Optomechanics". In: *Cavity Optomechanics*. Quantum Science and Technology. Springer, Berlin, Heidelberg, 2014, pp. 5–23. DOI: 10.1007/978-3-642-55312-7_2 (cit. on p. 25).

[92] A. Schließer. "Cavity Optomechanics and Optical Frequency Comb Generation with Silica Whispering-Gallery-Mode Microresonators". PhD thesis. Ludwig-Maximilians-Universität München, Oct. 21, 2009 (cit. on p. 25).

[93] S. Weis, R. Rivière, S. Deléglise, E. Gavartin, O. Arcizet, A. Schliesser, and T. J. Kippenberg. "Optomechanically Induced Transparency". In: *Science* 330.6010 (Dec. 10, 2010), pp. 1520–1523. DOI: 10.1126/science.1195596 (cit. on p. 25).

[94] A. H. Safavi-Naeini, T. P. M. Alegre, J. Chan, M. Eichenfield, M. Winger, Q. Lin, J. T. Hill, D. E. Chang, and O. Painter. "Electromagnetically Induced Transparency and Slow Light with Optomechanics". In: *Nature* 472.7341 (Apr. 7, 2011), pp. 69–73. DOI: 10.1038/nature09933 (cit. on p. 25).

[95] J. D. Teufel, D. Li, M. S. Allman, K. Cicak, A. J. Sirois, J. D. Whittaker, and R. W. Simmonds. "Circuit Cavity Electromechanics in the Strong-Coupling Regime". In: *Nature* 471.7337 (Mar. 10, 2011), pp. 204–208. DOI: 10.1038/nature09898 (cit. on p. 25).

[96] G. Staupendahl and P. Gerling. "Laser Material Processing of Glasses with CO_2 Lasers". In: *Proceedings of SPIE* 3097 (Aug. 18, 1997), pp. 670–677. DOI: 10.1117/12.281133 (cit. on p. 27).

[97] C. Weingarten, E. Uluz, A. Schmickler, K. Braun, E. Willenborg, A. Temmler, and S. Heidrich. "Glass Processing with Pulsed CO_2 Laser Radiation". In: *Applied Optics* 56.4 (Feb. 1, 2017), pp. 777–783. DOI: 10.1364/AO.56.000777 (cit. on p. 27).

[98] L. Collot, V. Lefèvre-Seguin, M. Brune, J. M. Raimond, and S. Haroche. "Very High- Q Whispering-Gallery Mode Resonances Observed on Fused Silica Microspheres". In: *Europhysics Letters* 23.5 (1993), p. 327. DOI: 10.1209/0295-5075/23/5/005 (cit. on p. 27).

[99] U. C. Paek and A. L. Weaver. "Formation of a Spherical Lens at Optical Fiber Ends with a CO_2 Laser". In: *Applied Optics* 14.2 (Feb. 1, 1975), pp. 294–298. DOI: 10.1364/AO.14.000294 (cit. on p. 27).

[100] M. Wakaki, Y. Komachi, and G. Kanai. "Microlenses and Microlens Arrays Formed on a Glass Plate by Use of a CO_2 Laser". In: *Applied Optics* 37.4 (Feb. 1, 1998), pp. 627–631. DOI: 10.1364/AO.37.000627 (cit. on p. 27).

[101] D. K. Armani, T. J. Kippenberg, S. M. Spillane, and K. J. Vahala. "Ultra-High-Q Toroid Microcavity on a Chip". In: *Nature* 421.6926 (Feb. 27, 2003), pp. 925–928. DOI: 10.1038/nature01371 (cit. on p. 27).

[102] K. L. Wlodarczyk, N. J. Weston, M. Ardron, and D. P. Hand. "Direct CO_2 Laser-Based Generation of Holographic Structures on the Surface of Glass". In: *Optics Express* 24.2 (Jan. 25, 2016), p. 1447. DOI: 10.1364/OE.24.001447 (cit. on p. 27).

[103] B. Petrak, K. Konthasinghe, S. Perez, and A. Muller. "Feedback-Controlled Laser Fabrication of Micromirror Substrates". In: *Review of Scientific Instruments* 82.12 (Dec. 1, 2011), p. 123112. DOI: 10.1063/1.3671291 (cit. on p. 27).

[104] K. Ott, S. Garcia, R. Kohlhaas, K. Schüppert, P. Rosenbusch, R. Long, and J. Reichel. "Millimeter-Long Fiber Fabry-Perot Cavities". In: *Optics Express* 24.9 (May 2, 2016), p. 9839. DOI: 10.1364/OE.24.009839 (cit. on pp. 27, 39, 67).

[105] M. Uphoff, M. Brekenfeld, G. Rempe, and S. Ritter. "Frequency Splitting of Polarization Eigenmodes in Microscopic Fabry–Perot Cavities". In: *New Journal of Physics* 17.1 (2015), p. 013053. DOI: 10.1088/1367-2630/17/1/013053 (cit. on p. 28).

[106] J. H. Nielsen et al. *QCoDeS/Qcodes: QCoDeS 0.29.1*. Zenodo, Oct. 7, 2021. DOI: 10.5281/zenodo.5554601 (cit. on p. 30).

[107] A. V. Kuhlmann, J. Houel, D. Brunner, A. Ludwig, D. Reuter, A. D. Wieck, and R. J. Warburton. "A Dark-Field Microscope for Background-Free Detection of Resonance Fluorescence from Single Semiconductor Quantum Dots Operating in a Set-and-Forget Mode". In: *Review of Scientific Instruments* 84.7 (July 1, 2013), p. 073905. DOI: 10.1063/1.4813879 (cit. on p. 31).

[108] A. Kashkanova. "Optomechanics with Superfluid Helium". PhD thesis. Yale University, Dec. 2017 (cit. on pp. 34, 61, 71).

[109] A. B. Shkarin. "Quantum Optomechanics with Superfluid Helium". PhD thesis. Yale University, May 2018 (cit. on p. 34).

[110] L. Neuhaus, R. Metzdorff, S. Chua, T. Jacqmin, T. Briant, A. Heidmann, P.-F. Cohadon, and S. Deléglise. "PyRPL (Python Red Pitaya Lockbox) — An Open-Source Software Package for FPGA-Controlled Quantum Optics Experiments". In: *2017 Conference on Lasers and Electro-Optics Europe European Quantum Electronics Conference (CLEO/Europe-EQEC)*. 2017 Conference on Lasers and Electro-Optics Europe European Quantum Electronics Conference (CLEO/Europe-EQEC). June 2017, pp. 1–1. DOI: 10.1109/CLEOE-EQEC.2017.8087380 (cit. on p. 34).

[111] C. Koks and M. P. van Exter. "Microcavity Resonance Condition, Quality Factor, and Mode Volume Are Determined by Different Penetration Depths". In: *Optics Express* 29.5 (Mar. 1, 2021), pp. 6879–6889. DOI: 10.1364/OE.412346 (cit. on pp. 36, 67).

[112] T. Doualle, L. Gallais, P. Cormont, D. Hébert, P. Combis, and J.-L. Rullier. "Thermo-Mechanical Simulations of CO_2 Laser–Fused Silica Interactions". In: *Journal of Applied Physics* 119.11 (Mar. 21, 2016), p. 113106. DOI: 10.1063/1.4944435 (cit. on p. 39).

[113] E. Mendez, K. M. Nowak, H. J. Baker, F. J. Villarreal, and D. R. Hall. "Localized CO_2 Laser Damage Repair of Fused Silica Optics". In: *Applied Optics* 45.21 (July 20, 2006), pp. 5358–5367. DOI: 10.1364/AO.45.005358 (cit. on p. 39).

[114] G. A. J. Markillie, H. J. Baker, F. J. Villarreal, and D. R. Hall. "Effect of Vaporization and Melt Ejection on Laser Machining of Silica Glass Micro-Optical Components". In: *Applied Optics* 41.27 (Sept. 20, 2002), pp. 5660–5667. DOI: 10.1364/AO.41.005660 (cit. on p. 39).

[115] T. He, C. Wei, Z. Jiang, Z. Yu, Z. Cao, and J. Shao. "Numerical Model and Experimental Demonstration of High Precision Ablation of Pulse CO_2 Laser". In: *Chinese Optics Letters* 16.04 (Mar. 30, 2018), p. 41401 (cit. on p. 39).

[116] M. D. Feit and A. M. Rubenchik. "Mechanisms of CO_2 Laser Mitigation of Laser Damage Growth in Fused Silica". In: *Proceedings of SPIE* 4932 (May 30, 2003), pp. 91–103. DOI: 10.1117/12.472049 (cit. on p. 39).

[117] K. M. Nowak, H. J. Baker, and D. R. Hall. "Analytical Model for CO_2 Laser Ablation of Fused Quartz". In: *Applied Optics* 54.29 (Oct. 10, 2015), p. 8653. DOI: 10.1364/AO.54.008653 (cit. on p. 39).

[118] H. Takahashi, J. Morphew, F. Oručević, A. Noguchi, E. Kassa, and M. Keller. "Novel Laser Machining of Optical Fibers for Long Cavities with Low Birefringence". In: *Optics Express* 22.25 (Dec. 15, 2014), pp. 31317–31328. DOI: 10.1364/OE.22.031317 (cit. on p. 39).

[119] S. Garcia, F. Ferri, K. Ott, J. Reichel, and R. Long. "Dual-Wavelength Fiber Fabry-Perot Cavities with Engineered Birefringence". In: *Optics Express* 26.17 (Aug. 20, 2018), pp. 22249–22263. DOI: 10.1364/OE.26.022249 (cit. on p. 39).

[120] J.-M. Cui et al. "Polarization Nondegenerate Fiber Fabry-Perot Cavities with Large Tunable Splittings". In: *Applied Physics Letters* 112.17 (Apr. 23, 2018), p. 171105. DOI: 10.1063/1.5024798 (cit. on p. 39).

[121] D. Najer, M. Renggli, D. Riedel, S. Starosielec, and R. J. Warburton. "Fabrication of Mirror Templates in Silica with Micron-Sized Radii of Curvature". In: *Applied Physics Letters* 110.1 (Jan. 2, 2017), p. 011101. DOI: 10.1063/1.4973458 (cit. on pp. 40, 42).

[122] D. Riedel, I. Söllner, B. J. Shields, S. Starosielec, P. Appel, E. Neu, P. Maletinsky, and R. J. Warburton. "Deterministic Enhancement of Coherent Photon Generation from a Nitrogen-Vacancy Center in Ultrapure Diamond". In: *Physical Review X* 7.3 (Sept. 7, 2017), p. 031040. DOI: 10.1103/PhysRevX.7.031040 (cit. on p. 40).

[123] D. Najer et al. "A Gated Quantum Dot Strongly Coupled to an Optical Microcavity". In: *Nature* 575.7784 (7784 Nov. 2019), pp. 622–627. DOI: 10.1038/s41586-019-1709-y (cit. on p. 40).

[124] H. Kaupp, T. Hümmer, M. Mader, B. Schlederer, J. Benedikter, P. Haeusser, H.-C. Chang, H. Fedder, T. W. Hänsch, and D. Hunger. "Purcell-Enhanced Single-Photon Emission from Nitrogen-Vacancy Centers Coupled to a Tunable Microcavity". In: *Physical Review Applied* 6.5 (Nov. 22, 2016), p. 054010. DOI: 10.1103/PhysRevApplied.6.054010 (cit. on p. 40).

[125] M. Mader, J. Reichel, T. W. Hänsch, and D. Hunger. "A Scanning Cavity Microscope". In: *Nature Communications* 6 (June 24, 2015), p. 7249. DOI: 10.1038/ncomms8249 (cit. on pp. 42, 67).

[126] B. Petrak, N. Djeu, and A. Muller. "Purcell-Enhanced Raman Scattering from Atmospheric Gases in a High-Finesse Microcavity". In: *Physical Review A* 89.2 (Feb. 10, 2014), p. 023811. DOI: 10.1103/PhysRevA.89.023811 (cit. on p. 42).

[127] T. Hümmer, J. Noe, M. S. Hofmann, T. W. Hänsch, A. Högele, and D. Hunger. "Cavity-Enhanced Raman Microscopy of Individual Carbon Nanotubes". In: *Nature Communications* 7 (July 12, 2016), p. 12155. DOI: 10.1038/ncomms12155 (cit. on p. 42).

[128] N. Rossi. "Force Sensing with Nanowires". Thesis. University_of_Basel, 2019. 136 Seiten. DOI: 10.5451/unibas-007178292 (cit. on pp. 51, 54).

[129] E. Janitz, M. Ruf, M. Dimock, A. Bourassa, J. Sankey, and L. Childress. "Fabry-Perot Microcavity for Diamond-Based Photonics". In: *Physical Review A* 92.4 (Oct. 30, 2015), p. 043844. DOI: 10.1103/PhysRevA.92.043844 (cit. on p. 61).

[130] N. Podoliak, H. Takahashi, M. Keller, and P. Horak. "Harnessing the Mode Mixing in Optical Fiber-Tip Cavities". In: *Journal of Physics B: Atomic, Molecular and Optical Physics* 50.8 (2017), p. 085503. DOI: 10.1088/1361-6455/aa640a (cit. on p. 67).

[131] C. Bond, P. Fulda, L. Carbone, K. Kokeyama, and A. Freise. "Higher Order Laguerre-Gauss Mode Degeneracy in Realistic, High Finesse Cavities". In: *Physical Review D* 84.10 (Nov. 4, 2011), p. 102002. DOI: 10.1103/PhysRevD.84.102002 (cit. on p. 67).

[132] S. J. Cartamil-Bueno, M. Cavalieri, R. Wang, S. Houri, S. Hofmann, and H. S. J. van der Zant. "Mechanical Characterization and Cleaning of CVD Single-Layer h-BN Resonators". In: *npj 2D Materials and Applications* 1.1 (1 June 22, 2017), p. 16. DOI: 10.1038/s41699-017-0020-8 (cit. on p. 77).

[133] Y. Anzai, M. Yamamoto, S. Genchi, K. Watanabe, T. Taniguchi, S. Ichikawa, Y. Fujiwara, and H. Tanaka. "Broad Range Thickness Identification of Hexagonal Boron Nitride by Colors". In: *Applied Physics Express* 12.5 (Apr. 2019), p. 055007. DOI: 10.7567/1882-0786/ab0e45 (cit. on p. 79).

[134] D. J. Wilson. "Cavity Optomechanics with High-Stress Silicon Nitride Films". PhD thesis. California Institute of Technology, June 15, 2012 (cit. on p. 79).

[135] M. Korppi. "Optomechanical Coupling between Ultracold Atoms and a Membrane Oscillator". Thesis. University_of_Basel, 2014. 194 S. DOI: info:doi/10.5451/unibas-006244041 (cit. on p. 79).

[136] C. Meyer, O. Sqalli, H. Lorenz, and K. Karrai. "Slip-Stick Step-Scanner for Scanning Probe Microscopy". In: *Review of Scientific Instruments* 76.6 (May 23, 2005), p. 063706. DOI: 10.1063/1.1927105 (cit. on p. 81).

[137] C. Saavedra, D. Pandey, W. Alt, H. Pfeifer, and D. Meschede. "Tunable Fiber Fabry-Perot Cavities with High Passive Stability". In: *Optics Express* 29.2 (Jan. 18, 2021), p. 974. DOI: 10.1364/OE.412273 (cit. on p. 87).

[138] E. Janitz, M. Ruf, Y. Fontana, J. Sankey, and L. Childress. "High Mechanical Bandwidth Fiber-Coupled Fabry-Perot Cavity". In: *Optics Express* 25.17 (Aug. 21, 2017), pp. 20932–20943. DOI: 10.1364/OE.25.020932 (cit. on p. 87).

[139] Y. Fontana, R. Zifkin, E. Janitz, C. D. R. Rosenblueth, and L. Childress. *A Mechanically Stable and Tunable Cryogenic Fabry-Perot Microcavity*. Mar. 5, 2021. URL: http://arxiv.org/abs/2103.04823 (cit. on p. 87).

[140] L. Neumeier, T. E. Northup, and D. E. Chang. "Reaching the Optomechanical Strong-Coupling Regime with a Single Atom in a Cavity". In: *Physical Review A* 97.6 (June 29, 2018), p. 063857. DOI: 10.1103/PhysRevA.97.063857 (cit. on p. 88).

[141] A. S. Aporvari and D. Vitali. "Strong Coupling Optomechanics Mediated by a Qubit in the Dispersive Regime". In: *Entropy* 23.8 (8 Aug. 2021), p. 966. DOI: 10.3390/e23080966 (cit. on p. 88).

[142] M. Šiškins, M. Lee, S. Mañas-Valero, E. Coronado, Y. M. Blanter, H. S. J. van der Zant, and P. G. Steeneken. "Magnetic and Electronic Phase Transitions Probed by Nanomechanical Resonators". In: *Nature Communications* 11.1 (1 June 1, 2020), p. 2698. DOI: 10.1038/s41467-020-16430-2 (cit. on p. 88).

[143] D. Hälg et al. "Membrane-Based Scanning Force Microscopy". In: *Physical Review Applied* 15.2 (Feb. 5, 2021), p. L021001. DOI: 10.1103/PhysRevApplied.15.L021001 (cit. on p. 88).

Thibaud Ruelle

1425 Onnens VD
Switzerland
thibaud.ruelle@csem.ch
thibaudruelle/en

Education

2016–2021 **University of Basel**, Ph.D. in Experimental Physics, *summa cum laude*
"Towards Hybrid Optomechanics in a Fiber-Based Fabry-Perot Cavity"

2012–2015 **EPFL**, Master in Materials Science and Engineering, *Grade: 5.6/6*
Specialization in Materials for Microelectronics and Microtechnology, Minor in Physics
Master Thesis supported by a Scholarship from the *Fondation Zdenek et Michaela Bakala*

Current Position

2022–present **CSEM**, R&D Engineer, Quantum Tech, Systems
- participate in the development of 2-photon optical atomic clocks
- develop instruments leveraging quantum systems

Research Experience

2021–2022 **University of Basel**, *Poggio Lab & Warburton Group*, Postdoctoral Researcher
- lead a project to improve the accuracy of an existing CO_2 laser ablation setup to better than 200nm

2016–2021 **University of Basel**, *Poggio Lab*, Doctoral Researcher
- developed from scratch a fiber-based optical microcavity setup stable to within 5 picometers, for the study of functionalized mechanical nanoresonators in high-vacuum at cryogenic temperatures
- designed mechanical parts (Solidworks) complying with space and vacuum/cryo-compatibility constraints
- designed, budgeted, & assembled a laser/radiofrequency system to address the experiment
- planned & carried out measurements of the opto-mechanical properties of hBN micro-drums
- fabricated micron-sized concave mirrors at the tip of optical fibers using CO_2 laser ablation
- mentored two Master students
- co-wrote & taught the course "Measurement, Control, and Acquisition"

Winter 2015 **McGill University (Canada)**, *Quantum Defects Lab*, Research Assistant
- designed & characterized a stiff fiber-based optical cavity tuned with piezoelectric actuators

Spring 2015 **Harvard University (USA)**, *Laboratory for Nanoscale Optics (Loncar Lab)*, Master Thesis Student
- developed a fabrication process for tapered and dimpled optical fibers
- implemented a protocol to measure optomechanical coupling in patterned diamond nanobeams

2014–2015 **Excelitas Canada Inc.**, Intern - R&D and Process
- developed a microfabrication process for high aspect-ratio Through-Silicon Vias and trenches

2013–2014 **EPFL**, *Lab. of Semiconductor Materials (LMSC)*, Research Student Assistant
- helped build a confocal microscope and a Hanbury-Brown Twiss interferometer setup
- investigated the photoluminescence properties of AlGaAs nanowires
- performed *ab initio* molecular dynamics simulations of the growth of nanowires

Spring 2013 **EPFL**, *Lab. of Advanced Semiconductors for Photonics and Electronics (LASPE)*, Project Student
- performed optical spectroscopy measurements of the properties of GaN/AlGaN quantum wells

Skills and Techniques

- development of experimental platforms & measurement protocols
- characterization of microscale opto-electromechanical devices
- handling of optical fibers & fiber-optic components
- design of optical systems & mechanical parts (Solidworks, COMSOL)
- programming of control interfaces & data acquisition software (Python, Matlab, Labview)
- microscopy (confocal / scanning probe / atomic force / electron)
- data & image analysis (Python, Matlab, R)
- languages: French (native), English (fluent), German & Spanish (basic)

Soft skills

- creativity and problem-solving: designed, built, and troubleshot several experimental setups
- teamwork: research projects involved coordinating with a supervisor and co-workers
- interdisciplinary communication: designed mechanical parts with feedback from the workshop
- business communication: selected and ordered scientific tools and instruments
- scientific writing & communication: 4 peer-reviewed articles & 6 poster presentations at conferences
- leadership: mentored 2 master students, lead a student association for 2 years

Extra Activities

- treasurer of the Ilotmots association (Neuchâtel, 2018–present)
- organized technology and career events (Chairman of the IEEE Student Branch at EPFL, 2013–2014)
- taught C/C++ evening classes (Ecole d'Ingénierie Appliquée, Lausanne, 2010–2011)

Hobbies

- cycling & trail running: cycled through Jura (400km, 2 days), ran GR20 in Corsica (180km, 7 days)
- climbing: regular indoor block and lead climber
- sewing: repaired mechanical sewing machines and used them to make custom clothes and bags

Peer-Reviewed Publications

- D. Jaeger, F. Fogliano, T. Ruelle, A. Lafranca, F. Braakman, and M. Poggio, "Mechanical mode imaging of a hybrid hBN/Si_3N_4 membrane resonator," in preparation, 2023.
- T. Ruelle, D. Jaeger, F. Fogliano, F. Braakman, and M. Poggio, "A tunable fiber Fabry–Perot cavity for hybrid optomechanics stabilized at 4K," *Review of Scientific Instruments*, vol. 93, no. 9, 2022.
- T. Ruelle, M. Poggio, and F. Braakman, "Optimized single-shot laser ablation of concave mirror templates on optical fibers," *Applied Optics*, vol. 58, no. 14, 2019.
- M. J. Burek, J. D. Cohen, S. M. Meenehan, N. El-Sawah, C. Chia, T. Ruelle, S. Meesala, J. Rochman, H. A. Atikian, M. Markham, D. J. Twitchen, M. D. Lukin, O. Painter, and M. Lončar, "Diamond optomechanical crystals," *Optica*, vol. 3, no. 12, 2016.
- A. Casadei, P. Krogstrup, M. Heiss, J. A. Röhr, C. Colombo, T. Ruelle, S. Upadhyay, C. B. Sørensen, J. Nygård, and A. Fontcuberta i Morral, "Doping incorporation paths in catalyst-free Be-doped GaAs nanowires," *Applied Physics Letters*, vol. 102, no. 1, 2013.

Conference Presentations

- **T. Ruelle**, D. Jaeger, F. Fogliano, F. Braakman, and M. Poggio, "Towards hybrid optomechanics with hBN in a fiber-based Fabry-Perot cavity," oral presentation delivered at the Optomechanics Workshop in Basel, 2021.
- **T. Ruelle**, D. Jaeger, F. Fogliano, F. Braakman, and M. Poggio, "Towards hybrid optomechanics with hBN in a fiber-based Fabry-Perot cavity," poster presentation delivered at the GDR MecaQ Colloquium in Paris, *Laureate of a Best Poster Award*, 2021.

- **T. Ruelle**, D. Jaeger, A. Saeedi, F. Braakman, and M. Poggio, "An experimental platform for qubit optomechanics," poster presentation delivered at the Nanophotonics: Foundations & Applications CSF conference in Monte Verità, 2019.
- **T. Ruelle**, D. Jaeger, F. Braakman, and M. Poggio, "Fiber Fabry-Perot cavities for qubit optomechanics: Design and fabrication," poster presentation delivered at the Mechanical Systems in the Quantum Regime Gordon Research Conference and Seminar in Ventura, 2018.
- **T. Ruelle**, F. Braakman, and M. Poggio, "Experimental setup for combined cavity optomechanics and QED," poster presentation delivered at the Quantum Nanophotonics CSF conference in Monte Verità and at the Frontiers of Nanomechanical Systems conference in La Thuile, 2017.
- **T. Ruelle**, F. Braakman, and M. Poggio, "Experimental setup for combined cavity optomechanics and QED," oral presentation delivered at the QSIT Junior Meeting in Passug, 2016.